

Hadronic multiparticle production with Sibyll

Zur Erlangung des akademischen Grades eines

Doktors der Naturwissenschaften

an der Fakultät für Physik des
Karlsruher Instituts für Technologie (KIT)

genehmigte

Dissertation

von

Dipl. Phys. Felix Riehn

aus Landstuhl

Tag der mündlichen Prüfung: 11.12.2015

Referent: Prof. Dr. Dr. h. c. J. Blümer

Korreferent: Priv. Doz. Dr. S. Gieseke

Betreuer: Dr. R. Engel

Hiermit versichere ich, die vorliegende Arbeit selbständig verfasst und nur die angegebenen Hilfsmittel verwendet zu haben.

Felix Riehn

Karlsruhe, den 15. November 2015

There is no fun, fun, fun.

There is no fun, fun, fun.

There is no fun, fun, fun.

...

There is no fun in fundamentalism.

(M. Burkett)

Contents

1	Introduction	1
2	Cosmic rays, air showers and hadronic interactions	3
2.1	Cosmic rays	3
2.2	Hadronic interactions	4
2.3	Extensive air showers	10
2.4	Inclusive atmospheric fluxes	18
3	The hadronic interaction model Sibyll 2.1	21
3.1	Cross section and scattering amplitude	22
3.2	Event generation	27
3.3	Hadronization	29
3.4	Performance & shortcomings of SIBYLL 2.1	31
3.5	Nucleus-nucleus interactions	33
4	Cross section and parton density update	35
4.1	Cross section update	35
4.2	New parameterizations of the parton distribution functions	38
5	New remnant treatment	39
5.1	Leading particle effect in SIBYLL 2.1	39
5.2	Remnant model	41
6	Extension to charm production	47
6.1	Charm model	47
6.2	Tuning of the parameters	48
7	Tuning of fragmentation parameters	53
7.1	Baryon production	53
7.2	Leading ρ^0 production	55
7.3	Transverse momentum	57
8	Intermediate states in the Glauber model	61
8.1	The Glauber model and inelastic screening	61
8.2	Diffraction dissociation in nuclear collisions	63
9	Comparison with accelerator data	71
9.1	Fixed target experiments	71
9.2	Large Hadron Collider	74
9.3	Extrapolation	79
10	Predictions for cosmic ray interactions	83
10.1	Extensive air showers	83
10.2	Inclusive atmospheric fluxes	93

11 Conclusion	97
A Appendix	103
A.1 Model parameters	103
A.2 Particle listings	103

Chapter 1

Introduction

Particle astrophysics is the application of particle physics to the study of the high energy universe. Through the detection of messenger particles, like photons (γ -rays), neutrinos and protons or nuclei, the most extreme environments and events, for example, active galactic nuclei or supernovae, can be studied.

While the observation of these messengers gives information from distant and violent places, they also constitute a test of our understanding of particle physics. Every step along the way, from the production at the source, the propagation through space, to the arrival at Earth, is determined by the laws of particle physics.

For protons and nuclei the interactions with matter are called hadronic interactions. While these interactions are in principle described by the quantum field theory of color charged quarks and gluons, Quantumchromodynamics, in the Standard Model of particle physics, the outcome of an interaction currently can only be calculated for collisions at small distances.

In order to make predictions for the flux of hadrons produced by an astrophysical source, to calculate the attenuation of the flux due to interactions with the interstellar medium or to interpret the measurement of the particle shower that is produced when the hadron enters the atmosphere, hadronic interactions have to be accounted for at every step along the way.

Predictions are typically calculated with the help of Monte Carlo event generators, also called interaction models. These models represent the current understanding of hadronic interactions and form a link between particle physics and astrophysics. Laboratory experiments on Earth are limited in energy and typically are conducted using protons. The application in astrophysical scenarios, on the other hand, requires the models to make predictions for higher energies than could ever be reached by man-made accelerators, while also using particle configurations that are rarely probed in experiment. The knowledge gained in accelerator experiments has to be transferred to collisions between different particles and extrapolated to high energies and different regions of phase space. The hadronic interaction models therefore also introduce a large uncertainty.

Two concrete problems that concern two of the astrophysical messengers, cosmic rays and neutrinos, and that are related to hadronic interactions, are the prediction of the number of muons in extensive air showers and the prediction of the flux of high energy neutrinos in the atmosphere.

In the case of air showers, the problem appears in the interpretation of the shower measurements in terms of the energy and mass of the primary cosmic ray particles. Based on the predictions from current interaction models, different observables do not give a consistent interpretation in terms of mass composition. The discrepancies can be explained by assuming that the number of muons in simulated air showers is too low, which means some aspect of the hadronic interaction is misrepresented in the models. Alternatively, new processes at high energy that are not included in the standard model could lead to these discrepancies. Also without the information whether the particles with the highest energies in the universe are protons or nuclei, their origin cannot be explained.

For the measurement of neutrinos, the problem is that decays of short-lived particles in the atmosphere produce a background of high energy neutrinos that can not always be separated

from the astrophysical flux. In order to subtract this background, it has to be known as accurately as possible. One type of short-lived hadrons that decay into neutrinos are charmed hadrons, which are not yet included in current hadronic interaction models.

One of the hadronic interaction models used in particle astrophysics is SIBYLL. It was one of the first models based on a microscopic picture of hadron interactions. The essential features in the early versions were multi-parton interaction in the form of minijets and string fragmentation. In the extension to the current version, SIBYLL 2.1, soft interactions, diffraction dissociation and an effective saturation model were added. It was tuned to low energy fixed-target and TeVatron data.

In this work, extensions to the model, that were motivated by the problems with the measurements of high energy cosmic rays and neutrinos, are developed and discussed. The aim is to produce a model that reproduces the essential features of hadronic multiparticle production and makes consistent predictions for extensive air showers and atmospheric fluxes.

First (Sect. 2) the mechanisms of particle production in the atmosphere and hadronic interactions, in general, are discussed. Then the microscopic model of hadronic particle production that is used in SIBYLL is introduced in Sect. 3.

In the main part, the model extensions are presented. Since each new accelerator measurement at high energy, tests and improves the extrapolation, the update of the cross section including the LHC measurements is discussed first (Sect. 4.1). A new model for the treatment of leading particles in SIBYLL, so-called beam remnant formation, is introduced next (Sect. 5). Both the remnant model and the charm model, that is presented in Sect. 6, have a large influence on the flux of atmospheric muons and neutrinos.

With regard to the discrepancy in the number of muons in air showers, the retuning of certain processes that were deemed important for the production of muons in air showers is discussed in Sect. 7. Since the interactions in the atmosphere occur between hadrons and nuclei, the basic hadron-proton model is translated in SIBYLL to nuclei by considering the effects of multiple target nucleons in one interaction. In this thesis this approach is extended to include intermediate states of the hadrons as described in Sect. 8. Comparisons of the predictions of the resulting new model with laboratory measurements are presented in Sect. 9. An update of the predictions for air shower observables and their uncertainty are discussed in Sect. 10. Finally, the main results of this thesis are summarized in Sect. 11.

Chapter 2

Cosmic rays, extensive air showers and hadronic interactions

2.1 Cosmic rays

Cosmic rays (CR) are relativistic particles that reach the Earth from outside the solar system. Their masses, in principle, range from single nucleons ($A = 1$) to the heaviest long-lived nuclei ($A \sim \mathcal{O}(200)$). Since the abundance is much lower for any nucleus beyond iron, usually only nuclei up to iron ($A = 56$) are considered. The energy spectrum of the total flux of these particles is shown in Fig. 2.1. The spectrum has the general shape of a power law, it is steeply falling and extends over many orders of magnitude in flux and energy. To improve readability the flux is scaled by a factor $E^{2.5}$ in Fig. 2.1.

The spectrum contains several features. There are two evident breaks in the slope of the spectrum (power-law: $\Phi \sim E^\gamma$, slope: γ) and there seems to be a strong suppression at the highest energies. These features probably can be explained in terms of effects in propagation, the acceleration mechanisms at the sources and transitions between different source populations. Typically there are multiple explanations and models for each feature [2].

In order to discriminate the models, more information is needed. An observable that could help distinguish models, would be the individual fluxes Φ_i of each particle species (mass), the so-called *mass composition*. The problem is that, at high energies, cosmic rays can only be measured indirectly through the detection of *extensive air showers* (EAS). The mass composition then has to be inferred from the measured properties of the air showers.

At this point hadronic interactions come into play. Since the energies reached by cosmic rays by far exceed the energies obtainable with accelerators on Earth (see upper axis in Fig. 2.1), hadronic interactions introduce some additional uncertainty in the interpretation of air shower observables. The connection between properties of hadronic interactions and air shower observables will be discussed further in Sect. 2.3. The current uncertainty of hadronic interactions and the effect on EAS observables, one of the conclusions of this work, are presented in Sect. 10.

Depending on the different explanations for the features in the spectrum and the accompanying mass composition, different fluxes for neutrinos and photons (γ -rays) are expected. In particular high energy neutrinos (IceCube) can be expected to be strongly correlated with cosmic ray protons through hadronic interactions (pion production and decay). Leptonic production of neutrinos is suppressed compared to hadronic production by a factor $g_w/g_s = \mathcal{O}(10^{-5})$ from the interactions alone. Only in some particular environments with high (energy) density, like supernova explosions, electroweak production of neutrinos does play an important role.

For example, one scenario for the suppression of the flux of cosmic rays observed at high energy is that due to the *Greisen-Zatsepin-Kuzmin* (GZK) [3, 4] effect. It states that protons with very large energy are subject to an additional process of energy loss, namely inelastic scattering with photons of the cosmic microwave background. The threshold (also the peak) of the reaction is determined by the Δ -resonance with a mass of $1.232 \text{ GeV}/c^2$. Due to the low energy of the CMB photons, the threshold energy for the protons is pushed to 60 EeV. Incidentally this is the

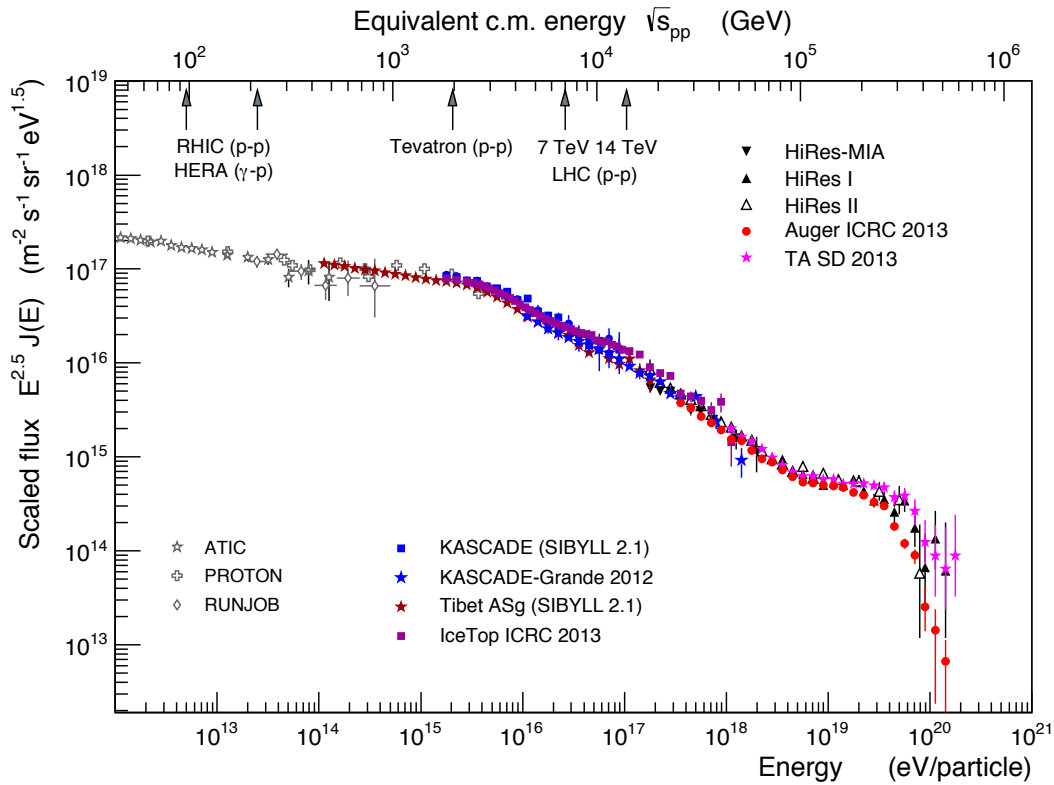


Figure 2.1: The all particle cosmic ray flux as a function of energy [1]. Data points in color represent indirect measurements, in gray are direct balloon or satellite measurements. On the upper axis the equivalent cm. energy of a proton is shown. The highest energetic particles correspond to $\sqrt{s} \simeq 500$ TeV protons.

energy range where a strong suppression of the flux is observed in the CR spectrum. In the decay of the Δ resonance pions are produced ($\pi^0 : \pi^+ = 2 : 1$, see Tab. 5.1) that then decay into photons and neutrinos, respectively. If the composition in the suppression region is dominated by protons, one would therefore expect a certain flux of secondary neutrinos and photons at high energy. High energy photons are also susceptible to interactions with background photon fields (e^+e^- pair threshold is even lower), so they might not propagate very far. The high energy GZK neutrinos, on the other hand might well reach Earth. After the discovery of astrophysical neutrinos of high energy by IceCube [5], this kind of *multi messenger* analysis has all the markings of a good tool to study the features of the cosmic ray sources and the high energy universe.

2.2 Hadronic interactions

2.2.1 Parton model

The question of the structure of the proton (hadrons) has determined the field of high energy physics during the last century. The contemporary answer is: "At what scale?" meaning it depends on the scale at which one is looking.

On small scales hadrons were shown to be composite objects made up of quarks and gluons. The interaction of these can be described by a quantum field theory, *Quantumchromodynamics* (QCD). On larger scales, the description of the hadron through a collection of point-like *partons* (quarks and gluons) seems to become inadequate. At least the interactions can not be described mathematically in a sensible way in terms of partons. The picture is that, at large scales, groups of partons interact collectively.

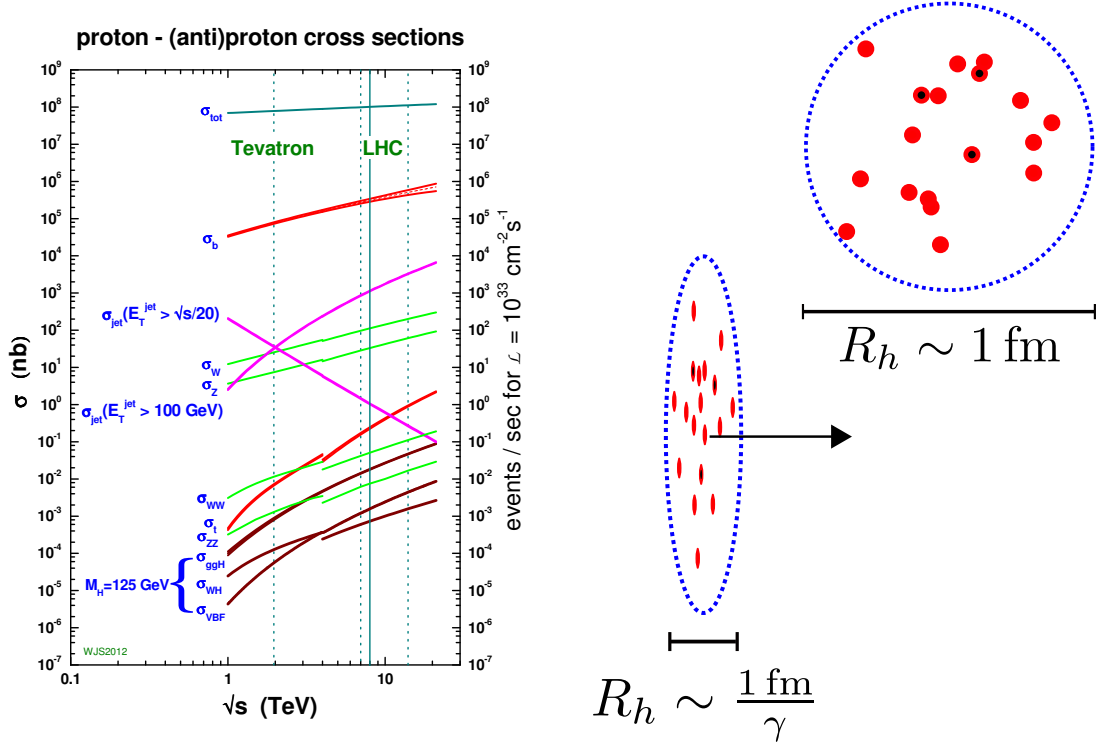


Figure 2.2: Left: Standard model cross sections at the LHC [6]. Hadronic interaction, in this context roughly speaking, refers to all the processes that make up the difference between the total cross section and bottom production in the plot. Right: Schematic picture of hadrons at high energy. The number of partons drawn resembles the number of binary parton scatterings that can occur.

While colliding hadrons, in principle, can interact via any of the interactions in the Standard Model, the term hadron interaction typically only refers to the subset of strong interactions. In Fig. 2.2 various cross sections for processes in pp collisions are shown as a function of center-of-mass energy. Hadron interactions in the narrow sense, are the interactions that make up the bulk of the total cross section. Bottom production (second line from the top) is already quite rare.

From the geometry of the situation, some general features of hadron collisions can already be derived. In the center-of-mass frame of reference (cm. frame), by definition, the colliding hadrons have the same but opposite momenta. It is customary in high energy physics to choose the z-axis along the direction of the momentum of the colliding particles, so that the 4-momentum in the cm. frame is $p_i = (E_i, 0, 0, \pm p_z)$. The hadron with momentum $+p_z$ will be called the beam, the one with $-p_z$ target. The total energy in the center-of-mass frame (cm. energy, E_{cm}) is usually expressed in terms of the Lorentz-invariant variable \sqrt{s} , with

$$\begin{aligned}
 s &= (p_{\text{beam}} + p_{\text{target}})^2 \\
 &= (E_{\text{beam}} + E_{\text{target}})^2 \\
 &= E_{\text{cm}}^2.
 \end{aligned} \tag{2.1}$$

In this frame, the x and y components of the momenta on parton level have to add up to zero but individually they can still be non-vanishing. In fact the limited size of the hadron of ~ 1 fm in combination with the uncertainty relation ($\Delta(x, y)\Delta(p_x, p_y) \sim 1$) means the partons on average should have a transverse momentum $p_{\perp} = \sqrt{p_x^2 + p_y^2}$ of the order of 0.4 GeV. The collisions of interest here, have energies well within the relativistic regime ($E_{\text{cm}} \gg m_{\text{beam}}$). The lowest energies of interest here are encountered in fixed target experiments where typical cm. energies are in the order of 20 GeV. The highest energies that can be studied in the laboratory

are currently reached at the LHC with 13 TeV. Ultra-high energy cosmic rays have been observed up to cm. energies of 500 TeV (see upper axis in Fig. 2.1). The Lorentz factors $\gamma = E_i/m_i$ for protons ($m_p \sim 1$ GeV) in these cases are: 20, 13000 and $5 \cdot 10^5$. The Lorentz contraction along the direction of motion is correspondingly large, so that the hadron at high energy has to be pictured as a narrow disk of partons (see Fig. 2.2-right).

Along z , the *longitudinal* direction, parton momenta can range from around zero to the order of the hadron momentum. This difference in scale between the initial conditions in the transverse and longitudinal direction is also present in the final state. There are typically a few particles produced with very large momentum along the beam direction and many particles with low momentum (relative to p_z) transverse to the beam. The distributions in different phase space variables are discussed in more detail in Sect. 2.2.3.

2.2.2 Event types

Interactions of hadrons can be separated into two different categories (see Fig. 2.3). Interactions where the final state particles are the same as the initial state particles are called *elastic* interactions.

$$A + B \rightarrow A + B \quad (2.2)$$

In combination with momentum and energy conservation only the direction of the momentum vector can be changed in these interactions. In the parton picture, elastic interaction requires the coherent interaction of all partons of one hadron with the partons in the other hadron. This becomes more unlikely with increasing energy where there is enough phase space available for hard interactions to occur so one expects the fraction of interactions that are elastic to decrease with energy. The probability of interaction is usually expressed in cross sections, so the separation of interactions is written as

$$\sigma_{\text{tot}} = \sigma_{\text{ela}} + \sigma_{\text{inel}} \quad (2.3)$$

and the requirement for coherent interaction in elastic scattering means $\sigma_{\text{ela}}/\sigma_{\text{tot}}$ decreases.

Interactions where there are additional or different particles produced in the final state are called *inelastic* interactions.

$$A + B \rightarrow A' + B + C + \dots$$

In general these can be seen as the exchange of energy, momentum and any quantum number between the colliding hadrons. Along these exchanges inelastic interactions can be further separated into two categories: *diffractive* and *non-diffractive* interactions.

In diffractive interactions (more completely: interactions in which diffractive dissociation occurs) only energy and momentum are exchanged between the hadrons and one (single diff.) or both (double diff.) transition into an excited state. The subsequent decay of the excited state, yields new particles (typically pions) and therefore the interaction is counted as an inelastic process.

$$A + B \rightarrow A^* + B \rightarrow A' + A'' + \dots + B$$

The similarities to the elastic process are nevertheless clear. Since the individual partons carry various quantum numbers, in particular since gluons carry color, the interaction can not involve the exchange of a single gluon or the scattering of a few quarks. Like elastic scattering diffractive interactions require the coherent interaction of the hadrons. For the same reason as before the fraction of diffractive events in inelastic scattering is therefore bound to decrease with energy. The interference effects that can be seen due to the coherent nature of the interaction are of course the reason it is called *diffractive* dissociation.

The rest of the interactions are *non-diffractive*. Here finally any number of independent gluons or quarks can be exchanged, so that the hadrons are connected by multiple color fields that fragment into new hadrons.

$$A + B \rightarrow C + D + \dots$$

Experimentally non-diffractive and diffractive interactions can only be distinguished to a certain degree. Especially if the acceptance of the detectors does not cover the entire phase space. For single diffractive events one typically looks for particle production on one side of phase

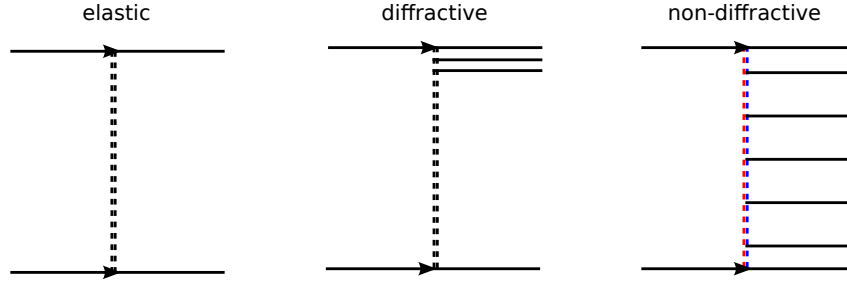


Figure 2.3: Different event types in hadron interactions. Elastic, diff, and non-diff.

space. To distinguish non-diffractive and double diffractive events one can look for regions in longitudinal phase space without particle production. Large gaps are more likely to come from diffractive events.

2.2.3 Kinematic variables and phase space

To describe the final state of hadronic interactions different variables are used depending on the process or phase space of interest. If one wants to study the structure of hadrons, the fundamental interactions or wants to find new particles and interactions (Higgs, SuSy), the transverse phase space is where to look.

For the study of air showers and hadronic interactions in astrophysical scenarios longitudinal phase space is much more important, since this is where particles carry most of the energy. Also one is interested in the typical interaction not the rare exception.

Feynman- x

The fraction of the maximal longitudinal momentum carried by a final state hadron in the center of mass frame (c.m. frame) is the typical variable to describe longitudinal phase space. It is also called Feynman- x , after the scaling law proposed by Feynman [7].

$$x_F = \frac{p_{\parallel}}{p_{\text{c.m. max}}} \quad (2.4)$$

The law states that differential cross sections in hadron collisions at high energy are universal functions of x_F and the transverse momentum p_{\perp}

$$E \frac{d^3\sigma}{d^3\vec{p}} = f(x_F, p_{\perp}) . \quad (2.5)$$

Although it was shown in many experiments since then that Feynman scaling is violated in the central region ($x_F \approx 0$), it probably still holds for large x_F , the so-called *fragmentation region*.

The reference frame in air showers is the laboratory, or fixed-target frame of reference (lab. frame), where one of the collision partners, the target, is at rest. In that case the longitudinal momentum fraction is formed relative to the beam particle, i.e. the total momentum.

$$x_L = \frac{p_{\parallel, \text{Lab}}}{p_{\text{beam, Lab}}} \quad (2.6)$$

Lab. frame and c.m. frame are transformed into one another with a Lorentz boost. Applying this boost to x_F and expanding in the ratio of the transverse mass $m_T = \sqrt{p_{\perp}^2 + m^2}$ to particle energy E , the relation of x_F to x_L is found to be

$$x_F = x_L - \frac{m_T^2}{2mE} + \mathcal{O} \left[\left(\frac{m_T}{E} \right)^2 \right] . \quad (2.7)$$

For small p_{\perp} and large x_F , $m_T/E \rightarrow 0$ and x_F can be replaced by x_L , since the two are equal.

Transverse Momentum p_{\perp}

The transverse phase space is usually described directly with transverse momentum

$$p_{\perp} = \sqrt{p_x^2 + p_y^2}. \quad (2.8)$$

Since transverse momentum in the hadron initial state is zero, the distribution of final particles in p_{\perp} is very steeply falling. Apart from the intrinsic p_{\perp} due to the localization of the wave function to the hadron ($\mathcal{O}(0.5 \text{ GeV})$), the partons can only acquire transverse momentum in the scattering process. Turning the argument with the uncertainty relation in transverse space from before around ($\Delta b \Delta p_{\perp} \sim 1$), it is evident that large p_{\perp} means small length scales. The study of parton interactions, searches for new partons or parton substructure, for these reasons, are all carried out by looking at collisions with high p_{\perp} particles ($p_{\perp} > 10 \text{ GeV}$).

The large scale structure of hadrons on the other hand determines the low p_{\perp} region.

Rapidity y

A variable that mixes transverse and longitudinal phase space is the *rapidity*

$$\begin{aligned} y &= \frac{1}{2} \ln \left(\frac{E + p_z}{E - p_z} \right) \\ &= \ln \left(\frac{E + p_z}{m_T} \right). \end{aligned} \quad (2.9)$$

Under a boost along the axis it is defined with (here z), it changes simply by an additive term

$$y' \rightarrow y + \ln \sqrt{\frac{1 - \beta}{1 + \beta}}. \quad (2.10)$$

Since this is similar to the behavior of angles in ordinary 3-space under rotation it can be seen as a relativistic (4dim, Minkowski-space) angle. This simple transformation law is particularly helpful when modeling hadron collisions with multiple parton interactions (MPI), since each individual interaction is best described in the respective parton c.m. system, which can be transformed to the hadron c.m. system by a boost along z .

The rapidity has a maximal value when $p_{\perp} \rightarrow 0$, which is exactly fulfilled for the initial state particles, and it is given by

$$y_{\max} = \ln \left(\frac{E + p_z}{m_{\text{beam}}} \right) \quad (2.11)$$

$$\approx \ln \left(\frac{\sqrt{s}}{m_{\text{beam}}} \right). \quad (2.12)$$

The final state particles therefore roughly range from $-y_{\max}$ to y_{\max} . The exception are particles lighter than the beam particles, e.g pions in the case of beam protons, which can range a little further

$$y_{\max}^{\text{pion}} = y_{\max}^{\text{beam}} - \ln \left(\frac{m_{\text{pion}}}{m_{\text{beam}}} \right). \quad (2.13)$$

In experiment it is not always possible to identify the particles so the y , since it requires the mass of the particles, can not be calculated. Therefore the *pseudorapidity* η is used, which has the same definition as the rapidity only with energy replaced by momentum

$$\begin{aligned} \eta &= \frac{1}{2} \ln \left(\frac{p + p_z}{p - p_z} \right) \\ &= \ln \left(\frac{p + p_z}{p_{\perp}} \right). \end{aligned} \quad (2.14)$$

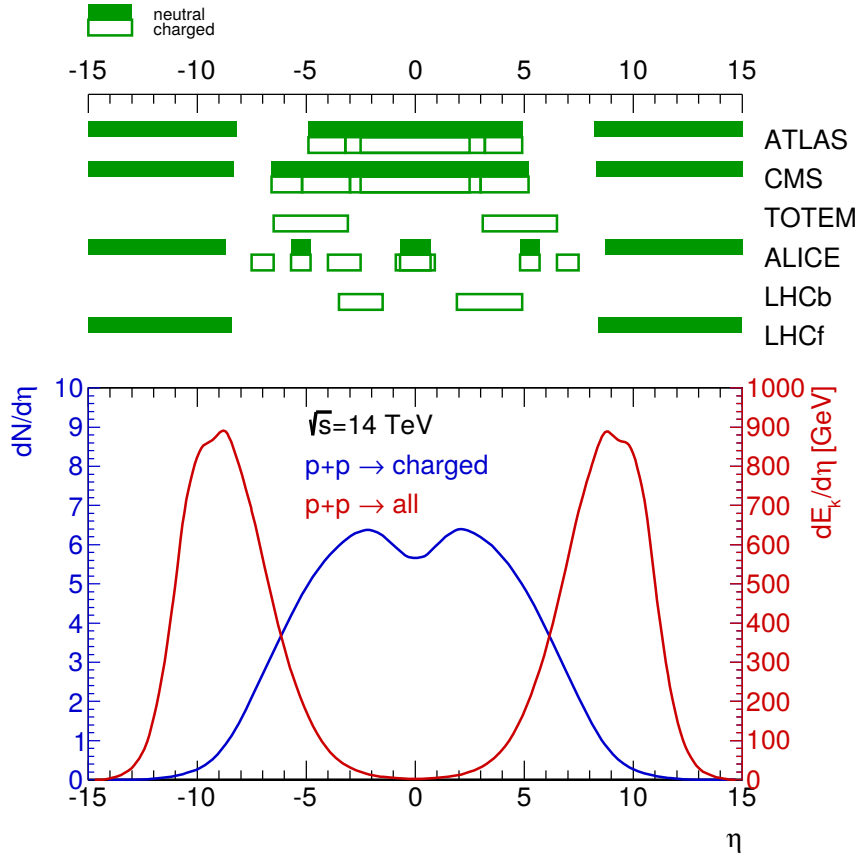


Figure 2.4: Energy and particle flow as a function of pseudorapidity at the LHC. The green bands represent the coverage of different detector components. Plot by R. Ulrich.

As only the components of the momentum vector are used it is not surprising that η can be exactly mapped to the scattering angle θ

$$\eta = -\ln\left(\tan\frac{\theta}{2}\right). \quad (2.15)$$

With this definition not even the measurement of the momentum of the particles is required. All that is needed is the track of the particle to get the scattering angle.

In contrast to the rapidity the range covered by the final state particles in pseudorapidity is not limited (no mass to regulate the denominator in Eq. 2.14), but extends from $-\infty$ to ∞ .

The typical range covered by detectors at the LHC is shown in Fig. 2.4 on the top. The maximal forward coverage can be achieved for neutral particles by placing a detector between the beam pipes, which corresponds to $\eta \rightarrow \infty$. The large multipurpose detectors, CMS and ATLAS, only cover $|\eta| \lesssim 3$. This reflects the fact that these detectors were designed to look for new physics by probing the smallest scales, which necessarily means measuring large p_{\perp} and small (pseudo)rapidities ($\Delta p_{\perp} \Delta b \sim 1$).

Air showers on the other hand are most sensitive to large rapidities. One way this can be seen is by noting that particle production appears in the cascade equations (more in next section, Sect. 2.3), with a factor of x_L , which gives large $x_L \approx x_F$ more weight. Another way of seeing this is by looking at where particles carry the most energy in an interaction.

In Fig. 2.4 on the bottom the energy flow $dE/d\eta$ and particle production $dN/d\eta$ are shown together as a function of the pseudorapidity. While most particles are produced in the central rapidity region, the bulk of the energy is carried by just a few particles in the forward region. Comparing to the acceptance of the detectors at the LHC, the bulk of the energy flow lies outside the acceptance for charged particle detection. Only neutral particles can be detected in the most

forward direction. The curves shown here are for a c.m. energy of 14 TeV calculated with a model. Measurements of the same quantities compared to SIBYLL and other models can be seen in Sect. 9.2.

Alternatively the rapidity can be defined through the differential equation (the solution to which is given by Eq. 2.9)

$$dy = \frac{dp_{\parallel}}{E}. \quad (2.16)$$

This definition shows that the invariant phase space element $E d^3/d^3\vec{p}$, introduced in Eq. 2.5, can be rewritten to

$$E \frac{d^3}{d^3\vec{p}} = \frac{d^3}{d^2\vec{p}_{\perp} dy}. \quad (2.17)$$

Considering azimuthal symmetry the transverse plane can be simplified by introducing polar coordinates. One finally arrives at

$$E \frac{d^3}{d^3\vec{p}} = \frac{1}{\pi} \frac{d^2}{dp_{\perp}^2 dy} \quad (2.18)$$

$$= \frac{1}{2\pi p_{\perp}} \frac{d^2}{dp_{\perp} dy}, \quad (2.19)$$

which is a common and convenient measure to show final state distributions in high energy physics.

Multiplicity N_{ch}

The multiplicity describes the number of charged particles per event. After the total cross section it is probably the most basic (not necessarily simplest) thing to measure. Nevertheless it contains some information about the structure of hadrons.

The emergence of jets and the associated violation of Feynman scaling at energies $\sqrt{s} \geq 50$ GeV, for example, manifests itself in the multiplicity distribution through the appearance of a large tail towards high multiplicities.

The shape of the distribution as a whole is determined by the overlap of the hadron profiles. Low multiplicity events can be seen as predominantly peripheral, high multiplicity events mostly as central collisions.

2.3 Extensive air showers

This section gives a short introduction into the physics of air showers and the link to hadronic interactions. It is based on the review by Engel et al. [1] and the textbook by Gaisser [8].

2.3.1 Development

The general features of air shower development can already be inferred from the properties of pions. As pseudo scalar particles pions do not carry any spin, which makes them Bosons. They are the lightest hadrons with masses of 139 MeV for the charged pions and 135 MeV for the neutral. Being bosons and light, pions are produced in abundance in hadronic interactions. At the ISR ($\sqrt{s} = 53$ GeV) for example, the average number of charged pions produced in a pp interaction was measured to be 9.2 while the total number of charged particles was 10.5 [11]. Air showers are formed from many subsequent interactions. Except for the first few, individual interactions do not matter much and fluctuations introduced by single interactions are averaged out quickly. Pion production, in determining the average hadronic interaction, therefore also plays a dominant role in air showers.

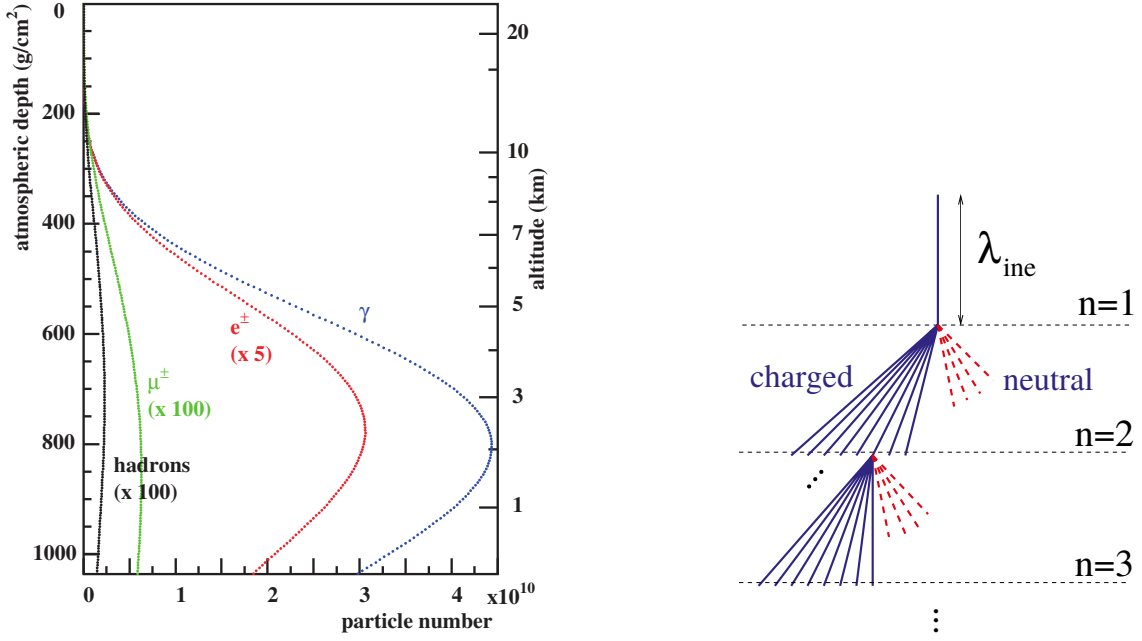


Figure 2.5: Left: Longitudinal profiles in an air shower induced by a proton with primary energy 10^{19} eV (100 TeV cm.). Em. particles are more numerous than hadrons or muons, so they determine the position of max. development. Hadronic particles and muons are more penetrating. In particular muons can still be observed when other particles have been absorbed (e.g. in very inclined showers). Right: Sketch of hadronic cascade in Heitler-Matthews model [9]. The model assumes only pions are produced. At each step in the cascade the energy is shared equally among these pions. Figures from Ref. [1]

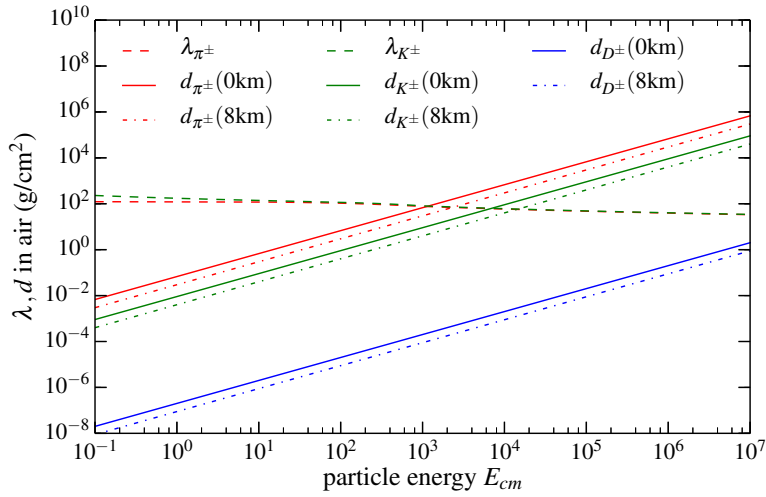


Figure 2.6: Comparison of the decay and interaction lengths of different mesons [10].

Due to the different decay channels of charged and neutral pions, air showers develop in two components: the electromagnetic and the hadronic component. Charged pions carry isospin, so the only possible decay channel is via the weak interaction

$$\begin{aligned}\pi^+ &\rightarrow \mu^+ + \nu_\mu \\ \pi^- &\rightarrow \mu^- + \bar{\nu}_\mu.\end{aligned}$$

In principle the final state containing electrons is allowed as well, but it is strongly suppressed due to parity. Since it is a weak decay the decay length in the rest frame is long, $c\tau_0 = 7.8$ m.

Neutral pions do not carry isospin ($I, I_3 = (1, 0)$) and since they are the lightest hadrons the dominant decay is via the electromagnetic interaction into two photons

$$\pi^0 \rightarrow \gamma + \gamma .$$

The decay length is accordingly short $c\tau_0 = 25$ nm.

Even though the decay length in the atmosphere is increased at high energy by the Lorentz dilation $l = c\tau_0 (E/m)$, neutral pions will almost always decay before reaching another nucleus in the air to interact. The photons produced in the decay can only interact electromagnetically, the dominant process being electron pair production. Electrons in turn are also most likely to interact electromagnetically, and thus the *electromagnetic* cascade is formed.

Interaction probability as a function of distance is expressed by the interaction length, since it depends on the surrounding matter it is usually written in units of g/cm^2 by including the local matter density $\lambda_{\text{int}} = \rho l_{\text{int}}$. Interaction probability microscopically is determined by the cross section of the particle with the target material. It can be expressed as a length by including the target number density $\rho_A = \rho/(A m_{\text{nuc}})$, so that finally

$$\lambda_{\text{int}} = \frac{A m_{\text{nuc}}}{\sigma_{\text{air}}} . \quad (2.20)$$

Note that the final result is independent of the density, the target material enters solely through the effective mass $A m_{\text{nuc}}$. To compare interaction and decay, the decay length is also expressed in units of g/cm^2

$$\lambda_{\text{dec}} = \rho c\tau_0 \cdot \left(\frac{E}{m} \right) . \quad (2.21)$$

In Fig. 2.6 the decay and interaction lengths of different particles in the atmosphere are shown. The interaction length is approximately constant with energy ($\sigma_{\text{prod}} \sim \ln s$) and for pions it is of the order of $120 \text{ g}/\text{cm}^2$. The decay length on the other hand increases linearly with energy. Because of the explicit dependence on the density in Eq. 2.21 the decay length changes slightly according to the vertical position in the atmosphere. The energy at which a particle is more likely to interact than to decay is called *critical energy*. For charged pions interaction is very likely at energies larger than $\mathcal{O}(100 \text{ GeV})$. In each interaction they will produce more particles (pions) and thus the *hadronic cascade* develops.

Neutral pions can be produced in any hadronic interaction, which means during the development of the shower, energy is constantly transferred from the hadronic to the em. component (see Fig. 2.5-right). The em. interaction in turn only rarely produces hadrons, so the energy transfer is in one direction only. This means that after $n \approx 6$ generations 90% of the energy will be in the em. component.

The interaction length of em. interactions, the *radiation length*, is only $X_0 = 37 \text{ g}/\text{cm}^2$ in air. In combination with the low mass of the electrons this means the em. cascade develops more rapidly in depth than the hadronic cascade and the total number of particles is dominated by the em. cascade. Pions are only the dominating species within the hadronic component.

Upon reaching the critical energy, charged pions will decay and produce muons and neutrinos. Within the remaining atmosphere neither muons nor neutrinos interact very often. Depending on their energy the muons will eventually be stopped somewhere underground. Neutrinos, unless at extremely high energy, will propagate through the Earth.

2.3.2 Observables

Longitudinal development

In Fig. 2.5 on the left, the number of particles in the different components of an air shower are shown as a function of the depth, the so called *longitudinal profile*. Profiles are shown for hadrons, muons, electrons and photons separately. The dominance of em. particles is quite

evident. However, as easy as em. particles are produced they are absorbed again, a fact that is reflected in the rapid decline of the particle number in the em. component after the maximum in Fig. 2.5. The depth at which the maximal number of particles is reached in an air shower is called *shower maximum*, denoted by X_{\max} .

Different primary particles produce slightly different air showers with different profiles. Since the interactions within the bulk of the air shower are the same (em. and hadronic), the difference is mostly due to the first interactions. The obvious difference between primary particles (protons and nuclei), is size. The larger the nucleus is, the larger the cross section will be and therefore the higher up in the atmosphere the first interaction will occur. This is one of the effects of the primary particle.

The second is that, since the development of the air shower ceases when the energy of the particles is below a certain threshold, that is when the energy has been dissipated, showers from large nuclei will terminate after fewer generations than proton induced showers, because the primary energy is initially distributed among several nucleons.

Air showers initiated by large nuclei therefore reach shower maximum at smaller atmospheric depths (larger heights). Because of the large number of different particles and the large fluctuations in the final state of hadronic interactions, the hadronic cascade is difficult to describe analytically. As an approximation, based on the description of em. cascades, where the situation is more simple, because only two particles are involved (electrons and photons) and the multiplicity is always two (bremsstrahlung and pair production), the hadronic cascade can be modeled by assuming that:

- only pions are produced in hadronic interactions,
- the multiplicity is fixed n_{tot} ,
- charged and neutral pions are produced in the ratio 2:1.
- the energy is shared equally.

In this approximation, called the Heitler-Matthews model [9], the energy in the em. and hadronic component is given by

$$E_{\text{had}} = \left(\frac{2}{3}\right)^n E_0 \quad E_{\text{em}} = \left[1 - \left(\frac{2}{3}\right)^n\right] E_0. \quad (2.22)$$

Assuming that the depth of shower maximum is determined by the em. component it can be written as

$$X_{\max} = \lambda_{\text{int}}(A) + X_0 \cdot \ln\left(\frac{E_0}{A \cdot 2n_{\text{tot}}E_{\text{crit}}}\right). \quad (2.23)$$

The above equation is only correct within that model, but the general shape: primary interaction length plus em. cascade proportional to $\ln(E_0/A)$ also applies to full simulations [12], so the effect of later interactions on X_{\max} is indeed small. The dependence on the primary mass number through the factor A in the denominator is introduced assuming *superposition*, i.e. a shower initiated by a nucleus A behaves like A parallel proton shower. Evidently this neglects possibility of piece wise fragmentation of the nucleus (more see Sect. 3.5 and references therein).

The average depth of maximal development of air showers at a given energy, $\langle X_{\max} \rangle$, is one of the observables used for the determination of the mass composition. The larger $\langle X_{\max} \rangle$ the larger is the fraction of light nuclei in cosmic rays.

The change of $\langle X_{\max} \rangle$ with regard to the logarithm of the primary energy, is called the *elongation rate*

$$\begin{aligned} D_e &= \frac{d\langle X_{\max} \rangle}{d \ln E} \\ &= X_0 \left(1 + \frac{1}{X_0} \frac{d\lambda_{\text{int}}}{d \ln E} - \frac{d \ln n_{\text{tot}}}{d \ln E}\right) \\ &= X_0(1 - B_\lambda - B_n). \end{aligned} \quad (2.24)$$

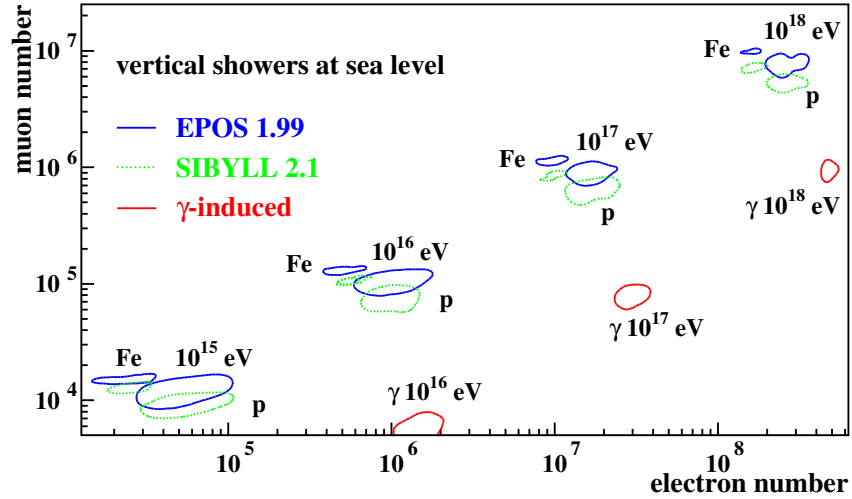


Figure 2.7: Number of muons and number of electrons in vertical air showers of different energy. The contour lines represent regions in which a fixed fraction of showers with proton or iron primary lie. The width of the contours then represent shower-to-shower fluctuations. Note that fluctuations are reduced for nuclei. This is due to the superposition of individual nucleon sub showers. Electromagnetic interactions inherently exhibit smaller fluctuations than hadronic interactions. Figure from Ref. [1].

If the multiplicity and interaction length in hadronic interactions were independent of energy ($B_\lambda = B_n = 0$), then for a pure composition the elongation rate of CR air showers would be the same as for photons (pure em. shower). Since the multiplicity and cross section have a small energy dependence, D_e is always smaller than for photon showers (*elongation rate theorem*) [13]. This will be discussed further in the context of the discussion of the predictions for cosmic ray interactions calculated with the new SIBYLL (Sect. 10).

Experimentally the longitudinal development and X_{\max} are more or less directly accessible through the energy deposit of em. particles in the atmosphere [14].

Particles at ground

In the vertical direction (inclination zero) the atmosphere has a depth of 1030 g/cm^2 (sea level). It increases with inclination by a factor $1/\cos(\theta)$, so that at $\theta = 60^\circ$ the ground is reached after traversing $\approx 2000 \text{ g/cm}^2$ of matter. Observing air showers with different inclination at ground, means one is effectively observing different stages in the development. Due to the very different attenuation of em. particles and muons in the atmosphere the relative fraction of these particles at ground changes with inclination but also with energy and between different primary particles. Considering a fixed inclination and energy, e.g. vertical 10^{19} eV particle (profiles in Fig. 2.5), the number of em. particles can be expected to be lower for a nucleus, since the maximum is reached higher up and attenuation is stronger.

For muons the behavior is not so evident. In the Heitler model the number of muons depends on the ratio of the primary energy to the energy where the cascade terminates and the ratio of the charged to the total number of pions

$$N_\mu = \left(\frac{E_0}{E_{\text{crit}}} \right)^\alpha, \quad \alpha = \frac{\ln n_{\text{ch}}}{\ln n_{\text{tot}}}. \quad (2.25)$$

Adding the superposition model, the number of muons produced in each sub cascade is reduced by a factor $1/A^\alpha$ compared to the proton primary and increased by a factor A , corresponding to the number of parallel cascades. The ratio of pion production α in the exponent was already shown (ISR measurement) to have a value close to one ($\alpha \approx 0.8 \dots 0.9$), so the dependence of the number of muons on the primary mass is small ($\mathcal{O}(1)$) but positive.

This can be seen in Fig. 2.7, where the combined dependence of the number of particles at ground on the primary energy and mass is shown. The number of electrons (drawn along x) is

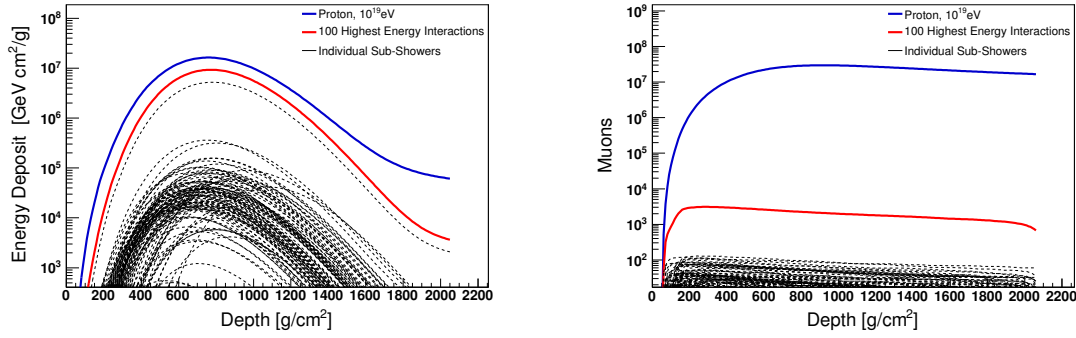


Figure 2.8: Sub showers and their influence on X_{\max} (left) and N_{μ} (right) [15].

lower for nuclei compared to protons which is in accordance with the stronger attenuation due to the higher X_{\max} . The number of muons (drawn along y) in showers initiated by protons and iron nuclei also differs but on a smaller scale.

As the figure suggests, the number of muons and electrons at ground is another observable that can be used to determine the mass composition.

2.3.3 Link to properties of hadronic interactions

Having determined the observables of air showers that are sensitive to the properties of the primary particle, the question is how do these observables depend on properties or observables of hadronic interactions? And what is the influence of uncertainties in the hadronic interactions on the air shower observables.

X_{\max}

From the previous discussion of the dependence of X_{\max} on the properties of the primary, it is clear that the shower maximum depends mostly on the properties of the first few interactions. Since, in real interactions the energy is not shared equally between the final state particles, but rather a single particle usually emerges that still carries most of the energy (so-called *leading particle effect* (see Sect. 5)), the most important interactions for X_{\max} will be the first few interactions of the leading particles, or in other words, the first highest energetic interactions.

Due to baryon number conservation and the fact that the primary particles are nucleons, the leading particles are mostly nucleons and therefore the first highest energetic interactions are proton-air interactions.

This dependency of X_{\max} on the first few interactions can be tested in simulations. In Fig. 2.8, on the left, the longitudinal profile of the energy deposited in the atmosphere (dominated by em.) of a 10^{19} eV proton is shown together with the contribution of the first 100 highest energy interactions and individual sub showers [15]. Of the 100 highest energetic sub showers, one dominates the profile and mostly determines the position of X_{\max} .

In terms of the properties of these first hadronic interactions, the balance between the number of produced particles and the way the energy is shared among those particles will be important. The variable to express the difference in energy between the leading particle and other produced particles is called the *inelasticity* κ . It is defined as the fraction of the primary energy carried by all particles other than the leading one

$$\kappa = \frac{E_{\text{non-lead}}}{E_0} = 1 - \frac{E_{\text{lead}}}{E_0}. \quad (2.26)$$

In the model where the energy is shared equally between all particles the inelasticity would be one, in case of elastic scattering (no additional particles produced) it would be zero. The inelasticity in the general case is weakly linked to the multiplicity through energy conservation,

since energy spent on particle production is not available for the leading particle. The non-leading particles, that make up most of the multiplicity, are centrally produced, which means they carry low momentum fractions and therefore take not much energy to produce. Picking up on the discussion on Feynman scaling from Sect. 2.2.3, a constant inelasticity with energy would mean Feynman scaling is preserved, since $Ed\sigma/dE \sim \text{const.}$. The strong violation of Feynman scaling that is observed in the central region, only has a small effect on the inelasticity because the fragmentation region is only affected indirectly through energy conservation.

The larger the inelasticity and multiplicity are, the less generations it takes until the primary energy is dispersed and the threshold for particle production is reached, so the shower maximum is anti-correlated with inelasticity and multiplicity (see Fig. 2.10).

N_μ

The number of muons in air showers, in contrast to the shower maximum, does not depend so much on the first interactions. The reason is that muon production is linked to the termination of the hadronic cascade (particle decay). In the Heitler-Matthews model the cascade grows exponentially with each hadronic generation n_{ch}^n , so, such is the nature of exponential growth, essentially all pions, that will produce muons, are created in the final stage just before the decay.

Outside the model, of course, the multiplicity in each interaction undergoes fluctuations and decreases as the interaction energy decreases along the shower, and there are also other particles than pions produced, but none of these introduce large enough deviations to change the general behavior. The change in multiplicity with energy, for example, is only logarithmic.

In Fig. 2.8 the effect of the 100 highest energetic sub showers on the profile of muons in the atmosphere is shown. The contribution from these interactions is clearly negligible.

One way to escape the cascade mechanism is premature decay. Particles that decay into muons before they can interact again (large critical energy), could possibly shift the weight in muon production from the late stages in development to the first few interactions. However, none of the particles that make up the majority of the multiplicity in hadronic interactions, has such short lifetime [16].

For particles that are produced less often but have a short lifetime and decay into muons the effect on the cascade is small and the contribution to the number of muons compared to muons from the cascade is certainly negligible. One important difference for these muons is that they may be highly energetic, which is unlikely for muons from pions or kaons since high energetic pions or kaons are very likely to interact before decaying. Muons originating from short lived particles are called *prompt muons*, in general they are not very important for individual air shower measurements but they play an important role in the inclusive atmospheric flux of muons and neutrinos (see Sect. 2.4) [17].

Another mechanism for muon production that is not included in Eq. 2.25 is the effect of particles that do not decay into non-hadronic particles. In that case the critical energy is at the absolute limit of particle production, which for hadrons is the pion mass. Since such particles would continue to interact and produce new particles (pions) they are part of the cascade (Eq. 2.25) but with lower value for the energy where they would drop out of the cascade $E_{\text{crit}} \rightarrow \mathcal{O}(m_\pi)$. So far the only particles known to decay only to other hadrons are baryons. *Baryon production* is considered one of the most effective ways of increasing the number of muons in air showers [18, 19, 20]. It will be discussed in context of SIBYLL in Sect. 7.

In summary, muons are mostly generated in the late stages of the air shower. The interactions relevant are mostly pion interactions, since pions dominate the hadronic cascade in the late stages. However, since each step of the cascade depends on the previous one, also the high energy interactions will have an influence on the final number of muons.

This dependency of the number of muons on the full range of interaction energies in air showers makes it very susceptible to uncertainties in hadronic interactions. In particular, the understanding of pion and kaon interactions at high energy has not been tested by experiment yet. Misrepresentations of these interactions then could have large effects on interpretation of air shower observables.

In Fig. 2.9 a consistency check for the modeling air showers is shown [21]. The test is in the form of a comparison between two air shower variables that are both sensitive to the cosmic ray

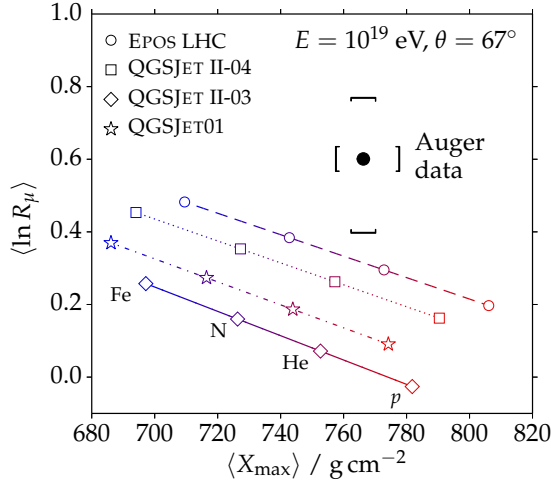


Figure 2.9: Comparison of measurements of X_{\max} and N_{μ} [21]. Selecting highly inclined showers means the signal at ground is dominated by muons. Note that the data lie in a region outside all model predictions.

composition but depend on different air shower components and therefore on different properties of hadronic interactions. The first variable is $\langle X_{\max} \rangle$ and it is determined by the development of the em. component. As it has been explained before the em. component is influenced the most by the first few high energy interactions. The second variable is related to the number of muons in the air shower at the surface of the Earth. The muons are produced in the hadronic component.

Our current best knowledge of hadronic interactions is represented by the models EPOS-LHC and QGSJET II-04 (models tuned to LHC measurements) [22, 23]. The difference between the two model lines represents the uncertainty introduced by the extrapolation of one order of magnitude in energy ($10^{19} \text{ eV} \simeq 100 \text{ TeV cm.}$). The fact that the model predictions for $\langle X_{\max} \rangle$ and N_{μ} are different to the experimental data has then to be interpreted as a misrepresentation of hadronic interactions in the models. In light of the strong dependence of the number of muons on hadronic interactions, in particular the less known meson interaction (here the extrapolation is 6 to 7 orders of magnitude!), it is quoted as the ‘muon number problem’. The figure shown here is only one of the many manifestation of this discrepancy.

The connections between hadronic interactions and air shower observables are summarized in Fig. 2.10. The effect of a property of a hadronic interaction, like multiplicity, cross section or inelasticity, can be demonstrated by varying that property in a model (here SIBYLL), simulating several air showers and then comparing air shower observables between the modified and the default model.

The energy of interactions in a single air shower extends over a large range. Scaling the interaction properties the same way at all energies would break the intrinsic energy dependence of the model. The figure is therefore constructed by varying the model at high energy (10^{19} eV) by a factor f_{19} . For lower energies the modification is scaled down [24].

In the figure, the $\langle X_{\max} \rangle$ and N_{μ} of a proton initiated air showers with a primary energy of 10^{19} eV are shown as a function of the modification factor at the primary energy (f_{19}). The different lines represent the effects of the different interaction properties.

The figure confirms what has been argued before, namely that X_{\max} is influenced by the cross section and quantities that affect the dispersion of energy into particles (inelasticity and multiplicity). For the number of muons the ratio between charged and neutral pions has by far the strongest influence of the quantities considered here. Cross section and inelasticity are not particularly influential. The multiplicity dependence for the number of muons is opposite to the one for the shower maximum.

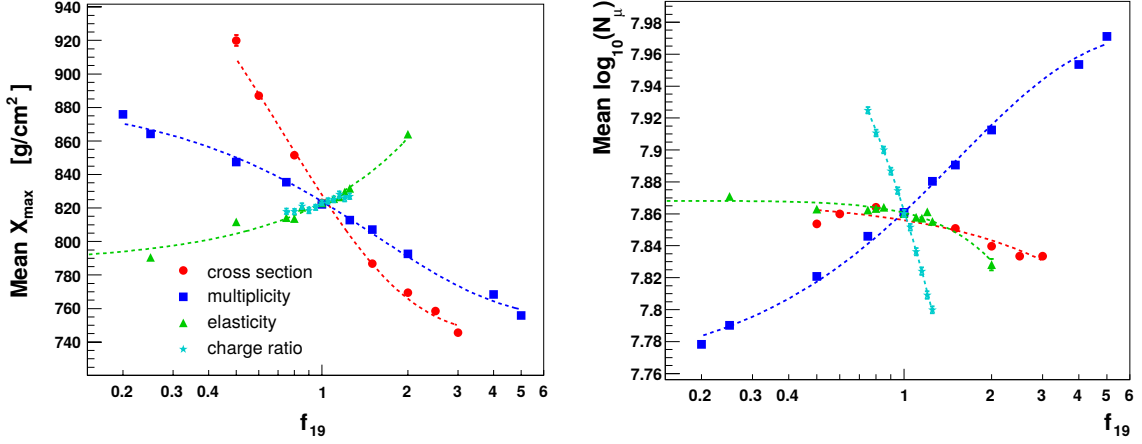


Figure 2.10: Dependency of air shower observables on properties of hadronic interactions [24]. Shower maximum (left) and number of muons (right). The inelasticity, cross section, multiplicity and charge ratio of pions are varied continuously so that the change is maximal at 10^{19} and reduced at lower energies.

2.4 Inclusive atmospheric fluxes

In the previous section the development and observables of individual extensive air showers were discussed. The detection of an air shower with particle detectors at ground requires timing information. The particles from a single air shower are identified by a coincidence measurement [25]. Without the timing information particles from different air showers can not be distinguished.

The measurement in that case is the inclusive measurement of particle fluxes in the atmosphere. By placing the detector underground the particles that are measured can be limited to muons and neutrinos. By going even deeper or looking for particles coming up, the flux of neutrinos in the atmosphere can be measured.

These inclusive fluxes still contain information about the primary cosmic ray spectrum (Fig. 2.1). Since the flux is the product of all air showers in the atmosphere it also depends on the properties of hadronic interactions.

With the recent measurement of astrophysical neutrinos by the IceCube experiment [5]. An accurate prediction of the contribution of air showers to the inclusive flux of neutrinos has become very important. The measurement by IceCube shows that the inclusive flux of neutrinos is the combination of the atmospheric flux and a primary (extra)galactic flux. To determine the primary flux the atmospheric flux needs to be subtracted from the measurement.

Cascade equations

The atmospheric flux, or any particle flux in a medium, can be described by the *cascade equations*. The equations describe how the flux of particles of different type changes under the influence of interactions with the surrounding medium and decay of the particles

$$\frac{d\Phi(E_i, X)}{dX} = -\frac{\Phi_i(E_i, X)}{\lambda_i} - \frac{\Phi_i(E_i, X)}{d_i} + \sum_{j=i}^J \int_E^\infty \frac{F_{ji}(E_i, E_j)}{E_i} \frac{\Phi_j(E_j, X)}{\lambda_j(E_j)} dE_j. \quad (2.27)$$

The first two terms describe the reduction of the flux due to decay and inelastic interaction. The third term describes the increase due to particle production. Its structure determines how the properties of hadronic interactions influence the atmospheric flux.

The first factor in the integrand, $F_{ji}(E_i, E_j)$, is the invariant inclusive yield for the production of particle i with energy E_i in the interaction of particle j with the medium

$$F_{ji}(E_i, E_j) = E_i \frac{dn_i(E_i, E_j)}{dE_i} \quad (2.28)$$

$$\sim \frac{1}{\sigma_{\text{inel}}} \int E_i \frac{d^3\sigma_{j+\text{Air} \rightarrow i+X}}{d^3\vec{p}_i} d^2\vec{p}_T. \quad (2.29)$$

The invariant cross section, $E_i d^3\sigma/d^3\vec{p}_i$ has been introduced in a previous section. The second factor is the number of collisions of particle j with air that occur in the interval $X, X + dX$.

Using the primary flux of cosmic rays as initial condition at $X = 0$ (top of atmosphere), the inclusive flux of any type of particle produced in hadronic interactions can be calculated by solving these equations.

In principle these equations also describe single air showers (initial flux: $A\delta(E - E_0/A)$), the solution would however correspond to the average air shower with that energy. Since the fluctuations in hadronic interactions can be substantial, individual air showers may deviate a lot from the average shower, which is why full MC simulations are needed to analyze measurements. The predictions for $\langle X_{\text{max}} \rangle$ and the average number of muons as a function of primary energy, that are presented in Sect. 10.1, have been calculated using a numerical implementation of the cascade equations [26].

Chapter 3

The hadronic interaction model Sibyll 2.1

A model, in a general sense, is a construct that mimics the behavior or appearance of the natural world in a simplified way. Models play an essential role in physics because they help develop deeper understanding. It is interesting to note that most times understanding advances not through the success of a model but through its failure.

Interaction models, or Monte Carlo (MC) event generators, are an integral part of high energy physics (HEP). They are helpful and necessary for multiple reasons. Firstly they bridge the lack of understanding we have in the long distance behavior of QCD. Secondly they enormously simplify the comparison between experimental data and theory. Even if there were an analytic theory for all interactions, carrying out the multidimensional integration that corresponds to a measurement at one of the LHC detectors is certainly unpractical.

The overall features of hadrons and their interactions have been described in the previous section. How can these be implemented in a model? The general approach is to factorize the problem into parts that treat the different (length, time, momentum)-scales (see Fig. 3.1). The short length scales (hard) can be calculated in the perturbation expansion of QCD. Long length scales (soft) are typically described with a phenomenological model.

HEP models focus on describing hard processes. Since the experiments also trigger on hard processes (large p_{\perp}) in order to reduce the interaction rate given by the total cross section ($\mathcal{O}(100\text{ mb})$) down to weak interaction scales ($\mathcal{O}(\text{ nb})$) (see Fig. 2.2), HEP models can neglect most processes. Often the description of *soft interactions* is limited to the contribution to the phase space of hard process, the so-called underlying event. For this it is enough to tune the soft interaction model on a small data set with relaxed trigger before each accelerator run ('tunes'). While this procedure allows the extraction of the hard physics from experimental data, it does not give a reliable prediction at high energies.

CR models on the other hand, need to focus on the dominant processes that make up the bulk of the total cross section, since those will also be the processes dominating air shower development. These are mostly soft processes. Also the description of the interaction should be as general as possible to allow the reliable extrapolation to high energy, different beams (mesons!) and different targets (nuclei).

SIBYLL is one of the interaction models designed for the description of hadronic interactions in the context of cosmic rays. It follows the general structure of interaction models in that it factorizes hard and soft interactions, in particular parton scattering (Sect. 3.1) is separated from hadronization (Sect. 3.3).

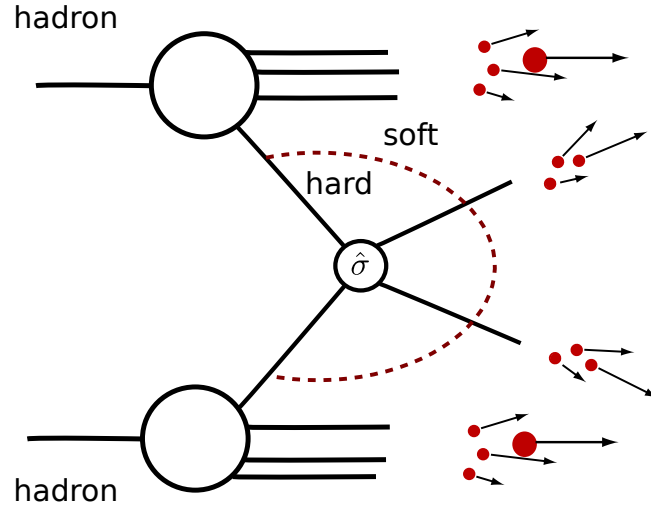


Figure 3.1: Schematic view of hadron collision.

3.1 Cross section and scattering amplitude

3.1.1 Eikonal and the dual parton model

The interaction picture in SIBYLL [27] is based on the Dual Parton Model (DPM) [28, 29, 30], which combines concepts from Regge Field Theory [31] with ideas from topological expansion of QCD [32] to arrive at an inclusive description of particle production in hadron-hadron collisions.

The basis is that hadron interactions are described by the exchange of combined objects of partons. In cases where color charge is transferred, the hadrons are linked with a strong color field from which particles are produced. If there is no net color exchange the interaction is elastic or diffractive.

At large momentum transfers (Q^2) or on small length scales the exchanged objects correspond to the quarks and gluons in QCD. In soft processes (small Q^2 , large distance) it is seen as a structured combination of quarks and gluons (so-called *Pomeron*) [31].

An additional complication arises from the fact that multiple exchanges or scatterings can occur. In order to combine the soft and hard channels to make up the observed total cross section the so-called *eikonal approximation* is used.

Starting with the optical theorem and the assumption that the amplitude is an analytic function, a general expression for the amplitude in terms of so-called eikonal functions can be derived. The term eikonal stems from geometrical optics where the eikonal model is used to describe the scattering of light rays. Comparing the size of the proton of 0.7 fm with the wavelength of a proton with $p_{\text{Lab}} = 10 \text{ GeV}/c$ which is $\lambda \simeq \hbar c/p \simeq 0.02 \text{ fm}$, shows that the situation in high energy physics is similar [33]. The central element in the model are *eikonal functions* χ that correspond to the phase shift that the incoming wave exhibits when it is scattered. Multiple scatterings then simply correspond to adding up multiple phase shifts.

The same mechanism is used to represent multiple interactions in high energy particle collisions. The essential feature of the eikonal representation is that the conservation of probability (unitarity) is obeyed by construction.

The appropriate coordinates to derive the probability of interaction from the parton structure of hadrons are coordinates in impact parameter space. The scattering amplitude $f(s, \vec{q})$ is therefore usually replaced by its Fourier transform $\Gamma(\vec{b})$, the so-called *profile function*,

$$f_{\text{hp}}(s, \vec{q}^2) = \frac{ik}{2\pi} \int e^{i\vec{q}\cdot\vec{b}} \Gamma(\vec{b}, s) d^2\vec{b}. \quad (3.1)$$

The profile function is given by the eikonal function $\Gamma(b, s) = i/2(1 - e^{-\chi(b, s)})$. To include soft and hard interactions, the eikonal function is written as

$$\chi(b, s) = \chi_{\text{hard}}(b, s) + \chi_{\text{soft}}(b, s). \quad (3.2)$$

The cross sections and the eikonal function are related by

$$\sigma_{\text{inel}} = \pi \int db^2 [1 - e^{-2\chi(b, s)}] \quad (3.3)$$

$$\sigma_{\text{tot}} = 2\pi \int db^2 [1 - e^{-\chi(b, s)}] \quad (3.4)$$

$$\sigma_{\text{el}} = \pi \int db^2 [1 - e^{-\chi(b, s)}]^2. \quad (3.5)$$

The measure πdb^2 is what remains of the integration in transverse space $d^2\vec{b}$ after applying azimuthal symmetry and using b^2 as integration variable.

In a probabilistic interpretation the eikonal function χ can be related to the average number of interactions at a given impact parameter

$$\chi(b, s) = \frac{1}{2} n_{\text{int}}(b, s).$$

The average number of interactions quite clearly depends on the number and the spatial distribution of partons in the hadrons, the range of their interaction and the probability of the parton interaction. The spatial distribution is given by the profile functions (impact parameter space PDFs) $A_i(\vec{b})$. The range of interaction is characterized by another profile function $A_{\text{int}}(\vec{b})$. The overlap of all three determines the probability of interaction from a geometrical point of view

$$A_{12}^i(\nu_1, \nu_2, \vec{b}) = \int d^2\vec{b}_1 d^2\vec{b}_2 d^2\vec{b}_3 A_1(\nu_1, \vec{b}_1) A_2(\nu_2, \vec{b}_2) A_{\text{int}}^i(s, \vec{b}_3) \delta^{(2)}(\vec{b}_1 - \vec{b}_2 + \vec{b}_3 - \vec{b}). \quad (3.6)$$

\vec{b}_i are different impact parameters in the collision (see Fig. 3.2). \vec{b} is the transverse distance between the centers of the colliding hadrons, which is what is usually referred to as impact parameter. \vec{b}_1 and \vec{b}_2 are the distances of the interacting partons to the centers of their respective parent hadrons and \vec{b}_3 is the transverse distance between the partons. ν_i are parameters of the profiles, typically describing the width. Weighting the overlap with the partonic $2 \rightarrow 2$ cross sections accounts for the quantum mechanical nature of the interaction itself

$$n_{\text{int}}(b, s) = A_{12}(b, s) \sigma_{\text{int}}(s). \quad (3.7)$$

The entire eikonal function that defines the scattering amplitude is then

$$\chi(b, s) = \frac{1}{2} \sigma_{\text{hard}}(s) A_{12}^{\text{hard}}(b, s) + \frac{1}{2} \sigma_{\text{soft}}(s) A_{12}^{\text{soft}}(b, s). \quad (3.8)$$

3.1.2 Hard interactions

The total cross section for a hard interaction between two partons is given by the convolution of the $2 \rightarrow 2$ scattering cross section in QCD $\hat{\sigma}(\hat{s}, \hat{t})$ with the PDFs $f(x, Q^2)$.

$$\begin{aligned} \sigma_{\text{QCD}}(s, p_T^{\text{min}}) &= K \int dx_1 \int dx_2 \int dp_T \\ &\times \sum_{i,j,k,l} \frac{1}{1 + \delta_{k,l}} f_{a,i}(x_1, Q^2) f_{b,j}(x_2, Q^2) \frac{d\sigma_{\text{QCD}}^{i,j \rightarrow k,l}(\hat{s}, \hat{t})}{dp_T} \Theta(p_T - p_T^{\text{min}}), \end{aligned} \quad (3.9)$$

All partonic $2 \rightarrow 2$ processes to leading order are included in the model and higher order corrections are accounted for with the K -factor. For the parton distribution functions (in momentum space) the Glück, Reya and Vogt [34, 35] parameterizations are chosen.



Figure 3.2: Profile overlap in case of hard (left) and soft (right) interactions.

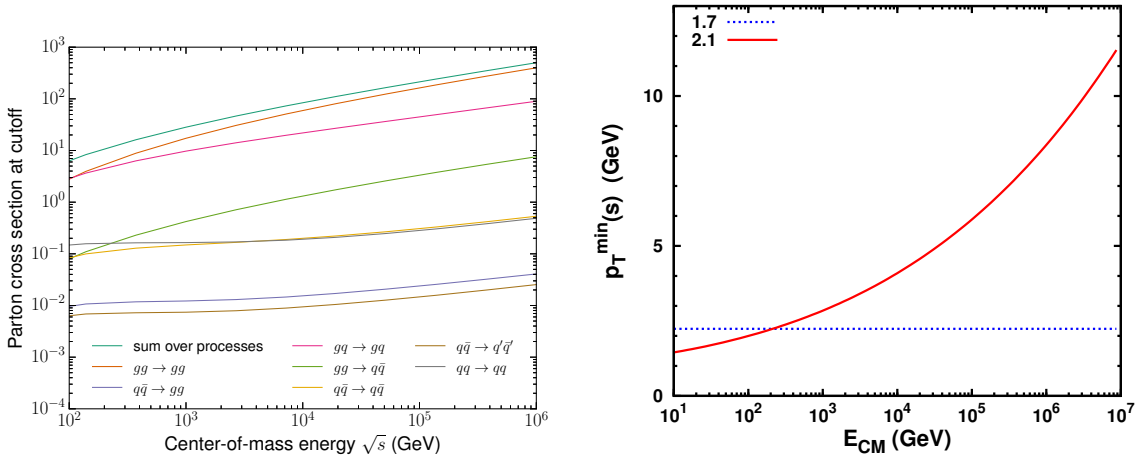


Figure 3.3: Left: Value of the parton scattering cross sections at the transverse momentum cutoff. Right: Value of the p_{\perp} -cutoff as a function of energy as it is implemented in SIBYLL 2.1.

The definition of hard scattering is given by the cutoff in transverse momentum p_{\perp}^{\min} . It is chosen energy dependent to include effects of saturation, i.e. the break down of the assumption of independent $2 \rightarrow 2$ scattering due to high parton densities.

In principle saturation should be impact parameter dependent but since this would break the factorization between the geometry and micro physics in Eq. 3.7 and would complicate the implementation immensely (see Sect. 3.2), an effective saturation model is used by scaling the p_{\perp} cutoff. The energy dependence is constructed from the geometrical saturation conditions [36, 37] that the total area covered by gluons is less than the size of a proton.

$$\frac{\alpha_s(p_{\perp}^2)}{p_{\perp}^2} \cdot xg(x, p_{\perp}^2) \leq \pi R_p^2, \quad (3.10)$$

The transverse size of the gluons is roughly given by α_s/p_{\perp}^2 and $g(x, p_{\perp}^2)$ the gluon density.

On the level of the profiles in Eq. 3.6 hard interactions are seen to be point like (see also Fig. 3.2), so A^{hard} is set to a Dirac delta function.

In Fig. 4.3 of the next section the overlap profile $A_i(b)$ for hard interactions is shown with two different values for the proton profile width.

3.1.3 Soft interactions

The cross section for soft parton interactions is parameterized by

$$\sigma_{\text{soft}}(s) = X \left(\frac{s}{s_0} \right)^{\Delta_{\text{eff}}} + Y \left(\frac{s}{s_0} \right)^{-\epsilon}, \quad (3.11)$$

corresponding to calculations based on Pomeron and Reggeon exchanges [38].

In contrast to hard interactions, soft interactions are assumed to take place over longer impact parameter distances (see Fig. 3.2). The profile function for the soft interactions ($A^{\text{soft}}(s, \vec{b})$ in Eq. 3.6) is taken to be a Gaussian,

$$A^{\text{soft}}(s, \vec{b}_3) = \frac{1}{4\pi B_s(s)} \exp\left[-\frac{|\vec{b}_3|^2}{4B_s(s)}\right], \quad (3.12)$$

and the energy dependent width

$$B_s(s) = B_0 + \alpha'(0) \ln\left(\frac{s}{s_0}\right). \quad (3.13)$$

$\alpha'(0)$ is a parameter of Regge theory which takes the value $\alpha'(0) \approx 0.25 \text{ GeV}^{-2}$.

Hadron profiles

The hadron profiles A_i are chosen according to the measured em. form factors [39]

$$A_p(\nu_p, \vec{b}) = \nu_p |\nu_p \vec{b}| K_1(|\nu_p \vec{b}|). \quad (3.14)$$

For mesons

$$A_m(\nu_m, \vec{b}) = \frac{1}{(2\pi)^2} \int d^2k_T \left(1 + \frac{k_T^2}{\nu_m^2} + \eta \left(\frac{k_T^2}{\nu_m^2}\right)\right)^{-1} e^{i\vec{k}_T \cdot \vec{b}}. \quad (3.15)$$

For protons the width parameter is $\nu_p = 0.71 (\text{GeV}/c)^2$, for mesons it is $\nu_m = 0.54 (\text{GeV}/c)^2$.

In the case of a hard interaction for protons the overlap integral in Eq. 3.6 is just the convolution of two proton form factors

$$A_{pp}^{\text{hard}}(\nu_p, \vec{b}) = \frac{\nu_p^2}{96\pi} (\nu_p |\vec{b}|)^3 K_3(|\nu_p \vec{b}|). \quad (3.16)$$

In the case of a hard interaction between meson and proton the overlap integral between the two different form factors is more complex

$$A_{mp}^{\text{hard}}(\nu_p, \nu_m, \vec{b}) = \frac{1}{4\pi} \frac{\nu_p^2 \nu_m^2}{\nu_m^2 - \nu_p^2} \left(\nu_p |\vec{b}| K_1(|\nu_p \vec{b}|) - \frac{2\nu_p^2}{\nu_m^2 - \nu_p^2} [K_0(|\nu_p \vec{b}|) - K_0(|\nu_m \vec{b}|)] \right). \quad (3.17)$$

K_i are the modified Bessel functions of the second kind.

For soft interactions the overlap integral between the hadron form factors and the Gaussian profile of the interaction can only be calculated numerically. To keep the expressions in analytic form, for soft interactions the hadron form factors are approximated by exponentials instead of dipoles. The overlap integral then corresponds to the convolution of three Gaussians, which is also given by a Gaussian

$$A_{pp}^{\text{soft}}(s, \vec{b}) = \frac{1}{4\pi(2B_p + B_s(s))} \exp\left[-\frac{\vec{b}^2}{4(2B_p + B_s(s))}\right]. \quad (3.18)$$

The parameter B_p is the width parameter of the exponential form factor (corresponding to ν_p). It is treated as a free parameter, together with B_0 in Eq. 3.13.

3.1.4 Diffraction dissociation

Of the event types introduced in Sect. 2.2.2 only inelastic and elastic events have been covered so far (see Eq. 3.3). To separate inelastic interactions further into diffractive and non-diffractive interactions another model inspired by optics is used.

When describing the scattering of light on a polarized target, the light wave is written as a superposition of two polarization states that interact differently with the target. The scattered wave then exhibits interference effects when the differently interacting polarization states are put back together.

For hadron interactions a similar approach can be used (called the Good-Walker model [40]) by defining the hadron as a superposition of the hadron (h) and the diffractively excited hadron (h^*)

$$|h\rangle \rightarrow c_1|h\rangle + c_2|h^*\rangle . \quad (3.19)$$

The different event types can then be described as transitions from hadron to excited hadron states within the eikonal model. In particular, diffraction dissociation can be written as,

$$|h_1, h_2\rangle \rightarrow |h_1^*, h_2\rangle \quad \text{single diff., beam} \quad (3.20)$$

$$|h_1, h_2\rangle \rightarrow |h_1, h_2^*\rangle \quad \text{single diff., target} \quad (3.21)$$

$$|h_1, h_2\rangle \rightarrow |h_1^*, h_2^*\rangle \quad \text{double diff. .} \quad (3.22)$$

Diffractive excitation is parameterized as fractions β (diff. coupling) of the elastic amplitude \mathcal{M} , i.e. the transition probability from A to A^* in a AB collision is written as

$$\langle A^*B|\mathcal{M}_{\text{int}}|AB\rangle = \beta_A \mathcal{M}_{\text{Born}} . \quad (3.23)$$

Similarly the transitions from excited to excited and de-excitation can be defined. Representing $|AB\rangle$ by a vector in R^4 the eikonal function (Eq. 3.8) can be generalized to a 4x4 matrix. The matrix elements are given by transition expressions like Eq. 3.23

$$\hat{\chi}(s, b) = \begin{pmatrix} 1 & \beta_Y & \beta_Z & \beta_Y \beta_Z \\ \beta_Y & 1 - 2\alpha_Y & \beta_Y \beta_Z & \beta_Z (1 - 2\alpha_Y) \\ \beta_Z & \beta_Y \beta_Z & 1 - 2\alpha_Z & \beta_Y (1 - 2\alpha_Z) \\ \beta_Y \beta_Z & \beta_Z (1 - 2\alpha_Y) & \beta_Y (1 - 2\alpha_Z) & (1 - 2\alpha_Y)(1 - 2\alpha_Z) \end{pmatrix} \chi(s, b) . \quad (3.24)$$

The elastic cross section in Eq. 3.5 now becomes

$$\sigma_{\text{el}}^{\text{AB}} = \pi \int db^2 \left| \langle AB|(1 - e^{-\hat{\chi}(s,b)})|AB\rangle \right|^2 . \quad (3.25)$$

It was already argued that diffractive interactions are very similar to elastic scattering as both are coherent scattering processes. The association that is made in the previous chapter by describing diffraction dissociation as an element of inelastic scattering is, while strictly correct, misleading when it comes to the calculation. Diffraction dissociation is calculated as an element of elastic scattering, e.g. the cross section for single diffraction dissociation $AB \rightarrow A^*B$ is

$$\sigma_{\text{SD},A}^{\text{AB}} = \pi \int db^2 \left| \langle A^*B|(1 - e^{-\hat{\chi}(s,b)})|AB\rangle \right|^2 , \quad (3.26)$$

and similarly for double diffraction with $A \rightarrow A^*$ and $B \rightarrow B^*$. To evaluate these expressions the eikonal matrix has to be diagonalized. The corresponding mathematical expressions have been omitted here [41].

The Good-Walker approach is only valid for sufficiently long-lived excitation states. In general, the higher the mass of an excitation or resonance is the shorter is its lifetime. At high energies, the coherence limit

$$\sqrt{|t|} = (1 - x) m_p \leq m_\pi \quad , \quad \frac{M_x^2}{s} \leq \frac{m_\pi}{m_p} \approx 0.15 \quad (3.27)$$

allows high excitation masses that would correspond to very short lived states. These so-called *high-mass diffraction* events in SIBYLL are assigned to the inelastic cross section. They are taken to make up a fixed fraction δ of the events with one hard and/or one soft interaction

$$\sigma_{\text{hm}}^{\text{SD}} = \delta (\sigma_{1,0} + \sigma_{0,1}) , \quad (3.28)$$

$$\sigma_{\text{hm}}^{\text{DD}} = \delta^2 (\sigma_{1,0} + \sigma_{0,1} + \sigma_{1,1}) + \beta_Y^2 \sigma_{\text{lm}}^{\text{SD,Z}} + \beta_Z^2 \sigma_{\text{lm}}^{\text{SD,Y}} . \quad (3.29)$$

δ is set to 0.1 according to HERA data, where 10% of events in deep inelastic scattering with low x (large Q^2) still appear to be diffractive [42].

$\sigma_{n,m}$ in Eq. 3.29 refers to the cross section for n soft and m hard interactions. It is essentially given by two Poissonian distributions with averages $n_{\text{soft}}(s, \vec{b})$ and $n_{\text{hard}}(s, \vec{b})$,

$$\begin{aligned} \sigma_{N_s, N_h} = \int d^2 \vec{b} \sum_{k=1}^4 \Lambda_k \frac{[\lambda_k n_{\text{soft}}(s, \vec{b})]^{N_s}}{N_s!} \frac{[\lambda_k n_{\text{hard}}(s, \vec{b})]^{N_h}}{N_h!} \\ \times \exp \left[-\lambda_k (n_{\text{soft}}(s, \vec{b}) + n_{\text{hard}}(s, \vec{b})) \right] . \end{aligned} \quad (3.30)$$

The coefficients Λ_k, λ_k can be determined from the eikonal matrix (Eq. 3.24) after it has been diagonalized.

The complete expressions for the eikonal matrix, the transitions and the profile functions can be found in Ref. [27].

3.1.5 Nuclear interactions

Interactions in the atmosphere take place between hadrons and nuclei, so the model described so far has to be extended to include nuclear targets to be useful for air shower simulations.

In SIBYLL this is accomplished by means of the *Glauber model* [43, 44]. It is based on the same multiple scattering picture used before for hadron-hadron interactions (historically correct the multiple parton interaction picture in hadron collisions is inspired by Glauber theory). The essential feature is again factorization, i.e. the different hadron-nucleon interactions in a hadron-nucleus collision are treated as independent. The nuclear profile function Γ_{hA} is given by the product of individual hadron-nucleon profiles

$$\Gamma_{hA}(\vec{b}, \vec{s}_1 \dots \vec{s}_A) = 1 - \prod_{j=1}^A \left[1 - \Gamma_{hN}(\vec{b} - \vec{s}_j) \right] , \quad (3.31)$$

where \vec{b} is the impact parameter of the hadron with the nucleus and \vec{s}_i are the impact parameters of the nucleons in the target nucleus. The hadron-nucleon profiles (impact parameter amplitudes) are related to the eikonal functions used above by $\Gamma_{hN} = i/2(1 - e^{-\chi(b,s)})$.

The Glauber model is described in more detail in Sect. 8, where the extension of the Glauber model to include inelastic intermediate states is discussed.

3.2 Event generation

In the previous section it was described what types of events are included in the model and how their cross sections are calculated. The calculations of the partial cross sections for n soft and m hard interactions can be done ahead of time and the results stored in tables, increasing the performance of the model. How the parton final state is generated from these tables is described in the following.

It should be noted that the implementation in the event generator is less detailed than that in HEP generators such as PYTHIA [45] or HERWIG [46]. For the sake of higher performance the implementation is also not entirely consistent with the amplitude level calculations as should become clear in the following.

3.2.1 Non-diffractive events

The basic non-diffractive interaction in the model involves one soft interaction and it produces two strings stretched between the valence quarks (see Fig. 3.4). The flavors of the valence quarks are quark-antiquark combination for mesons and quark-diquark combination for baryons. The fraction of momentum carried by the valence quarks is determined from $1/\sqrt{x}$ with the pole regulated by a minimal mass μ and large x suppressed by $(1-x)^\alpha$

$$f_q(x) = \frac{(1-x)^\alpha}{(x^2 + \mu^2/s)^{1/4}}, \quad (3.32)$$

μ is set to 0.35 GeV and α is 3 for baryons and 2 for mesons. The other valence quark/diquark is assigned the remaining fraction $1 - x_q$.

The valence quarks are also assigned a transverse momentum from a Gaussian distribution with the mean value given by

$$\langle p_T \rangle = \left[p_0 + 0.08 \log_{10} \left(\frac{\sqrt{s}}{30 \text{ GeV}} \right) \right] \text{ GeV}/c. \quad (3.33)$$

p_0 is 0.3 GeV/c for u, d -quarks, 0.45 GeV/c for s -quarks and 0.6 GeV/c for diquarks.

In each additional interaction two more strings are produced. The probability for multiple interactions is determined from the ratio of the cross section in Eq. 3.30 and the inelastic cross section

$$P_{N_s, N_h} = \frac{\sigma_{N_s, N_h}}{\sigma_{\text{inel}}}. \quad (3.34)$$

The two strings from the additional hard or soft interactions (*minijets*) are created in a closed color loop, i.e. stretched between quark pairs (see Fig. 3.4), corresponding to $gg \rightarrow gg$. If the mass of the strings is below $E_{q\bar{q}} = 8 \text{ GeV}$ the two strings are merged into one, corresponding to $q\bar{q} \rightarrow q\bar{q}$ scattering. In contrast, the hard cross section in Eq. 3.9 includes all LO contributions from 4 light flavors and gluons. Sampling all these contributions explicitly, however would be too expensive computationally (would need to sample color flow too!). Therefore, since these interactions populate parts of phase space that (presumably) have little effect on air shower development, they are approximated by a single configuration.

In the same spirit, the kinematics of the hard minijets are determined from an effective PDF [47] constructed from the Eichten et al. [48] parameterizations

$$f(x) = g(x) + \frac{4}{9} [q(x) + \bar{q}(x)], \quad (3.35)$$

and the transverse momentum is determined from $d\sigma/d\hat{t} \sim 1/\hat{t}^2$, evidently with $\hat{t} > (p_T^{\text{min}})^2$.

The soft kinematics are determined from a $1/x$ distribution for the momentum fraction and from a Gaussian distribution for p_\perp .

3.2.2 Diffractive events

The fraction of events that are diffractive is determined from the ratio between the diffractive cross sections and the inelastic cross section

$$P_{\text{diff}} = \frac{\sigma_{\text{SD}}}{\sigma_{\text{inel}}}. \quad (3.36)$$

The excitation mass is determined from a $1/M^2$ distribution with the lower limit set to 1.2 GeV^2 , 0.2 GeV^2 and 0.6 GeV^2 for protons, pions and kaons respectively. The upper limit is universally determined by the coherence condition $\zeta_{\text{max}} = 0.2s$, where s is the cm. energy squared.

The transverse momentum is determined from the elastic scattering peak

$$\frac{d\sigma_{\text{ela}}}{dt} \sim e^{-Bt}, \quad (3.37)$$

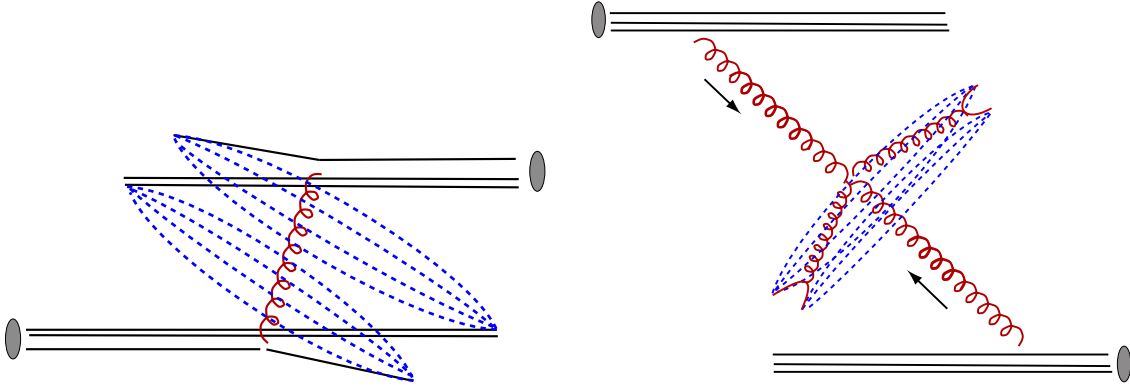


Figure 3.4: Sketch of string configuration in SIBYLL. Left: First soft interaction attached to valence quarks. Right: Additional hard or soft scattering (minijets).

with energy dependent slope parameter $B(s) = a - b \ln(M^2/s)$.

The hadronization of the diffractive system is split into separate regions. Low diffractive masses correspond to coherent interactions where single partons are unlikely to be resolved so a soft break up of the hadron through phase space decay is used. Higher masses can have incoherent character so the hadron is split into two flavors and then hadronized via string fragmentation. The threshold is chosen to be at $\Delta E = M_X - m_{\text{beam}} = 0.7$. For even higher masses ($\Delta E > 10$) the structure of the exchanged object is resolved and the entire system is hadronized via π^0 -hadron scattering.

3.3 Hadronization

In the previous sections the modeling up to the parton interactions has been described. The final state of which were parton configurations or excited hadrons. The particles that are observed in the detector or that form cascades in the atmosphere are long-lived hadrons, mostly pions, kaons and nucleons. The process that transforms the partonic final state of hadron scattering into these hadrons is called *hadronization*. There are two mechanisms for this included in SIBYLL, *string fragmentation* and *phase space decay*.

3.3.1 String fragmentation

String fragmentation in SIBYLL is based on the original Lund algorithm [49, 50] that describes the fragmentation of color fields into hadrons.

As the name suggests in the model the hadronization process between two color charges is seen as the stretching of a string. As the string stretches, it breaks into shorter pieces through the appearance of new color charges (see Fig. 3.5). This picture is motivated from observations of the spectroscopy of heavy quarkonia ($c\bar{c}, b\bar{b}$ -states) that can be described by assuming a central potential with a linear long-distance term for the strong interactions

$$V(r) = -\frac{\alpha}{r} + \kappa r. \quad (3.38)$$

With such a potential the energy in the field between two separating charges increases linearly with distance, just like in a rubber string.

The string breaking mechanism is seen as the promotion of $q-\bar{q}$ fluctuations from the vacuum into real particles, fueled by the field energy. The energy fraction that is kept in the final hadrons is determined by the Lund fragmentation function

$$f(z) = \frac{(1-z)^{a_i}}{z} \exp\left(\frac{-bm_T^2}{z}\right). \quad (3.39)$$

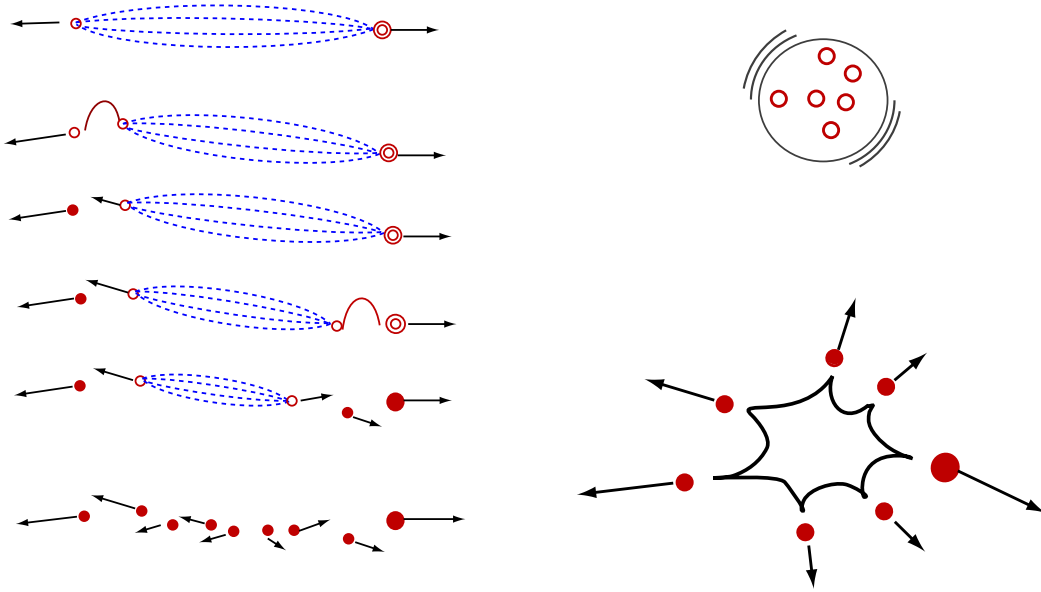


Figure 3.5: Left: Sketch of string fragmentation. Empty circles symbolize quarks, the full circles the final hadrons. The principal orientation of particles around the string axis (low p_{\perp}) is the key for the description of jets in hadron collisions. Right: Sketch of excited hadron and phase space decay. Particle emission from the fireball is isotropic in the cm. system of the excited hadron.

m_{T} is the transverse mass of the quark, where the quark mass is defined as the constituent mass. The parameters a_i and b are set to describe experimental data and are typically chosen differently for different quarks. The values for SIBYLL are shown in the appendix.

The distribution is chosen in this form to be symmetric between starting points. In the cm. system of two partons energy and momentum are assigned to the new hadron as fractions of the light-cone momenta $W_{\pm} = E \pm p_z$.

The flavors that appear in fragmentation would be suppressed by their masses so predominantly hadrons with u, d and s quarks are formed. The exact values of the flavor fractions are chosen to reproduce data (see Appendix). The formation of baryons is included by allowing diquark-antidiquark pairs.

The key feature of string fragmentation is that it is non isotropic. It produces particles in a very narrow region of phase space (low p_{\perp}) around the principle axis given by the initial partons.

3.3.2 Phase space decay

In diffractively excited hadrons, especially with low excitation masses (low Q^2), the hadron is not separated into partons that then form color strings and fragment. The coherent interaction rather distributes the energy equally among the partons in the hadron, forming something like a hot parton gas [51]. This gas would then eventually condense into hadrons, resembling de-excitation.

In SIBYLL this *hadronic fireball* is modeled by selecting a number of secondary particles that are to appear in the final state along with the original hadron. The number is chosen from a truncated Gaussian with an average of

$$n_{\text{thermal}} = 2\sqrt{\Delta E}, \quad (3.40)$$

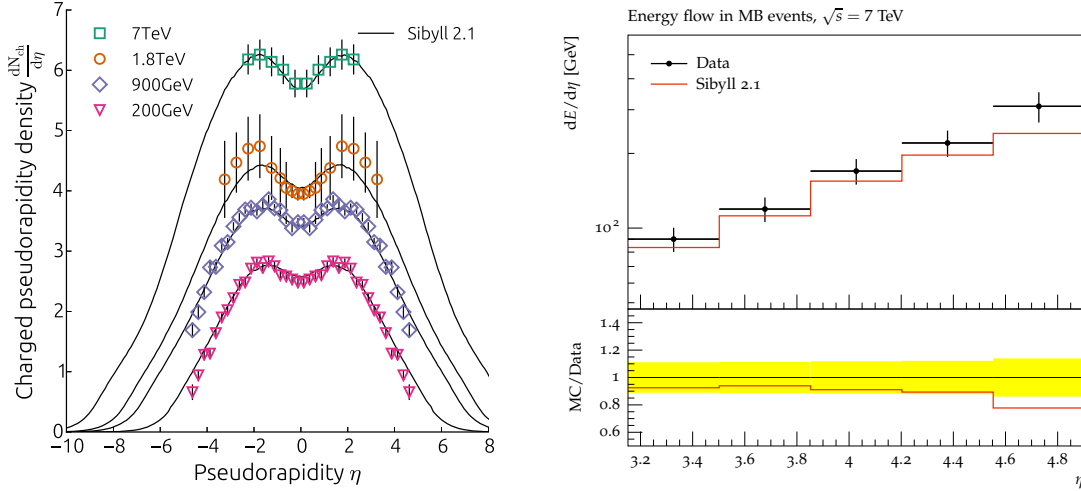


Figure 3.6: Left: Pseudorapidity distribution of charged particles measured by different experiments at different energies [52, 53, 54]. The model SIBYLL 2.1 gives a very good description of these data. Right: Energy flow in the pseudorapidity range $3.2 < \eta < 4.8$ measured with CMS [55].

where $\Delta E = M_X - m_{\text{beam}}$.

The particles that are added are taken to be charged and neutral pions only. The primary hadron may change its charge in the fireball which affects the charge of the first pion. The kinematics are determined by flat sampling in the $n + 1$ -body phase space, similar to n -body decay, hence *phase space decay*.

The key feature of phase space decay is that it is isotropic (flat sampling) (see Fig. 3.5). This means in particular that particles can have larger transverse momentum than in string fragmentation.

3.4 Performance & shortcomings of Sibyll 2.1

The current version of the model dates back to the year 2001 and hence was last tuned to data from TeVatron. The new measurements provided by the LHC test the predictions of the model at about five times the cm. energy that was available then.

The cross section that is predicted for 7 TeV with the model tuned to TeVatron data, turns out to be too high compared to the new cross section measurements at the LHC. In Sect. 4.1 it is discussed how the parameters in the amplitude can be adjusted to accommodate the new data.

In Fig. 3.6 the predicted distribution of particle production as a function of the pseudorapidity, is compared with measurements at different energies. Central particle production, the so-called *pseudorapidity plateau*, is sensitive to the number of parton interactions in the model. Correctly describing the evolution with energy strongly restricts the soft and hard amplitudes (Eq. 3.30). Based on the comparison of the measurement at 7 TeV and the prediction by the model, the evolution of the amplitude is well compatible with the data.

Unfortunately central production also depends on the hadronization parameters. An overestimation of the number of parton interactions could be compensated by the number of particles produced by the hadronization of each interaction. This kind of redundancy between parameters of different, *necessary* model components is the main difficulty in model tuning. It can only be overcome by comparing the model to as many different sets of data as possible.

In this particular case the spectacularly good description of the central particle production is accidental. There is an error in the definition of the p_{\perp} -cut applied to the minijets, which when corrected and after retuning, shifts the result down.

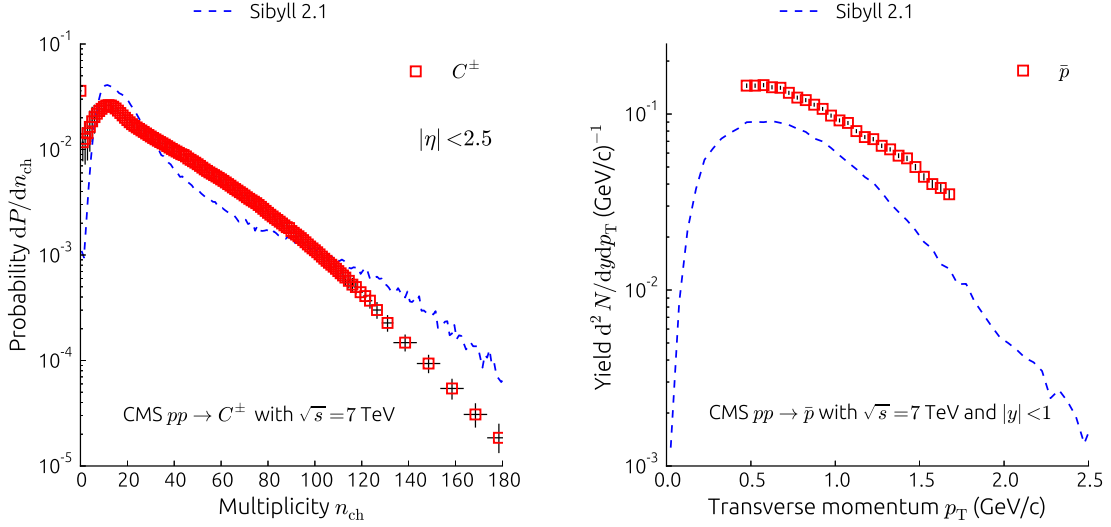


Figure 3.7: Left: Multiplicity of charged particles in the central pseudorapidity range $|\eta| < 2.5$ at $\sqrt{s} = 7$ TeV [56]. Right: Transverse momentum spectrum of antiprotons in pp collisions at $\sqrt{s} = 7$ TeV [57].

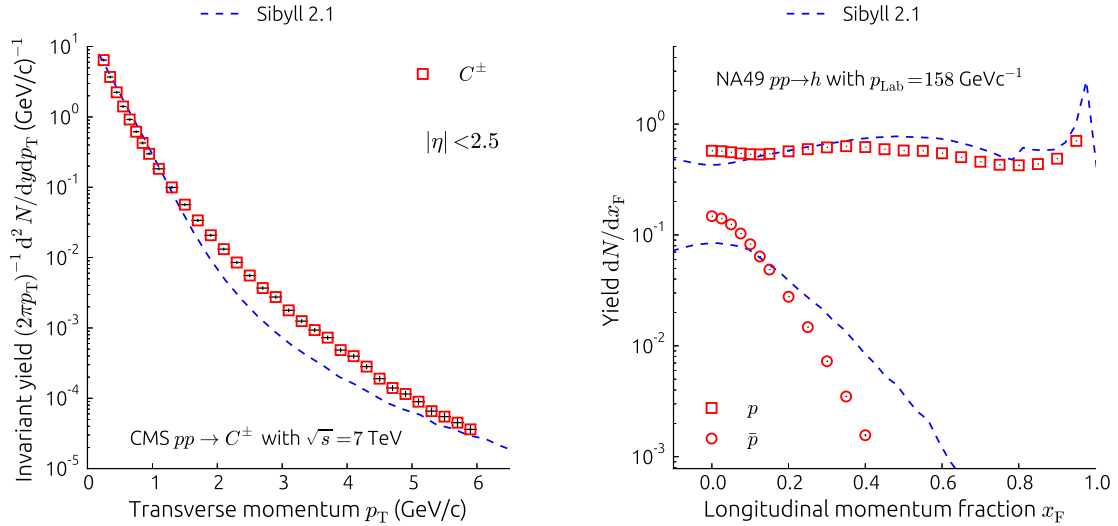


Figure 3.8: Transverse momentum spectrum of all charged particles at 7 TeV c.m. energy measured with the CMS detector [54]. Right: Inclusive distribution of protons and antiprotons in longitudinal phase space measured in the fixed target experiment NA49 [58].

In other observables, like the charged multiplicity distribution, the distribution of transverse momentum of charged particles or the transverse momentum spectra of individual particle species, the shortcomings of the model are more apparent.

The multiplicity distribution (Fig. 3.7) shows that the model overestimates the number of events with a very large number of parton interactions by a large amount. Since these make up only a very small fraction of all events, the effects can not be seen in other distributions and it certainly will not affect air shower calculations.

The same could be said for the discrepancies in the p_{\perp} -spectra, charged or identified. Nevertheless these things should be repaired, since the parameter changes or model extensions necessary for the repair can have effects elsewhere.

The p_{\perp} -spectrum of antiprotons (Fig. 3.7) shows two things, first that the total yield of antiprotons is too low and second that the shape of the distribution is wrong. The mismatch of the shape can be seen for all particles at essentially all energies, indicating that its origin lies

in hadronization. It will be addressed again in Sect. 7.3.1. Low baryon pair production will be discussed in Sect. 7.1.

The discrepancy seen in the charged p_{\perp} -spectrum in Fig. 3.8 is due to the effects of the aforementioned error in the p_{\perp} -cut in combination with the use of an outdated extrapolation for the PDFs to small x . The PDF update is discussed in the next section.

An observable that is well reproduced by the model is the energy flow shown in Fig. 3.6.

A fundamental shortcoming of the model in the form presented here is that it produces an artificial correlation between leading protons and central antiprotons that makes it impossible to describe both distributions at the same time (see Fig. 3.8). The problem can be avoided by introducing the beam remnants as is shown in Sect. 5.

Finally there is an inconsistency in the model in the way the treatment of diffraction in the case of hadron-proton collisions is extended to the case of hadron-nucleus collisions. This will be addressed in Sect. 8.

Further there is a technical error in the model for nuclear diffraction that leads to the additional production of positive charged kaons. This error is the reason for the large overestimation of the charge ratio of muons in the atmosphere [59].

3.5 Nucleus-nucleus interactions

The final ingredient needed for an interaction model used in air shower simulations is a model for nucleus-nucleus interactions.

In principle the Glauber model in Eq. 3.31 can be extended to nucleus collisions simply by adding another product for the nucleons in the beam nucleus (and adding another set of nuclear wave functions in the appropriate place, see Sect. 8).

The model used in SIBYLL instead is the semi superposition model [60]. An air shower is a cascade of interactions that completely disintegrates the primary nucleus. In the superposition model an air shower initiated by a nucleus with mass number A is approximated by adding A nucleon initiated air showers with the primary energy $E_N = E_A/A$ together. The semi-superposition model refines this approach by distributing the starting point in the atmosphere and the energy of the sub showers, representing the fragmentation of the primary nucleus along the trajectory. The advantage in comparison to the basic superposition model is that the step wise fragmentation introduces additional fluctuations in the development of air showers initiated by nuclei.

More details can be found in the reference given above.

Chapter 4

Cross section and parton density update

4.1 Cross section update

This section describes the changes in the model that were introduced to get a better description of the cross sections at LHC energies. They were previously described in the 2014 ISVHECRI conference proceedings [61].

Measurements at LHC suggest (see Fig. 4.1) that SIBYLL 2.1 overestimates the cross section at high energies. The inelastic cross section measured in the TOTEM experiment, which has the highest precision for a measurement of the total cross section at LHC, is $73.5^{+1.9}_{-1.4}$ mb [62] whereas SIBYLL predicts 80 mb. The rise of the p-p cross section beyond 1 TeV is mainly driven by hard parton scattering (hard minijets).

In SIBYLL the eikonal approximation is used to combine the parameterizations of soft scatterings with the perturbative calculation of the minijets into an unitary amplitude, which then defines the total and elastic cross sections. The size of the soft and hard contributions in this formalism depends on the size of the particular cross section and the profile function (see Eq. 3.7 in Sect. 3.1).

In order to make the inelastic cross section compatible with the new measurements without changing the hard cross section (calculated within QCD), the profile function of the distribution of the hard partons in transverse (impact parameter) space has been made narrower, so that peripheral collisions are less likely to produce minijets (Fig. 4.3).

The downside of this approach is that central collisions now exhibit very high densities of partons (profile functions are normalized), which consequently means that some events will be sampled with a very large number of parton interactions. The number of interactions directly translates to the number of final state particles so the narrow profile function will produce a larger tail in the multiplicity distribution (see Fig. 3.7). However central collisions are rare so the average multiplicity and most other observables are still compatible with the measurements.

Since our goal is a model capable of describing interactions a decade and more higher in center-of-mass energy, the effects of high parton densities have to be taken serious, even if the mean multiplicity still agrees with current experiments.

A microscopic model of parton density *saturation* could limit the number of scatterings in central collisions and thereby correct the multiplicity tail. In the current model, saturation is implemented only in an impact parameter independent way as an energy-dependent lower p_{\perp} -cutoff for the minijets (details in Sect. 3.1 and the discussion in Sect. 9).

Another indication for the limitations of the model can be seen in Fig. 4.4. Here the elastic slope parameter B_{ela} is shown as a function of the cm. energy. While the model is well capable of describing low energy measurements it has problems with TeVatron data at 1.8 TeV and clearly fails at 7 TeV. However there is an ambiguity in the definition of the slope parameter, so the results have to be interpreted with care. The slope parameter in experiments is determined

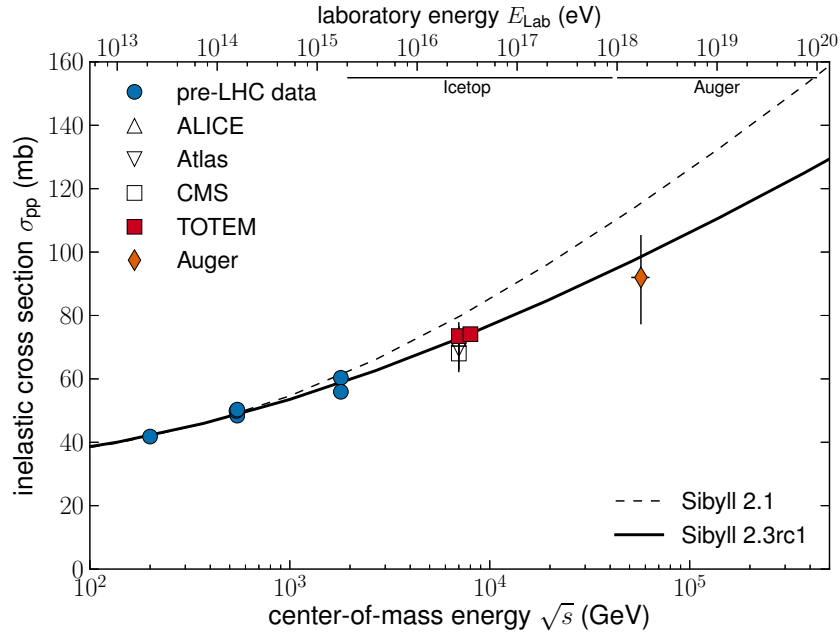


Figure 4.1: Inelastic pp cross section in SIBYLL. The updated cross section is shown in blue, the old version is in black. The red squares are the measurements by TOTEM [62]. The highest energy measurement was done at the Pierre Auger Observatory [63, 64], using cosmic ray air showers. The top axis shows the equivalent laboratory energy for pp interactions. The energy ranges where the IceTop air shower array [65] and the Pierre Auger Observatory [64] measure cosmic rays are indicated.

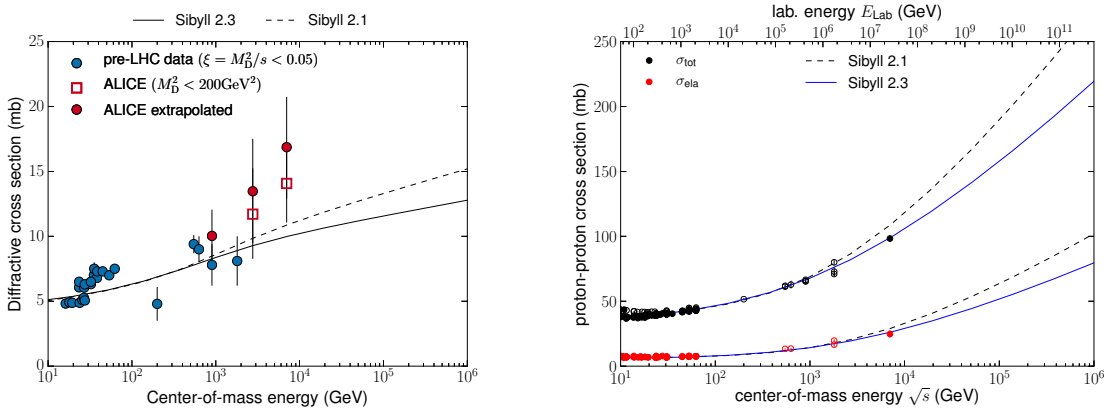


Figure 4.2: Left: Cross section for diffractive dissociation in proton proton collisions. The estimation of the cross section decreases between models. Right: Total and elastic cross section for proton proton collisions. The measurement at $\sqrt{s} = 7$ TeV is from TOTEM [62]

assuming an exponential shape for the differential elastic cross section and then fitting it to the data

$$\frac{d\sigma}{dt} \sim e^{-B_{\text{ela}}t} . \quad (4.1)$$

New measurements at 8 TeV [67], however, have shown that the shape of the cross section deviates from a pure exponential and that it is best described by an exponential with additional terms

$$\frac{d\sigma}{dt} \sim e^{-(B_{\text{ela}}t + Ct^2 + Dt^3)} . \quad (4.2)$$

A comparison of the pure exponential differential cross section in experiment and the model is shown in Fig. 4.3 on the right. The full t dependency of the cross section that is given by the

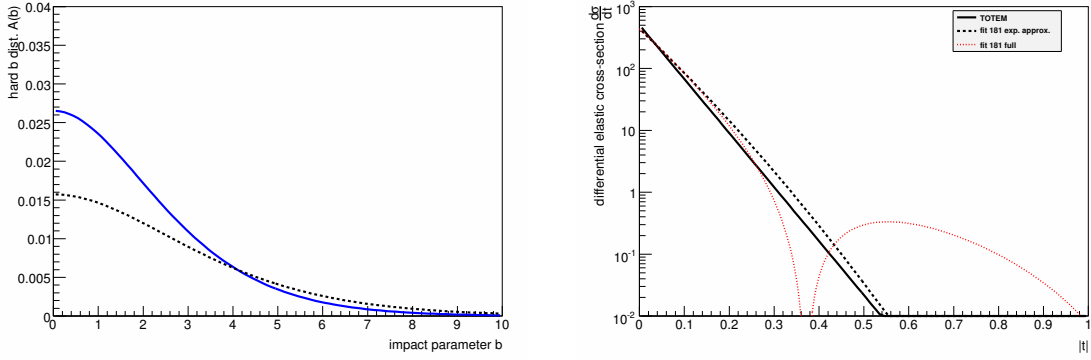


Figure 4.3: Left: Profile function of hard interactions in SIBYLL 2.1 (dashed) and in the model with adjusted cross section (solid blue). Right: Differential elastic scattering cross section $d\sigma/dt$. The solid black line corresponds to an exponential with the slope parameter measured in TOTEM [66]. The dashed black line is an exponential with the slope parameter in SIBYLL. New data show that the shape is non exponential [67]. The full differential cross section in SIBYLL is shown by the red dashed line.

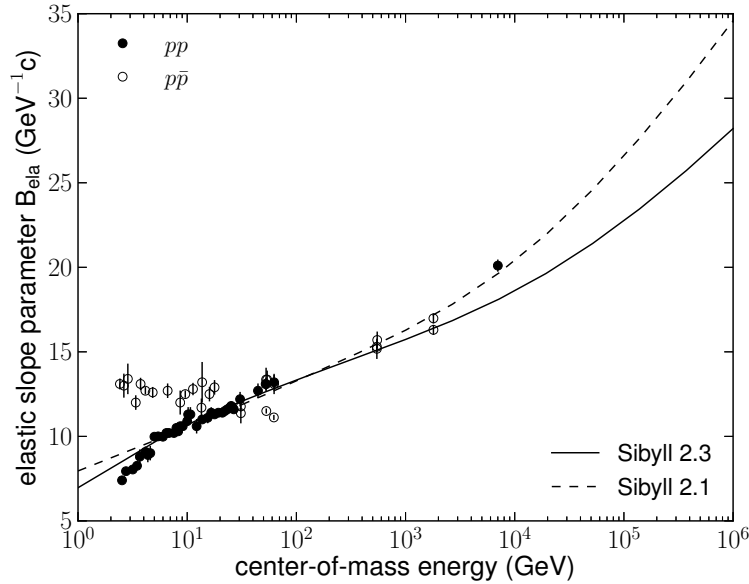


Figure 4.4: Slope of the elastic peak in proton-proton collisions in the model compared to measurements.

absolute square $|f|^2$ of the Fourier transform of the amplitude $\Gamma(s, \vec{b})$ defined in Sect. 3.1, is also shown.

In addition to changing the hard profile function the coupling parameters of the soft cross section (X, Y in Eq. 3.11) were adjusted to fit the p - p and \bar{p} - p cross section data at lower energy.

Since the proton profile also enters the meson-nucleon cross sections, the parameterizations of the soft contribution were fitted there again as well.

The resulting cross section is shown in Fig. 4.1 as a blue line. The old cross section for comparison is shown as a black solid line. The data point of the highest energy is the estimation of the p - p cross section from air shower measurements at the Auger Observatory at energies of about $\sqrt{s} = 57$ TeV [63, 64].

This value has not been used to fit the cross section in SIBYLL and can be seen as an indication that the extrapolation by the model is working well.

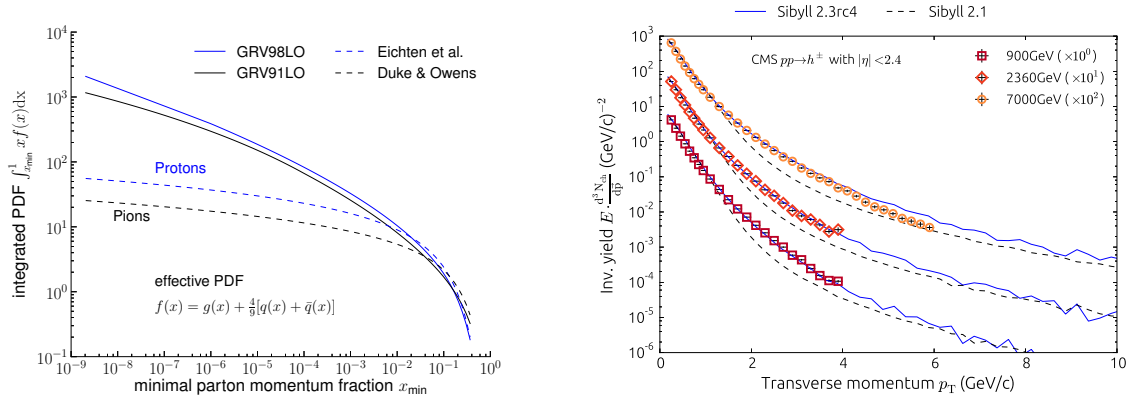


Figure 4.5: Left: Integrated effective parton distribution functions for pions (black) and protons (blue). The individual quark and gluon distributions from the sets are combined to an effective PDF. In the previous version the set by Duke & Owens[68] was used for the protons (all baryons) and the one by Eichten et al. [48] for the pions (all mesons). In SIBYLL 2.3 both parameterizations for protons and pions are taken from Glück, Reya and Vogt [34, 69]. Right: Inclusive cross section for charged particles as function of the transverse momentum. The results obtained with the old and new versions of SIBYLL are compared with CMS data at different c.m. energies [70, 54].

4.2 New parameterizations of the parton distribution functions

The momentum fractions that determine the kinematics of the minijets are taken from an effective parton density function [47]

$$f(x) = g(x) + \frac{4}{9} [q(x) + \bar{q}(x)] , \quad (4.3)$$

where $g(x)$ and $q(x)$ are the distributions of the gluons and quarks. For the case of a proton (baryon) projectile the parameterization is chosen according to Eichten et al. (EHLQ) [48], for pion (meson) projectiles the parameterization by Duke & Owen [68] is chosen. For $q(x)$ sea contributions from three light flavors (u, d, and s) are included as well as the contribution from the valence quarks.

In the updated version the effective parton distribution function (PDF) is used but the quark and gluon contributions are sampled from the parameterizations by Glück, Reya and Vogt (GRV) [34, 69]). The same parameterization that is already used in the calculation of the hard minijet cross section (Sect. 3.1).

The main difference between these parameterizations is the behavior at low x which, in the case of the GRV parameterization, is much steeper.

In Fig. 4.5 the distribution of transverse momenta of charged hadrons measured by the CMS detector [70, 54] is shown. In combination with the correction of a mistake in the definition of the cut between soft and hard interactions (p_{\perp}^{\min}) the steeper PDFs give a better description of the p_{\perp} -spectra in the range of intermediate transverse momenta (2-5 GeV/c) than in SIBYLL 2.1, see Fig. 4.5. At very high transverse momenta in case of the 7 TeV data, the over abundance of hard scattering (see Fig. 3.7) in SIBYLL results in an overestimation of the p_{\perp} -spectrum.

Chapter 5

New remnant treatment

As discussed in Sect. 2, the development of air showers is most sensitive to the forward phase space in hadronic interactions. From deep inelastic scattering experiments it is known that the valence quarks, the quarks related to the quantum numbers of the initial particle, on average carry a large fraction of the particles momentum. The forward phase space is therefore mostly influenced by the fragmentation of the valence quarks, which is why it is also called beam fragmentation or just fragmentation region. The central region, in contrast, is unrelated to the initial state since it is predominantly formed by the scattering of sea quarks and gluons and these are more or less universal for all hadrons.

The difference is obvious when looking at inclusive distributions of individual particle species in longitudinal phase space (typically Feynman- x , see Sect. 2.2.3). Particles that share one of the valence quarks with the beam particle, have a harder spectrum, i.e. they are produced with larger longitudinal momenta than particles that are produced from sea quarks in the initial particle.

The comparison of the inclusive distributions of pions, kaons and protons in p-p collisions in Fig. 5.1 shows this very clearly. The measurement in the figure was done at the fixed target experiment NA49 [58] with a beam of momentum 158 GeV, corresponding to a c.m. energy of only 17 GeV.

At this low energy particle production is entirely dominated by soft processes. The fact that the proton spectrum is flat even at large values of Feynman- x is also known as the *leading particle effect* and it is the consequence of the valence quarks carrying larger momentum fractions.

5.1 Leading particle effect in Sibyll 2.1

The dominant string configuration for SIBYLL 2.1 in non-diffractive events at low energy is given by two strings connecting the valence quarks of the projectiles (see (a) in Fig. 5.1). Multiple interactions and minijets only start to play a role at a few hundred GeV.

In order to reproduce forward baryon spectra, the fragmentation function for the leading baryon (qq) is chosen to be harder. Leading baryons share at least two flavors with the initial proton so they can be neutrons, Δ -resonances or Λ and Σ hyperons, neglecting higher resonances. Measurements of the x_F -spectra of these particles show different shapes for the forward distributions [27], requiring a different leading fragmentation function for each particle (see Fig. 5.3). The flat proton spectrum in Fig. 5.2 for example requires a very hard fragmentation function of $f_{\text{leading}}^p(z) \sim z$.

Apart from this lack of generality in the fragmentation function the *valence string* ansatz has the problem that it introduces a strong correlation between the leading baryons and central baryon production. In principle there should be some correlation because baryons are very heavy and always have to be produced in pairs. At low c.m. energies as these, it is difficult to localize enough energy in a string so that additional baryons can be formed.

With a flat proton spectrum and corresponding fragmentation function the additional baryon is very likely produced whenever the leading proton is slow. This then produces a too hard spectrum for the antibaryons (see \bar{p} in Fig. 5.2).

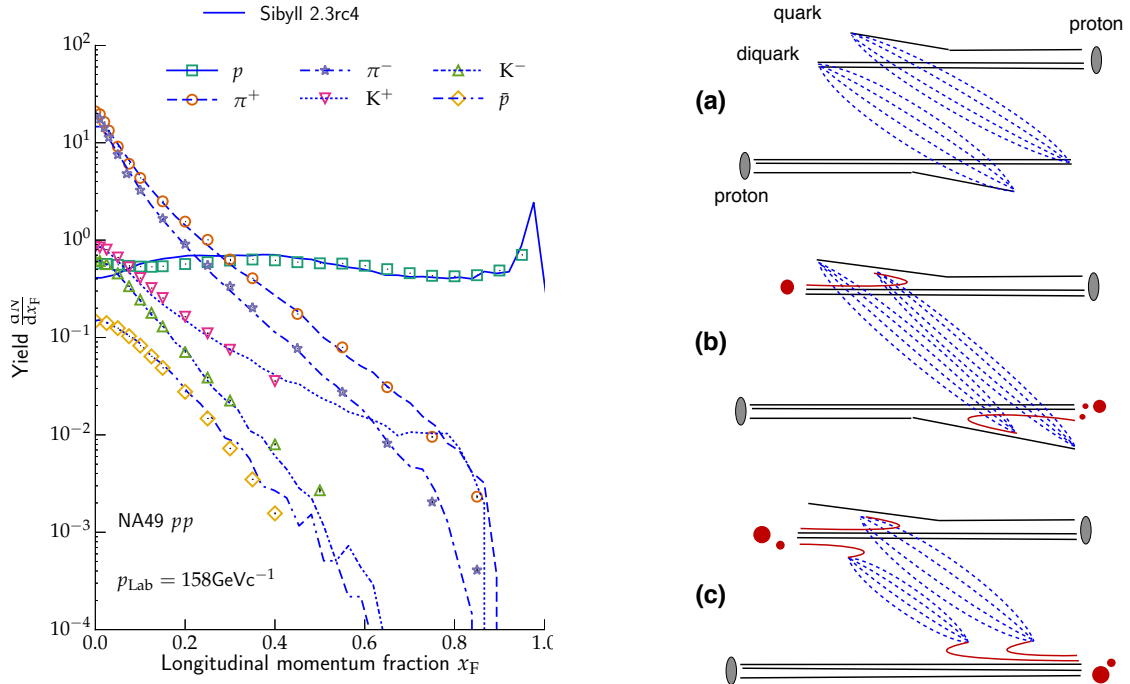


Figure 5.1: Left: Longitudinal momentum spectrum of particles measured in the fixed target experiment NA49 with beam momentum of 158 GeV [58]. The lines are the new version of the model SIBYLL 2.3. Note the difference between the spectra of the different charge states (π^\pm and K^\pm), reflecting that π^+ ($u\bar{d}$) is more likely to be formed from a proton (uud) than π^- ($d\bar{u}$). Right: String configurations for the first interaction in SIBYLL. Without remnant (a) the valence quarks are attached to the first strings. In the simplest extension including a remnant (b) the strings are attached to a sea quark pair, where the quark may be exchanged with the valence quark (figure). In the general case (c) any number of sea quark pairs can be created, two are attached to the first strings the rest will contribute to the remnant.

If the slow protons are removed, for example by choosing a Lund type function (exp. suppression for $z \rightarrow 0$, setting $a = 0$ removes the unwanted suppression for $z \rightarrow 1$) as the leading fragmentation function (see SIBYLL 2.3-rc1 in Fig. 5.2), then the antibaryons are produced with the correct spectrum but the proton spectrum is not flat anymore.

The correlation can be broken by going from the valence string model to a model with central strings and so-called *beam remnants* (Fig. 5.1-right (b,c)).

In addition to repairing the baryon spectra the remnant model can also be used to improve the forward production of pions. In particular the charge ratio of pions in the forward direction that is shown in Fig. 5.2 is not described very well. This ratio is ultimately reflected in the charge ratio of muons in the atmosphere [71].

Furthermore it was shown in the context of other models [72] that the additional degrees of freedom offered by the introduction of beam remnants are necessary to describe the large x_F region of phase space.

It was shown that the localization of the beam quantum numbers, in particular isospin, into a small fragmenting system has a positive influence on the muon content of extensive air showers [19].

To summarize the models used, the model with the valence quarks between hadrons directly connected by strings and using a hard, fine tuned fragmentation function is SIBYLL 2.1. SIBYLL 2.3-rc1 is a development version which still uses the valence string approach but applies a more general fragmentation function at the string end [61]. The remnant model is implemented in SIBYLL 2.3-rc4 and it is described in the following section. rc4 is the current candidate for release, so it is also just called SIBYLL 2.3.

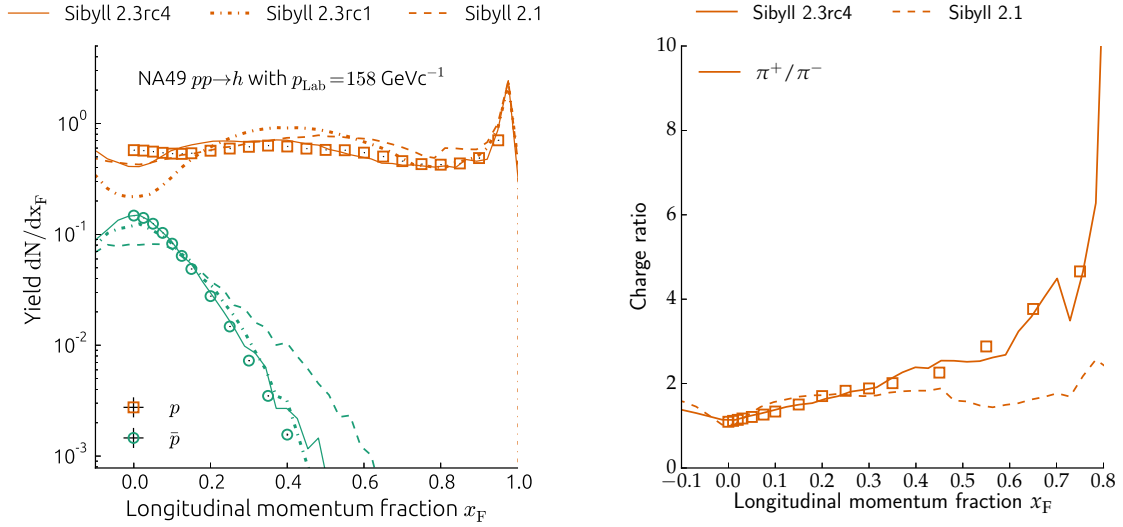


Figure 5.2: Left: Longitudinal momentum spectra of protons and antiprotons measured in the fixed target experiment NA49 [58]. SIBYLL 2.1 (dashed) can not describe both spectra at the same time. The intermediate model SIBYLL 2.3-rc1 (dash dotted) describes antiprotons well but fails for the slow protons ($x_F < 0.4$). The remnant model (solid) still has a few central protons missing, but the overall shape of both p and \bar{p} are much better. Right: Charge ratio of pions in p-p collisions [73]. SIBYLL 2.1 produces essentially a constant ratio of $\pi^+ : \pi^-$, whereas the data show an increase in the fragmentation region. This behavior is expected from the quark content of the proton (uud) which offers more combinations to produce $\pi^+(u\bar{d})$.

5.2 Remnant model

When implementing the remnant model in SIBYLL three questions have to be answered: How does a remnant fit in with the soft & hard interaction picture (DPM)? Where does the mass come from and what is the mass distribution? How does the remnant fragment?

5.2.1 Remnant formation

A beam remnant in the parton picture can be formed whenever there are partons left in the hadron that are not involved in a parton interaction, so-called *spectators*. In SIBYLL 2.1 these are always included in the first soft interaction, hence valence strings.

In the new remnant model the spectators are separated again from the soft interaction. It is assumed that there is only one set of spectators (color triplet and anti-triplet pair). The first soft interaction is to occur between an additional pair of sea quarks (u, d, s, c) and the valence quarks are made to make up the remnant (see sketch (b) in Fig. 5.1-right).

Occasionally the color triplet (q_{val}) in the remnant may be exchanged with the color triplet in the sea quark pair, so that the remnant can receive a new flavor. This channel is necessary to reproduce the harder spectra observed for particles that are related to the proton (e.g. hyperons: Λ^0, Σ) compared to spectra of particles that are not (see also difference between π^\pm and K^\pm in Fig. 5.1). The anti-triplet (qq_{val}) is excluded from this exchange since the conversion of the leading baryon into a meson is not very common. For meson projectiles both valence quarks are allowed to be exchanged. The flavor exchange rate is set to $P_{\text{exchange}} = 0.6$.

The momentum fraction assigned to the sea quarks is sampled from the same $1/x$ distribution as for the soft minijets with an additional mass regulation at $m_{\text{sea}} = 1 \text{ GeV}$, i.e. $x_{\text{min}} = 2m_{\text{sea}}/\sqrt{s}$. The momentum fraction of the remnant as a whole ($q_{\text{val}} + qq_{\text{val}}$) is sampled from a hard distribution of the form $x^{1.5}$.

In general the remnant is defined to be always present. With the changing parton structure, in particular the increasing number of interactions at high energy, a *survival probability* P_r is

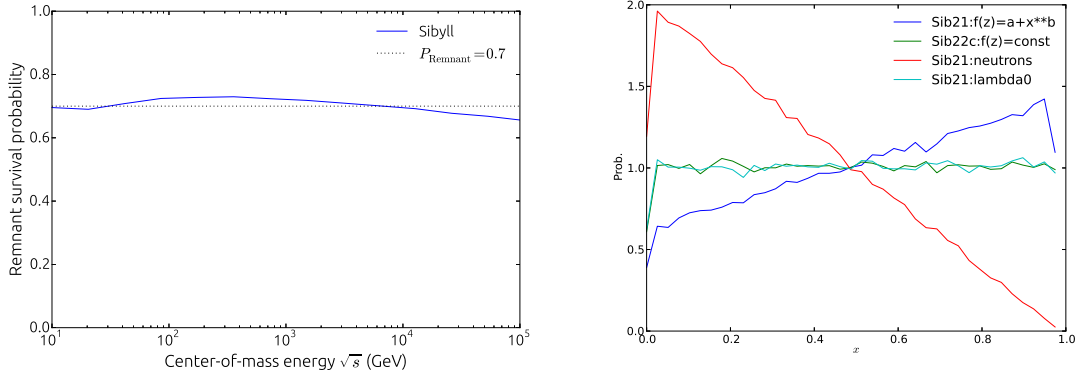


Figure 5.3: Left: Remnant survival probability as a function of energy. The energy dependence comes from the idea that more interactions increase the chance that the valence quarks are among the interacting particles. Right: Fragmentation function used for baryons produced from valence diquarks in SIBYLL 2.1.

defined that represents the likelihood that there are spectators left to form a remnant after parton scattering. Each hard or soft interaction reduces the chance that the remnant will survive. The same should occur for interactions with multiple nucleons in case of a nuclear target. The remnant survival probability is then calculated as

$$P_r = P_{r,0}^{N_w + \alpha \cdot (n_{\text{hard}} + n_{\text{soft}} - 1)}, \quad (5.1)$$

where N_w represents the number of interacting nucleons and n_{hard} and n_{soft} are the number of soft and hard parton interactions in an event. The coupling α is set to 0.01 and the basic survival probability is $P_{r,0} = 0.6$. The resulting energy dependence of remnant formation is shown in Fig. 5.3.

The interaction dependence of remnant formation and the values of the parameters are chosen in order to describe the pion and proton spectra measured by NA49 in pp and pC interactions. In Fig. 5.4 the results are compared to the old model with a hard fragmentation function. The additional interactions in case of the carbon target result in a lower probability for remnant survival according to Eq. 5.1. In case of no remnant the valence quarks are attached to the first pair of strings as in the old model (Fig. 5.1-right a), however without using the hard fragmentation function. This effectively means the leading protons lose energy (see relative decrease around $x_F \sim 0.8$ between pp and pC in Fig. 5.4) while mesons carrying quarks from the proton (π^+ , K^+ , first in hadron chain) gain energy relative to the proton. Since the strings in case of two nucleon interactions have in total less energy available, the meson spectra come out the same as in pp.

5.2.2 Mass excitation

Partons in SIBYLL are treated massless so the mass for the remnant is transferred to the quarks assigned to the remnant through an interaction with the valence quarks of the other hadron. The interaction itself is taken to be the same as in diffraction dissociation (see Sect. 3.2) with slightly different parameters.

The flat distribution of protons in x_F (Fig. 5.2) determines the shape of the mass spectrum of the remnant excitation for pp collisions.

$$\frac{dP}{dM_r^2} = \left(\frac{1}{M_r^2} \right)^{\alpha_r}, \quad (5.2)$$

with $\alpha_r = 1.5$.

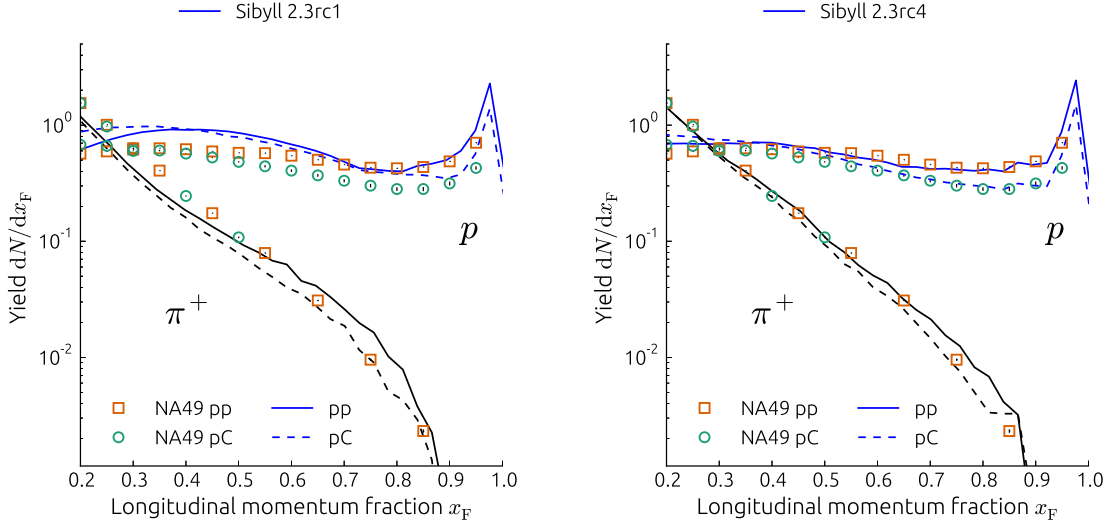


Figure 5.4: Proton and pion spectra in x_F compared between pp and pC collisions in SIBYLL 2.3-rc1 (left) and SIBYLL 2.3 (right). Note that the leading proton is attenuated in going from pp to pC, while the pion distribution remains almost the same. This behavior is well reproduced by the remnant model (right), whereas the model with valence strings fails (left).

The lower limit of the mass spectrum is given by the beam mass, the upper limit is of the same form as the coherence limit in diffraction

$$M_{\max}^2 = \tilde{\zeta}_{\max} \cdot s, \quad (5.3)$$

but with $\tilde{\zeta}_{\max} = 0.02$.

In principle the exponent α_r of the mass spectrum could vary between different beam particles. This could be an option to improve the description of meson resonance spectra (ρ, K^*) in pion and kaon interactions, which show a strong leading component (see discussion in Sect. 7.2). In order to keep the model as general as possible the parameter is kept universal so far.

5.2.3 Remnant de-excitation

After the remnant is formed there are several mechanisms for it to hadronize. In the most simple case the valence quarks recombine to form the initial hadron. This mode is used in the model for the lowest excitation masses, when the difference to the initial hadron mass

$$\Delta E = M_r - m_{\text{beam}} \quad (5.4)$$

is below $E_{\min}^{\text{recomb}} = 0.2 \text{ GeV}$. According to the kinematics of diffraction ($A + B \rightarrow A + X$), which is an equivalent to the situation in this remnant model, low masses correspond to large momenta $x_F \sim (1 - M_x^2/s)$. The low mass excitations therefore exactly determine the large x_F behavior of the proton spectra.

In principle the remaining masses could just be fragmented the same way diffractive systems are treated, i.e. masses in the region $E_{\min}^{\text{recomb}} < \Delta E < E_{\min}^{\text{string}}$ undergo phase space decay and higher masses ($\Delta E > E_{\min}^{\text{string}}$) hadronize in a string. The problems with describing the charge ratio of pions and kaons in NA49 inspired an additional de-excitation mode, namely resonance decay.

It is essentially a variant of phase space decay with a preset final state. Instead of recombining to the initial beam hadron, the quarks in the remnant form an intermediate state, typically a short-lived resonance of the initial hadron. For simplicity the two lightest resonances with the same quantum numbers as the beam hadron are chosen. In case of proton and neutron this would be the nucleon resonances N(1440) and N(1710). It is clear that the final state of the

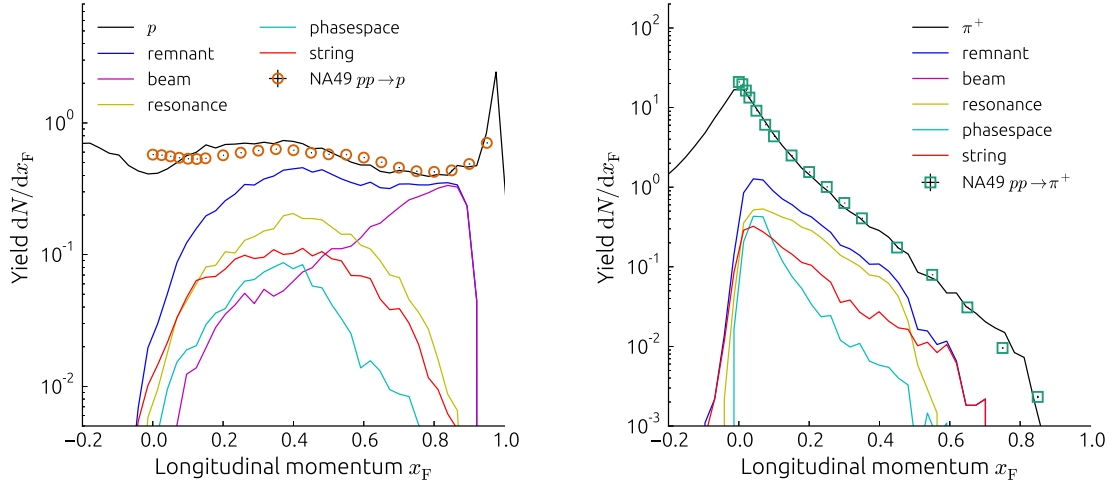


Figure 5.5: Break down of remnant components for protons (left) and pions (right) in NA49. The shape of the ‘beam’ component for protons is determined by the remnant mass spectrum. The maximal x_F for the remnant protons is determined by the minimal mass of the sea quark pairs m_{\min} .

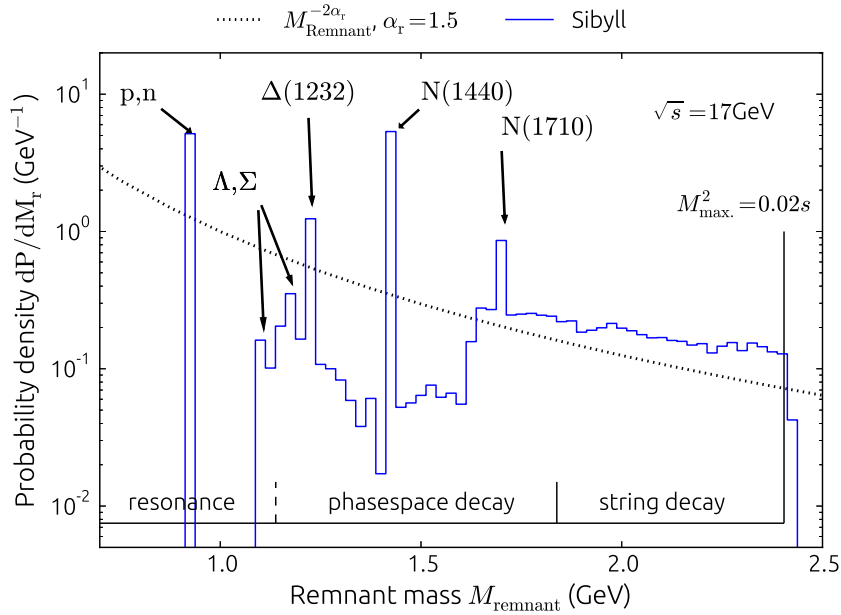


Figure 5.6: Mass spectrum of the remnant excitation for proton-proton collisions at $\sqrt{s} = 17\text{GeV}$. The ranges of the different de-excitation modes are shown at the bottom. The dominant lines are the nucleons and their first resonances N(1440) and N(1710). When allowing one of the quarks in the remnant to be exchanged with a sea quark, Delta- and Hyperon-resonances can be formed as well. The mass spectrum in general is chosen as $M^{-2\alpha_r}$, with $\alpha_r = 1.5$ and limited to masses within $M_{\max}^2/s = 0.02$.

resonance decay is the same obtained from the phase space decay of an excited proton with one additional pion

$$\begin{aligned} p^* &\rightarrow p + \pi^0 \\ p^* &\rightarrow n + \pi^+ . \end{aligned}$$

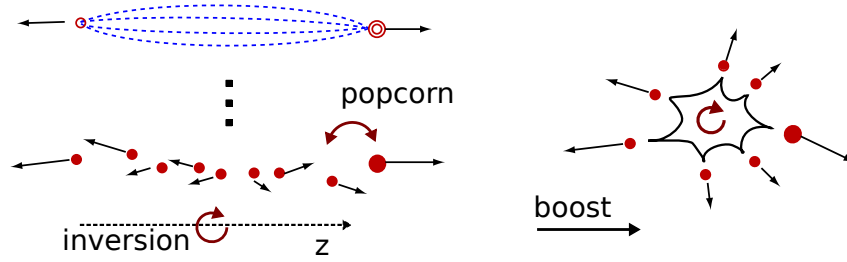


Figure 5.7: Sketch of longitudinal string compared to phase space decay final state. The popcorn mechanism switches diq and q in the hadron chain. String inversion turns the entire hadron chain around, i.e. the diq carries a very low fraction of the hadron momentum. In phase space decay the final state is isotropic in the cm. of the decaying system.

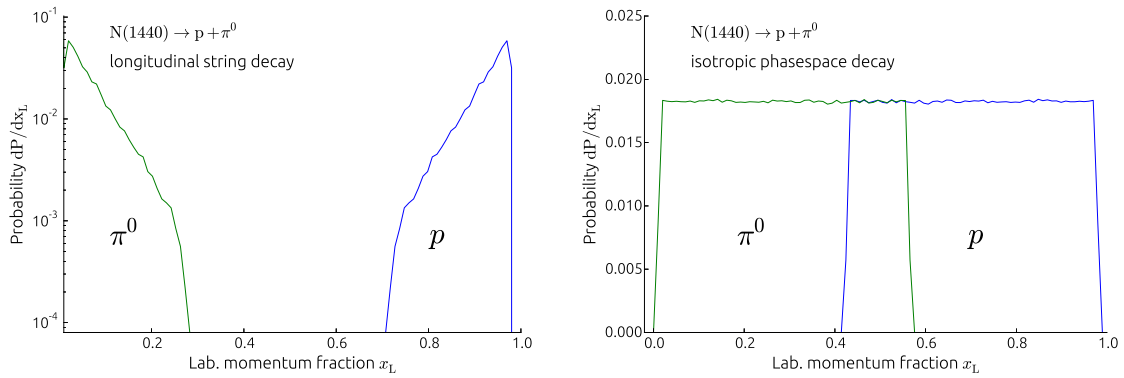


Figure 5.8: Comparison between the spectra of the different modes for the decay of the nucleon resonance $N^+(1440)$. Left: decay through a longitudinal string. Right: isotropic phase space decay. The final state in in both cases is a proton and a neutral pion. In phase space decay, however, there is a chance that the leading particle after the decay is the pion, while in string decay the leading particle is always the proton. This difference was one of the reasons to include both modes for the decay of the remnants.

Table 5.1: Table of the isospin decomposition (Clebsch-Gordan coefficients) of Δ and N baryons into pions and nucleons. Note that for N -resonances the final state where the nucleon has a different charge is preferred.

		Δ^{++}				
π^+	p	1	Δ^+	N^+		
	π^+	n	1/3	2/3		
	π^0	p	2/3	-1/3	Δ^0	
		π^0	n	2/3	1/3	
		π^-	p	1/3	-2/3	Δ^-
			π^-	n	1	

The difference is that for the resonance the branching ratio between the two charge states is not symmetric. The isospin decomposition of the $N(1440)$ resonance for example favors the $\pi^+ n$ final state over $\pi^0 p$ with a ratio 2:1 (see Tab. 5.1 for other decompositions). In addition the phase space decay would also allow final states with a nucleon and two pions.

Table 5.2: Table of the mass regions for the different de-excitation modes of the remnant. A region is defined as: $M_i < \Delta M = M_r - m_{\text{beam}} < M_{i+1}$. Thresholds M_i are given in GeV.

beam recomb.	resonance	phase space	string
0.2	0.4	0.7	1.0

A comparison between the kinematic of a 2-body decay via phase space decay and string fragmentation is shown in Fig. 5.8. The strict longitudinal orientation of the string means that the meson is always emitted backward with respect of the fragmenting remnant. So in combination with the decay spectrum, which occasionally allows the meson to carry more energy than the baryon (isotropic, see Fig. 5.8), the 2:1 ratio of the resonance decay channels could be used to increase the pion charge ratio at large x_F .

Other options could involve the modification of string fragmentation. In *string inversion* the diquark qq_{val} is placed at the $-z$ end of a string representing the fragmentation of an excited system along $+z$ (see Fig. 5.7-left). In the case of the increased *popcorn mechanism*, a meson can switch place with a baryon in the hadron chain. At the string end the meson then replaces the baryon as leading particle (see also Fig. 5.8-left). In strings with a two particle final state the two are obviously equivalent, in larger strings the baryon carries much less energy in string inversion.

Compared to the string modifications the resonance decay model is the least artificial choice to reproduce the leading charge ratios, in particular, because of the emergent distinction between different beam hadrons.

The implementation of the resonance decay mode is such, that the resonance channel is selected after the mass was sampled from the $M^{-2\alpha}$ -distribution. The probability for selection is determined from a relativistic Breit-Wigner function centered around the mass of the resonance. The width of the Breit-Wigner function is taken to be the width of the resonance times a scaling factor. The factor is adjusted to reproduce the measured spectra. After the resonance is selected, the mass is set to the pole mass to avoid problems with phase space in the final state. If the resonance is not selected then the other hadronization modes are called.

A breakdown of the contributions from the different de-excitation modes to the proton and pion spectrum in NA49 is shown in Fig. 5.5. The thresholds of the channels are listed in Tab. 5.2 and a full list of the resonances implemented in the is shown in the appendix.

The resulting mass spectrum for protons is shown in Fig. 5.6. The different resonance peaks are clearly visible above the continuum. Σ, Λ and Δ resonances can be created when the valence quark is exchanged with one of the sea quarks. The break in the spectrum in the region labeled phase space decay is due to the wrong implementation of the boundary between the resonance and phase space region, which is meant to be semipermeable. That way resonances may be formed in the phase space decay region, so that the discrete spectrum, starting with the beam particle transitions into the continuum with discrete peaks.

After adjusting the parameters of the new remnant model, including the parameters of the sea quark distribution, and retuning some of the fragmentation parameters, the model is capable of describing the complete set of spectra from NA49, including protons, antiprotons, pions and kaons for both pp and pC interactions reasonably good. In particular the charge ratio as a function of x_F is now much better represented (see Fig. 5.2-right).

The correlation between leading protons and central antibaryons has been broken as can be seen in Fig. 5.2 on the left.

So far the model was exclusively tuned to proton projectiles. The behavior of the remnant in pion or kaon interactions is only extrapolated. In combination with the enhanced production of leading resonances observed in experiment for meson-proton and meson-nucleus interactions (see Sect. 7.2 for current model) the model could need some refinements.

Chapter 6

Extension to charm production

The interaction model SIBYLL 2.1 is limited to the production of particles containing u, d, and s quarks. In an earlier work by Ahn et al. [74]¹ it was shown that a simple phenomenological extension of the fragmentation model, based on the family connection between strange and charmed hadrons, can account for the production of charmed particles at low energy. In this approach the normalization is set by the rate at which charm quarks appear relative to strange quarks and it is globally defined to be $P_c = 0.004$.

With the measurements of charm production at higher energies by the LHC experiments this model proved to be too limited. In this section the extension of the basic charm model [74] to include the rapid rise of a hard central charm component that is observed at the LHC is described. Compared to the rest of the model, charm production can be treated as independent, because the production cross section for charm is two orders of magnitude smaller than general particle production. Because of the relatively large mass of the charmed hadrons compared to pions, kaons and even protons, the dependency in the opposite direction is very strong. Changing general fragmentation parameters will also affect charm production.

6.1 Charm model

The mentioned high mass of the charm quark, means the production of charmed hadrons in the fragmentation process is suppressed by a large factor. The dominant mechanism is the direct production of charm quarks in parton-parton scattering ($gg \rightarrow c\bar{c}$ or $q\bar{q} \rightarrow c\bar{c}$). In QCD the leading contribution is from gg scattering, so the process is sometimes referred to as *QCD gluon fusion* [75]. The minimal momentum transfer for which the process can occur is given by the charm quark mass $Q^2 > Q_{\min}^2 \sim 4m_c^2$. The high value of the charm quark mass of $m_c = 1.275 \text{ GeV}$ [16] means that the process can be expected to be calculable within perturbation theory.

The event generator SIBYLL includes only the dominant terms of hard parton-parton scattering at high energy and does not distinguish between the hadronization of the different parton configurations (see Sect.3). All parton-parton scattering processes fragment into hadrons through an unflavored two string configuration, similar to two scattered gluons (usually referred to as hard minijets).

To account for the dominating hard scattering contribution the charm quark fraction is increased in the fragmentation of the hard minijets. In order to keep the threshold behavior at low energy the charm quark fraction is suppressed exponentially in low mass strings. Specifically

$$P_{c/s}^i = P_{c,0}^i \exp\left(-\frac{m_{\text{eff}}}{\sqrt{\hat{s}}}\right), \quad (6.1)$$

where \hat{s} is the invariant mass of the scattering partons and m_{eff} is the effective mass scale. To account for string configurations of higher order, charm production is not limited to the end

¹version 2.2c, results presented at ISVHECRI 2010 but model was not published

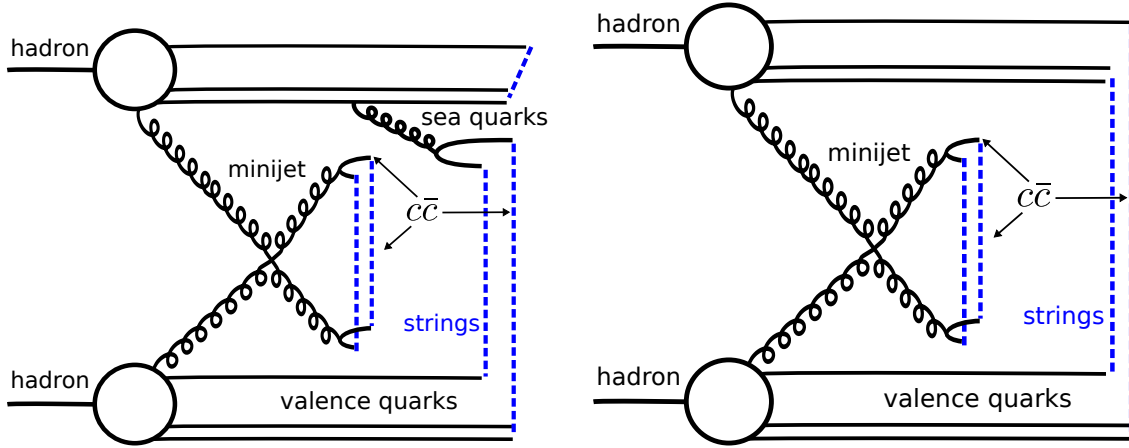


Figure 6.1: Schematic view of an event in SIBYLL with (left) and without (right) remnant. In this particular case a remnant is formed from the valence quarks of one of the projectiles, requiring an additional sea quark pair to connect to the valence quarks of the other hadron. The fragmentation process is symbolized by the blue dashed lines connecting partons which exchange color. The processes that contribute to charm production in the model are marked by arrows.

of the strings, but extends over the whole string. This part of the phenomenological model for charm production is referred to as perturbative component.

Next to the dominant contribution from hard scattering, experiments have shown that there is an asymmetry in charm production in the fragmentation region (i.e. at large x_F) [76, 77], which suggests a contribution from charm production in soft interactions. Two models, which can be used to explain this forward production of heavy flavor, are the *intrinsic charm* model [78] and the *flavor excitation* model [79].

In SIBYLL, a model is chosen which could represent either mechanism by allowing charm quark pairs in the fragmentation of any string attached to soft scattered partons (non-perturbative component). These will include strings between valence quarks. Due to the large momentum fraction carried by the valence quarks and the fact that their flavor is given by the initial hadron, these strings produce the observed asymmetry at large x_F .

In the remnant extended model (Sect. 5) two more sources for charm quarks arise, namely the charm sea rate ($P_{c/s}^{\text{sea}}$) and the charm rate in the fragmentation of the remnant ($P_{c/s}^{\text{Remnant}}$). As the remnant process is designed to replace the concept of the valence string and the leading fragmentation function, it is obvious that the parameters of the non-perturbative component have to be adjusted when using the remnant process in the model. The perturbative component should not be affected much.

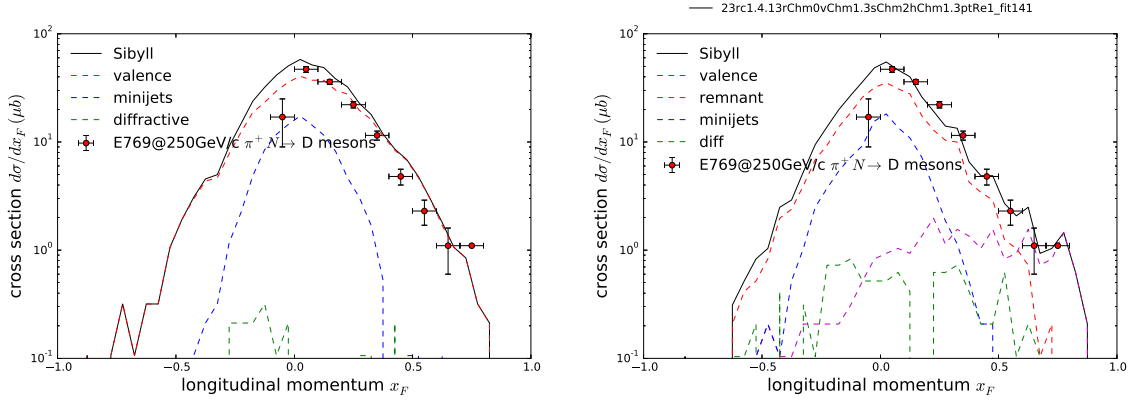
In Fig. 6.1 a schematic view of a non-diffractive interaction in SIBYLL with and without a remnant is shown. The processes contributing to charm production are pointed out. In Fig. 6.2 the contributions from the different processes to the x_F -spectrum of D-mesons in fixed-target π^+ -p collisions at $p_{\text{Lab}} = 250 \text{ GeV}/c$ are shown. The valence string model with a diffractive, soft and a hard charm component is shown on the left and the new with the additional remnant component is shown on the right. Note that with the current setting of parameters (Tab. 6.1) the contribution from the remnant arises purely from the exchange of a sea quark with a fast valence quark, since $P_{c/s}^{\text{Remnant}} = 0.0$. Note also that the component labeled 'valence', in this model corresponds to the sea contribution.

6.2 Tuning of the parameters

The values of the parameters in Eq. 6.1 are adjusted separately for the perturbative and non-perturbative contribution. The perturbative part is tuned to describe the p_{\perp} -spectra of D mesons measured by the ALICE [80] and LHCb [81] experiments in central phase space, since this

Table 6.1: Table of the parameters of charm production in different processes (see Eq. 6.1). The values shown in parentheses are for the remnant model (Sect. 5).

parameter	symbol	value
perturbative component		
asymptotic rate	$P_{0,c/s}^{\text{Hard}}$	0.075 (0.08)
mass threshold	$m_{\text{eff}}^{\text{Hard}}$	10.0 GeV (10.0)
non-perturbative component		
asymptotic rate	$P_{0,c/s}^{\text{Soft}}$	0.007 (0.004)
mass threshold	$m_{\text{eff}}^{\text{Soft}}$	25.0 GeV (10.0)
remnant component		
rate	$P_{c/s}^{\text{Sea}}$	0.0 (0.002)
rate	$P_{c/s}^{\text{Remnant}}$	0.0 (0.0)

**Figure 6.2:** Charm production in SIBYLL without (left) and with (right) the excitation of a remnant.

is where its contribution is expected to be dominant (Fig. 6.4). The parameters for the soft contribution are set to account for the production at low energies (Fig. 6.5).

The numerical values of charm production in the different processes are given in Tab. 6.1. Parameters for both models, the valence string (rc1) and the remnant extended model are shown.

In Fig. 6.3 the cross section for inclusive charm production is shown as a function of the center-of-mass energy. The ALICE data include an extrapolation from central to total phase space. The cross section for D meson production that is measured directly by ALICE is shown by the lower blue points and lines. The dotted line represents the inclusive D meson production cross section without subtracting the decays of resonances of higher mass, e.g. D^* . It is shown here because the low energy measurements are not corrected for this either.

The resulting model correctly describes the rise of the inclusive charm cross section with energy and reproduces the spectra at different energies.

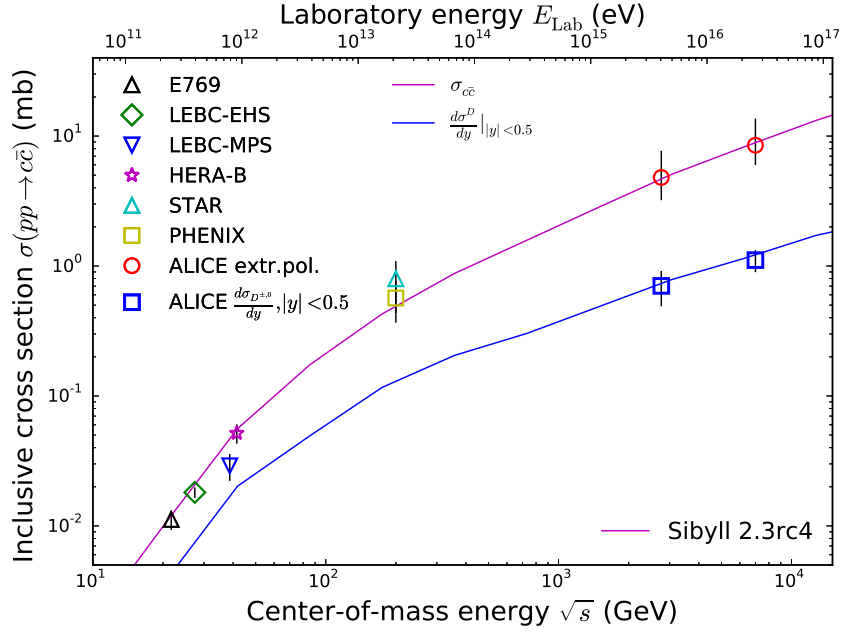


Figure 6.3: Inclusive charm cross sections as a function of cm. energy. The data at low energy are D -meson cross sections in fixed target experiments [76, 82, 83, 84]. The measurements at the highest energies are corrected to $c\bar{c}$ from ALICE [85, 80]. Here data are shown extrapolated to full phase space (red circles) and visible only (blue empty squares). At intermediate energies the data taken at RHIC by the STAR [86] and PHENIX [87] experiments are shown (also extrapolated).

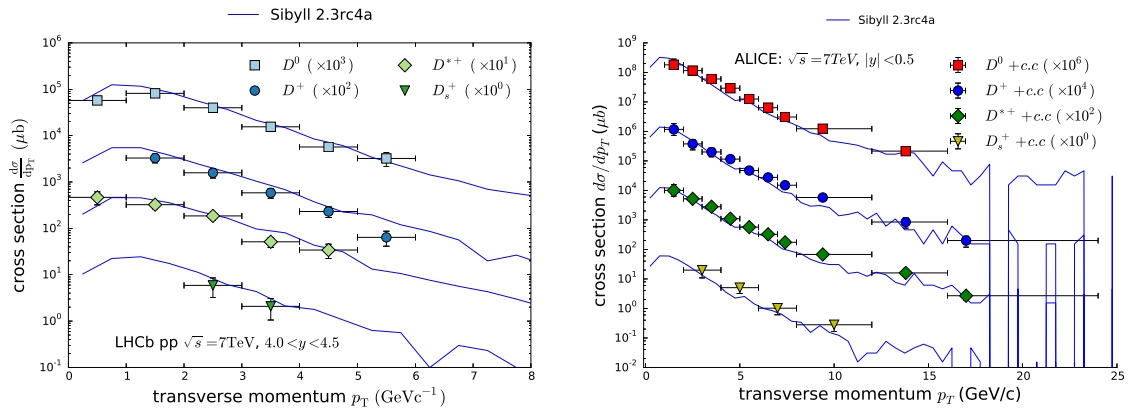


Figure 6.4: Left: Transverse momentum spectrum of different types of D -mesons in the rapidity interval $4.0 < y < 4.5$. Data were taken at $\sqrt{s} = 7$ TeV with the LHCb detector [81]. Right: Transverse momentum spectra of D mesons including vector (D^*) and strange mesons (D_s) at $\sqrt{s} = 7$ TeV. Data taken in mid-rapidity ($|y| < 1$) in the ALICE experiment [80]

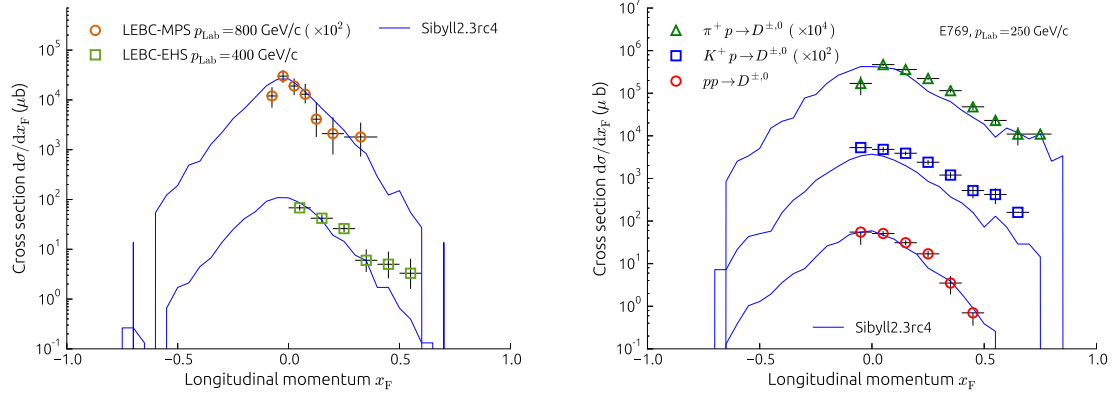


Figure 6.5: Left: Feynman- x spectra of charged charmed mesons ($D^\pm, D^0, \bar{D}^0, D^{*\pm}$) in proton proton fixed target interactions with $p_{\text{Lab}} = 400 \text{ GeV}/c$ [82] and $800 \text{ GeV}/c$ [83]. Right: Feynman- x spectra of charged D mesons in fixed target collisions with proton, π^+ and K^+ projectiles at $p_{\text{Lab}} = 250 \text{ GeV}/c$ [82].

Chapter 7

Tuning of fragmentation parameters

7.1 Baryon production

Even after 50 years of successful application of the quark model [90, 91], baryons are still a puzzle in QCD. In particular the production of baryons in hadronization remains an unsolved problem. In string fragmentation baryons are introduced by allowing the formation of a color triplet state of two quarks, so-called diquarks qq , in the fragmentation chain. The parameters of different diquark combinations in this approach are sufficient to describe the observed baryon multiplicities. A more complex model is the *popcorn model* [92, 93], where the baryons do not have to appear as nearest neighbors in the hadron chain. In SIBYLL 2.1 only the basic diquark model is used.

It was argued and demonstrated on several occasions, that the production of baryons can have a large effect on the number of muons in air showers [20, 19, 18]. The argument is essentially that due to the conservation of baryon number, the number of hadronic sub showers in an air shower increases with increasing number of baryons. With the sub shower in between it is clear that every single additional baryon, produces many additional muons. It is also clear that this mechanism will be particularly effective for baryon production at high energy, since baryons have large masses and need to be produced in pairs. The influence on the number of muons is mostly at low energy.

The ideal environment to study baryon (particle) production in hadronization are $q\bar{q}$ events in e^+e^- collisions. The question remains, however, whether the fragmentation process ($q\bar{q}$: one string) is independent of the environment. After all it is a process associated with large length scales. In particular, the question is if fragmentation is the same in a gluon rich environment like pp collisions at the LHC.

A similar gluon rich environment can be studied in the decay of the Y -resonance through the 3 and 2 gluon decay (see Fig. 7.1). The ratio of baryon production in these decays compared to non resonant $q\bar{q}$ events at similar energy, show an increase of baryon production in the gluon fragmentation [88].

In combination with the low yield of \bar{p} production in SIBYLL compared to the CMS measurement at 7 TeV (see protons in Fig. 7.5) this suggests a model with increased baryon production whenever multiple gluons are involved. This is likely the case whenever multiple parton interactions occur. In particular at high energy ($\sqrt{s} \geq \mathcal{O}(\text{TeV})$) where gluon scattering is dominant. The diquark production rate P_{diq} in string fragmentation is therefore increased if more than one hard or soft minijet is sampled

$$P_{\text{diq}} \rightarrow P_{\text{diq},0} + P_{\text{diq},\text{minijet}} \cdot \min(n_{\text{hard}} + n_{\text{soft}} - 1, 1) . \quad (7.1)$$

This extension to the baryon production model in SIBYLL was previously described in Ref. [61].

The measurement of the ratio of charged pions to protons and antiprotons as a function of central multiplicity $dN_{\text{ch}}/d\eta$ [57] that is shown in Fig. 7.1 requires the increase to be independent of the number of minijets, which is consistent with the result from Y decay.

The resulting evolution of antiproton production is shown in Fig. 7.2 compared to a collection of fixed target data at low energy [89]. The integrated measurement in the phase space covered

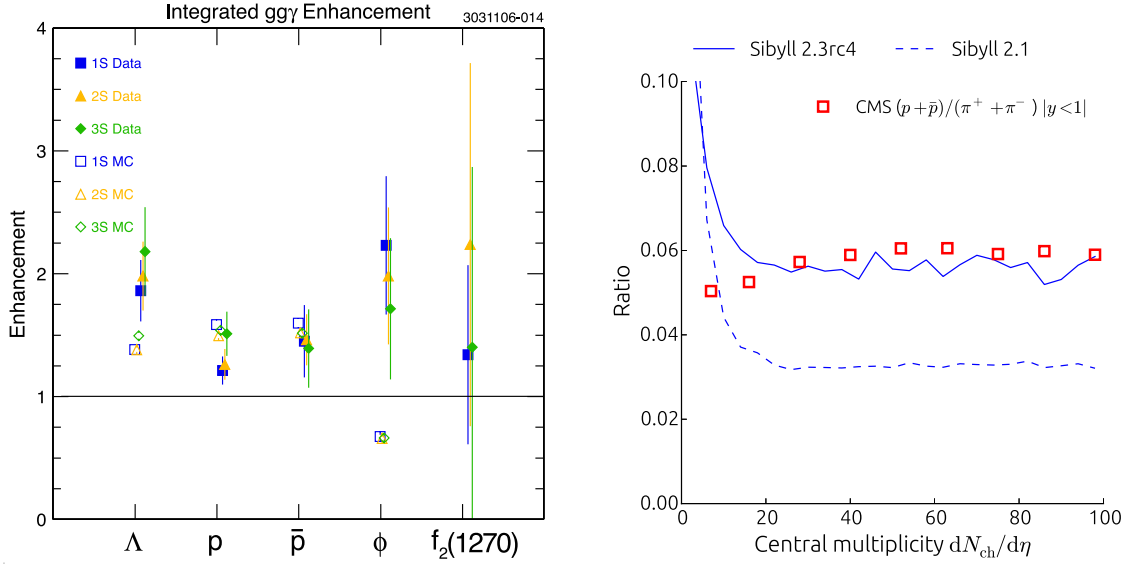


Figure 7.1: Left: Baryon enhancement in gg fragmentation compared to $q\bar{q}$ [88]. Right: Ratio of baryons to charged pions as a function of $dN_{ch}/d\eta$. Large central multiplicities are mostly central collision events with many minijets, low central multiplicities correspondingly have a low number of minijets. The flat ratio suggests baryon production is independent of the number of minijets.

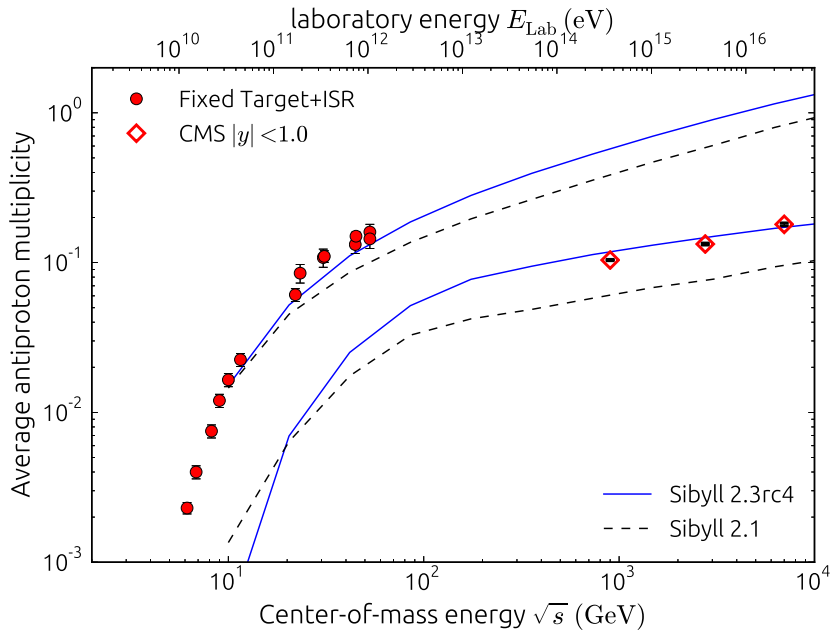


Figure 7.2: Antiproton production in pp collisions. Data at low energy are from fixed target experiments and ISR [89]. High energy data (CMS) are central phase space ($|y| < 1$) only [57].

by the central CMS detector is shown as well. Within the phase space of the CMS detector, antiproton production is dominated by the minijets. This can be used to determine the value of $P_{diq,minijet}$ in Eq. 7.1. The value of $P_{diq,0}$ on the other hand is determined by the low energy data. To produce enough slow protons at lower energies (see discussion of remnant model in Sect. 5) the popcorn mechanism was reactivated. This allows the proton in the first pair of strings (valence strings) to switch place with a neighboring meson in the hadron chain which makes it more likely to carry less energy.

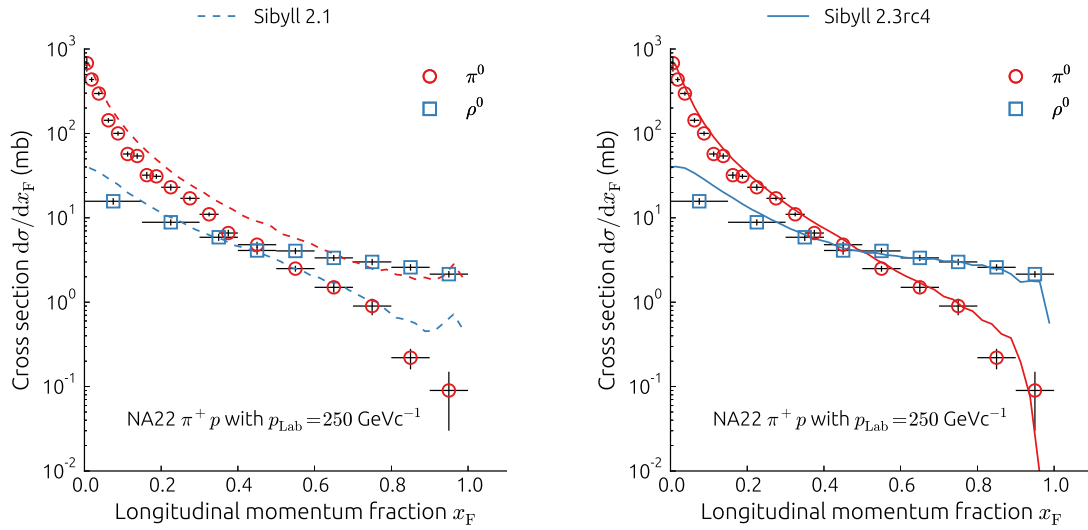


Figure 7.3: Neutral pion and ρ production in π^+ -p collisions [94, 95]. Note how the data points cross at $x_F = 0.4$, giving more ρ^0 at large x_F than π^0 . On the left SIBYLL 2.1 is shown, on the right SIBYLL 2.3.

The results on air shower simulations in particular the number of muons are shown in Sect. 10.1.2.

7.2 Leading ρ^0 production

Muon production in air showers is directly linked to the size of the hadronic cascade [20]. The balance between the hadronic and electromagnetic cascade is largely determined by the production of neutral pions. For the em. cascade the most important contribution comes from neutral pions produced in the first few interactions, since these can transfer the largest amount of energy (see also discussion in Sect. 2.3). Neutral pions produced in later stages have a negligible impact on the em. cascade. They do however have a large impact on the hadronic cascade. Every neutral pion that is produced removes energy from the hadronic cascade, which at this point still contains 10% of the primary energy. The dominant particles at this stage in the cascade are charged pions, which means neutral pions can be produced as leading particles ($\pi^\pm + Air \rightarrow \pi^0 + X$), carrying a large fraction of the energy of the interacting pion to the em. cascade and effectively terminating that hadronic sub shower. Reducing the number of neutral pions produced in meson nucleus interactions therefore could significantly increase the number of muons by increasing the number of hadronic sub showers in the late stages of an air shower [19]. At the same time the em. cascade would be unaffected.

The leading particle effect for protons was already discussed in the context of the remnant (Sect. 5). While the so-called *charge exchange* reaction can be neglected for nucleons ($p \rightarrow n$), at least in terms of air shower development, for the reasons given above it is of great importance in case of meson interactions.

In the valence string model as used in SIBYLL 2.1, the interacting pion, e.g. π^+ , is split into quark-antiquark (u, \bar{d}) that then each form one end of a pair of strings. The other ends will be attached to the valence quarks in a target nucleon. One of the two quarks in the meson is said to be leading, so it is assigned a large fraction of the initial momentum. The hadrons emerging from these two quarks are determined by vacuum quark-antiquark pairs (u, d, s, c) produced in string fragmentation. If one only considers the light quarks (u, d , heavy strange and charm are less common) for the pairs then in case of either valence quark (u or \bar{d}), the hadron can be a π^+ again or a π^0 . Since the vacuum pairs sampled in string fragmentation are symmetric in the light flavors, a significant fraction of leading pions will be produced as neutrals in the model.

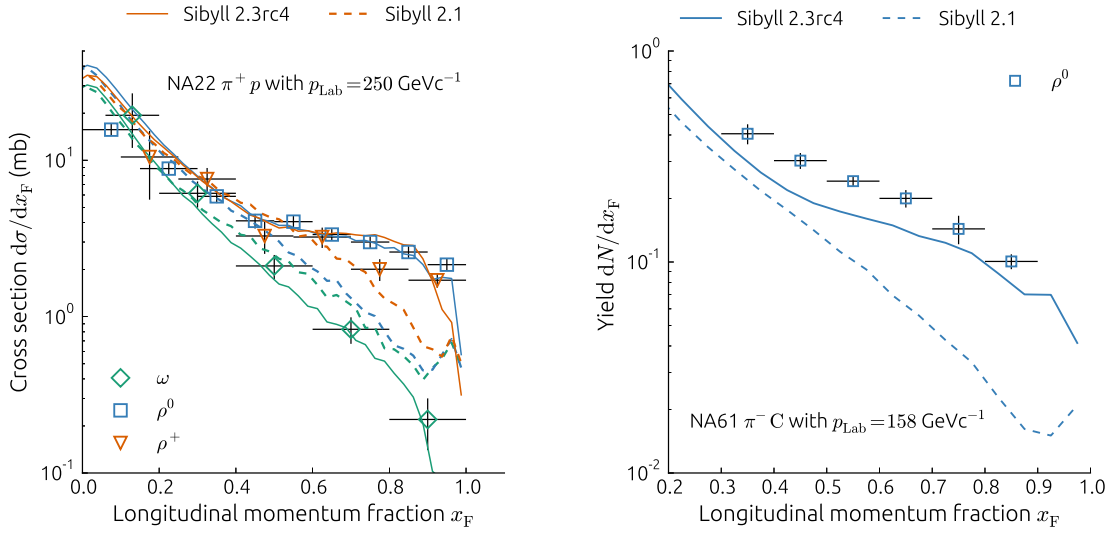


Figure 7.4: Left: Vector meson production ($\rho^{+,0}, \omega$) in π^+ -p collisions [95]. Right: ρ^0 production in π^- -C collisions [96].

The conversion rate is reduced a little by spin considerations. If the quarks are combined with spin one instead of spin zero ($P_{\text{spin1}}/P_{\text{spin0}} = 0.3$), then the resulting hadrons are ρ -resonances instead of π . Neutral ρ decay into charged pions, so the final conversion fraction (after decay) from charged to neutral pions is slightly lower than 0.5.

That is the situation in the model for non-diffractive interactions. In case of diffraction dissociation, which actually is the dominant process for particle production at large x_F , the situation is similar since dissociation most often happens through string fragmentation.

Data taken in π^+ -p fixed target collisions [94, 95] on the other hand show a leading component for neutral ρ -resonances but almost no contribution to neutral pions (see Fig. 7.3).

In order to reproduce this leading ρ enhancement and the suppression for neutral pions in the model a phenomenologic approach was used. Since diffraction dissociation is dominant at large x_F , increasing the spin-1 rate at the forward string end (first hadron) and forbidding the formation of neutral pions already describes the data very well. In the intermediate range of x_F the remnant de-excitation is dominant. Here again spin-1 formation rate and π^0 suppression have the desired effect. It should be stressed that neutral pions have to be actively suppressed in the fragmentation process. Only increasing the spin-1 rate, which naturally also reduces the amount of neutral pions, has proven not to be sufficient, within SIBYLL at least.

There is an additional complication namely that increasing the spin-1 rate also increases the production of the ω -resonance which is not observed in data (see Fig. 7.4-left). Since isospin is currently not accounted for in the fragmentation model, the ω -resonances suppression was added ad-hoc like for the π^0 . An analog suppression of neutrals and spin-enhancement was implemented for strange mesons, that according to the NA22 measurement behave similar [97].

In the right plot in Fig. 7.3 the results for the extended model are shown. The production of ρ^0, ρ^+ and ω are shown in Fig. 7.4 on the left.

On the right in Fig. 7.4 the production of ρ^0 mesons in nuclear collisions measured recently in the NA61 experiment [96] are shown. The model lines represent something like a prediction since the model was cooked up for the NA22 data that was taken in π -p collisions while the NA61 measurement was done with a carbon target. The misrepresentation of neutral ρ in nuclear collisions is not so surprising given the phenomenological nature of the model. It is not clear at the moment whether and how the model can be further extended to describe all the data.

At the same time additional measurements of neutral pions in nuclear collisions would be needed to show that their production is also suppressed as with proton targets.

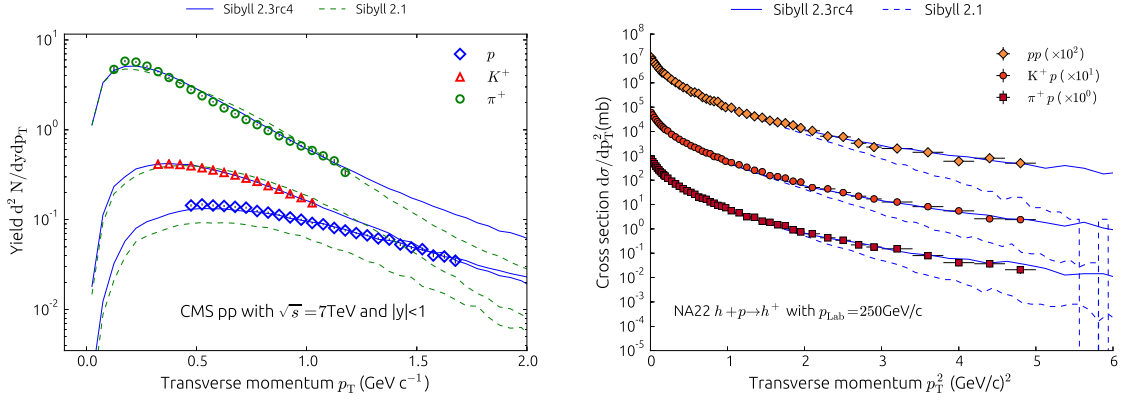


Figure 7.5: Left: Transverse momentum distribution of positive charged hadrons measured with the CMS detector at $\sqrt{s} = 7$ TeV [57]. The model with the exponential distribution in m_T is shown by the full line, the one with Gaussian p_T by the dashed line. The improvement in the normalization of the proton spectrum (blue diamonds) is due to the extended baryon production model (Sect. 7.1). Right: Transverse momentum distribution of hadrons with positive charge measured in the NA22 fixed target experiment with beam momentum $p_{\text{Lab}} = 250$ GeV/c [98].

How the extended model affects air shower simulations and especially the number of muons is presented in Sect. 10.1.2.

7.3 Transverse momentum

The contribution to transverse momentum from hard scattering has already been discussed in Sect. 4.2 in context of the altered PDFs. Contribution from soft interactions and string fragmentation are discussed here.

7.3.1 String p_{\perp}

In the original string model the transverse momentum that is assigned to the quark pairs in the fragmentation process follows a Gaussian distribution [99]. The distribution observed in hadron collision experiments [98, 100] however, closely resembles the exponential distribution in transverse mass predicted by ‘thermal’ particle production models [51]. Therefore the distribution of transverse momentum in string fragmentation has been changed to an exponential distribution in transverse mass $m_T = \sqrt{p_T^2 + m^2}$.

$$f(m_{T,i}) \sim \exp\left(-\frac{m_{T,i} - m_i}{\langle m_{T,i} \rangle}\right). \quad (7.2)$$

The energy dependence of the average transverse mass is parameterized as before by

$$\langle m_{T,i} \rangle = m_{0,i} + c \log_{10} \left(\frac{s}{(10 \text{ GeV})^2} \right)^b, \quad (7.3)$$

with the parameters c and b and the masses $m_{0,i}$. The exponent is $b = 2$ and the values for m_0 and c used in the model are summarized in Tab. 7.1.

7.3.2 Soft p_{\perp}

Without a microscopic model for soft interactions the shape of the transverse momentum spectrum can only be guessed. In SIBYLL 2.1 it is assumed to be Gaussian similar to the p_{\perp} -distribution used in string fragmentation. The only principal restriction comes from having to match the p_{\perp} -distribution in hard scattering at the transition p_{\perp}^{\min} .

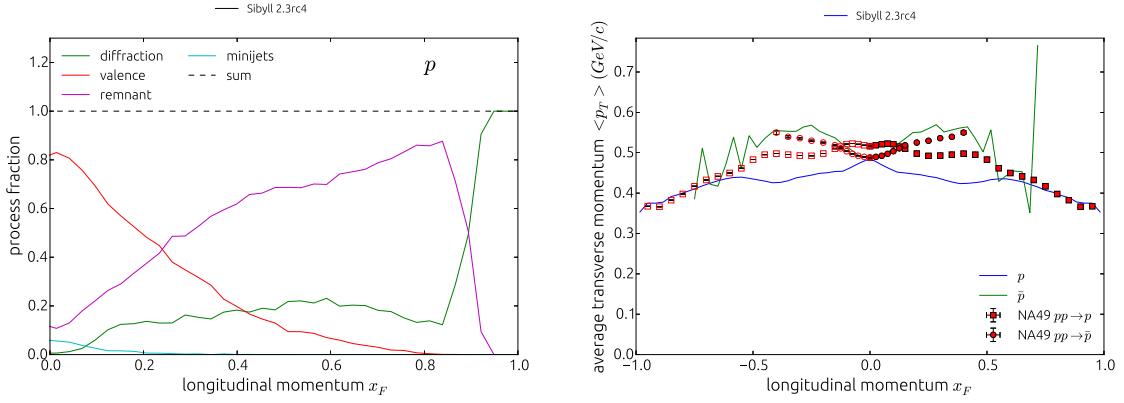


Figure 7.6: Left: Process fractions in the proton spectrum for SIBYLL 2.3. Note that ‘valence’ in the remnant model refers to the pair of strings stretched between sea quark pairs. Right: Seagull plot of protons and antiprotons in pp collisions at $p_{\text{Lab}} = 158 \text{ GeV}$.

Table 7.1: Table of the transverse momentum parameters for different partons.

parton	m_0	c
u, d	0.18	0.006
s	0.28	0.007
c	0.308	0.165
diq	0.3	0.05
$c - diq$	0.5	0.165
$sea q$	0.6	0.006
$valence q$	0.1	0.006

7.3.3 Remnant p_{\perp}

In SIBYLL 2.1 the first soft interaction is treated separately to account for the remnant (valence strings). The transverse momentum distribution used here is again the same as in string fragmentation but with a special set of parameters, chosen to describe p_{\perp} -distributions of leading particles at low energy (see Tab. 7.1).

In the new remnant model, transverse momentum is created in the interaction that transfers mass to the remnants. The interaction is the same as in diffraction dissociation, so essentially elastic scattering. The p_{\perp} -spectrum is therefore taken to be similar to the elastic peak

$$f(p_{\perp}) \sim e^{-B(s)t}, \quad (7.4)$$

albeit with new parameters for the slope $B(s) = \max(0.2, 7.0 - 2.5 \log(M^2/s))$. The parameters are determined by trying to reproduce the p_{\perp} -spectra of pion, kaons and protons measured in NA49. Particularly useful are the x_F -profiles of the transverse momentum spectra (so-called *seagull plot*) because diffraction, remnant break-up and soft sea scattering each dominate in different x_F -regions (see Fig. 7.6).

In Fig. 7.5 the measured transverse momentum distributions for pions, kaons and protons in pp collisions at a c.m. energy of 7 TeV are shown [57]. The difference between the shapes of the model predictions are due to the different underlying distributions in string fragmentation discussed before. The difference in scale in case of the protons is due to the increased production of baryons in central minijets mentioned before (Sect. 7.1).

The central phase space covered by the CMS measurement ($|y| < 1$) is dominated by particle production from minijets. The measured p_{\perp} -spectra are therefore sensitive to transverse momentum assigned in hard scattering and from fragmentation. Soft interactions are much more prominent at lower c.m. energies. Fig. 7.5 shows the transverse momentum spectrum of positive charged particles measured in the fixed target experiment NA22 [98] at a c.m. energy of 22 GeV. The measurement covers the entire phase space so the spectrum is influenced by all processes present at that energy. To describe the long tail of the spectrum the distribution of transverse momentum of the valence and sea quarks in the soft interaction is sampled from an exponential distribution in transverse mass ($m = 0.0 \text{ GeV}$).

Chapter 8

Intermediate states in the Glauber model of nuclear collisions

8.1 The Glauber model and inelastic screening

The microscopic picture of hadron interactions in SIBYLL that was introduced in Sect. 3.1 can be extended to hadron nucleus collisions by means of the Glauber model.

In the following the extension of the calculation to include the effect of inelastic intermediate states is described. The basic formalism for the extension of the Glauber model with a two channel approach has been used to calculate the effect of the intermediate states on the inelastic cross section in p-Air interactions [101]. For an implementation in the context of SIBYLL the calculation has to be extended to include diffractive cross sections as well.

8.1.1 General formalism

The basic idea of the Glauber model [43, 44] is that the interaction of a beam hadron with multiple target nucleons factorizes, i.e. the interactions with the individual nucleons are considered to be independent. This is true if the energy of the projectile is much larger than the nuclear binding energy.

Following the convention in Sect. 3.1, the elastic scattering amplitude for a hadron-nucleon interaction is defined in terms of the Fourier transform of the profile function $\Gamma(\vec{b})$ by,

$$f^{hN}(s, \vec{q}^2) = \frac{ik}{2\pi} \int e^{i\vec{q}\cdot\vec{b}} \Gamma(\vec{b}) d^2\vec{b}, \quad (8.1)$$

In impact parameter space the interaction is represented as the overlap between the constituent profiles (see Sect. 3.1). s is the Mandelstam variable defined by $s = (p_h + p_N)^2$ and the momentum transfer is $\vec{q} = \vec{k} - \vec{k}'$. The scattering amplitude for a hadron-nucleus interaction where the nucleus undergoes a transition from initial state ψ_i to final state ψ_f is then given by:

$$f_{fi}^{hA}(s, \vec{q}^2) = \frac{ik}{2\pi} \int e^{i\vec{q}\cdot\vec{b}} \psi_f^*(\vec{r}_1 \dots \vec{r}_A) \Gamma_{hA}^{\text{ela}}(\vec{b}, \vec{s}_1 \dots \vec{s}_A) \psi_i(\vec{r}_1 \dots \vec{r}_A) d^2\vec{b} \prod_{j=1}^A d^3\vec{r}_j. \quad (8.2)$$

Factorization of the interactions means the total nuclear profile function $\Gamma_{hA}^{\text{ela}}(\vec{b}, \vec{s}_1 \dots \vec{s}_A)$ (also called impact parameter amplitude) contains the product of the individual hadron-nucleon profile functions

$$\Gamma_{hA}(\vec{b}, \vec{s}_1 \dots \vec{s}_A) = 1 - \prod_{j=1}^A e^{i\chi_j(\vec{b}-\vec{s}_j)} = 1 - \prod_{j=1}^A [1 - \Gamma_{hN}(\vec{b} - \vec{s}_j)]. \quad (8.3)$$

The vectors \vec{s}_i represent the projections of the positions \vec{r}_i of the individual nucleons in the nucleus onto the plain perpendicular to the projectile momentum (\vec{k}), i.e. the projection onto impact parameter space.

The function $\chi(s, \vec{b})$ in the first step in Eq. (8.3) is the *eikonal function* Γ_{hN} which also appeared in the definition of the amplitude for hadron-nucleon scattering (see Sect. 3.1). Here it is extended to the case of nuclei. The term $e^{i\chi}$ is sometimes called the eikonal wave function or also scattering matrix S . Here the factorization becomes most apparent since in general $\sigma \sim 1 - S$ and evidently applying $S_i = e^{i\chi}$ to Eq. (8.3) requires $S = \prod_i^A S_i$.

The amplitude in Eq. (8.2) is the most general form of the amplitude, allowing for transitions of the nucleus between different states. The elastic scattering amplitude is recovered from the general case by taking $\psi_i = \psi_f$.

The convolution of the nuclear wave functions ψ_j and the hadron-nucleus amplitude $\Gamma_{hA}(\vec{b}, \vec{s}_1 \dots \vec{s}_A)$ can be combined to the generalized elastic hadron-nucleus profile function:

$$\Gamma_{hA}^{\text{ela}}(\vec{b}) = \int \psi_i^*(\vec{r}_1 \dots \vec{r}_A) \left\{ 1 - \prod_{j=1}^A [1 - \Gamma_{hN}(\vec{b} - \vec{s}_j)] \right\} \psi_i(\vec{r}_1 \dots \vec{r}_A) \prod_{j=1}^A d^3\vec{r}_j. \quad (8.4)$$

Neglecting correlations between the different nucleons in the nucleus, which for the time scales that occur in high energy interactions is a reasonable assumption, the wave function of the nucleus factorizes $\psi_{\text{init}} = \prod_j \psi_j(\vec{r}_j)$ so

$$\psi_i^*(\vec{r}_1 \dots \vec{r}_A) \psi_i(\vec{r}_1 \dots \vec{r}_A) = \prod_j \rho_j(\vec{r}_j). \quad (8.5)$$

The integral in Eq. (8.4) then becomes the convolution of the nucleon densities with the hadron-nucleon profile

$$\Gamma_{hA}^{\text{ela}}(\vec{b}) = \left\{ 1 - \prod_{j=1}^A \left[1 - \int \Gamma_{hN}(\vec{b} - \vec{s}_j) \rho_j(\vec{r}_j) d^3\vec{r}_j \right] \right\}. \quad (8.6)$$

Through the optical theorem (Sect. 3.1) the total and the elastic cross section can then be expressed as

$$\sigma_{hA}^{\text{tot}}(s) = \frac{4\pi}{|\vec{k}|} \text{Im} \left\{ f_{\text{ela}}^{hA}(s, \vec{q}^2 \rightarrow 0) \right\} = 2\text{Re} \left\{ \int \Gamma_{hA}^{\text{ela}}(\vec{b}) d^2\vec{b} \right\} \quad (8.7)$$

$$\sigma_{hA}^{\text{ela}}(s) = \int \frac{1}{|\vec{k}|^2} \left| f_{\text{ela}}^{hA}(s, \vec{q}^2) \right|^2 d^2\vec{q} = \int \left| \Gamma_{hA}^{\text{ela}}(\vec{b}) \right|^2 d^2\vec{b}. \quad (8.8)$$

8.1.2 Production cross section

For the implementation in the event generator the decomposition of the inelastic cross section into diffractive and non-diffractive contributions is needed. For the development of air showers only the interactions of the projectile (atmosphere at rest) are of any importance. The remnants of the (target) nucleus can generally be neglected. Interactions in which the projectile stays intact and only the nucleus is excited and maybe breaks apart (so-called *quasi elastic*), in terms of the effects on air showers do not need to be distinguished from an elastic interaction. The important quantity is therefore not the full inelastic cross section but rather the so-called *production cross section*:

$$\sigma_{\text{prod}} = \sigma_{\text{inel}} - \sigma_{\text{q,ela}}. \quad (8.9)$$

$\sigma_{\text{q,ela}}$ is given by the quasi elastic events where the target nucleus changes state but no additional particles are produced. This could in principle be calculated by setting $\psi_i \neq \psi_f$ in Eq. (8.4). In practice calculating $\Gamma_{hA}^{\text{q,ela}}$ is complicated and it is not necessary as shall be seen shortly.

The inelastic cross section can be calculated from the total and elastic cross sections which are determined by Eq. (8.7) and Eq. (8.8). The production cross section then is given by

$$\sigma_{\text{prod}} = \sigma_{\text{tot}} - (\sigma_{\text{ela}} + \sigma_{\text{q.ela}}) . \quad (8.10)$$

The sum of the elastic and quasi elastic cross section can be calculated more easily than the separate contributions because the nuclear wave functions form a complete and orthonormal set. Based on Eq. (8.4) the sum of the cross sections is given by

$$\sigma_{\text{ela}} + \sigma_{\text{q.ela}} = \int |\Gamma_{hA}(\vec{b}, \vec{s}_1 \dots \vec{s}_j)|^2 \prod_{j=1}^A [\rho_j(\vec{r}_j) d^3\vec{r}_j] d^2\vec{b} , \quad (8.11)$$

where $\prod_{j=1}^A \rho_j(\vec{r}_j)$ is the product of the spatial distributions of the individual nucleons in the nucleus.

Note the difference to σ_{ela} in Eq. (8.8) where the hadron-nucleon amplitude is convolved with the nucleon distributions, forming the generalized nuclear profile $\Gamma_{hA}^{\text{ela}}(\vec{b})$, and then its absolute square is integrated over impact parameter space while here the order is inverted. The absolute square of the product of the hadron-nucleon profiles Γ_{hN}^{ela} is convolved with the nucleon distributions and then everything is integrated in \vec{b} -space.

8.2 Diffraction dissociation in nuclear collisions

8.2.1 Two channel model

So far inelastic intermediate states have not appeared in the calculation. In order to include them Eq. (8.2) needs to be extended. Instead of choosing an explicit set of intermediate states we combine all intermediate states into one effective state and, in addition, take the scattering amplitude of that state to be the same as the elastic hadron-nucleon amplitude. That way it is not necessary to determine the individual amplitudes, which would be difficult, since it is not clear which intermediate states should be taken into account at all. We also avoid changing the structure of the nuclear amplitude (Eq. (8.2)) and therefore do not need to find a way to combine everything without breaking unitarity. To parameterize the amplitude for producing an inelastic intermediate state we introduce only one free parameter: the coupling λ .

This approach is known as the *two-channel model* and it was already applied to describe diffractive interactions in hadron-nucleon collisions (see Sect. 3.1.4). Since the basis of the Glauber model is that nucleons participate individually in the collision it is clear that only such states are allowed as intermediates that, in some form, preserve the identity of the nucleon. States that fulfill this are excitations of the nucleons which also appear in diffractive interactions. The two-channel approach introduced in the context of diffraction by Good and Walker [40] is therefore a natural choice to introduce inelastic intermediate states to the Glauber calculation. Another advantage of this approach is that the case of coherent nuclear diffraction is already included.

Similar to the case of diffraction in hadron-hadron collisions in Sect. 3.1.4 the two-channel Glauber model can be written in matrix-vector form by choosing

$$|p\rangle = \begin{pmatrix} 1 \\ 0 \end{pmatrix} \text{ and } |p^*\rangle = \begin{pmatrix} 0 \\ 1 \end{pmatrix} , \quad (8.12)$$

where $|p\rangle$ represents the proton and $|p^*\rangle$ is the effective intermediate state or diffractive final state. This means the generalized amplitude is

$$\hat{\Gamma}_{hN} = \begin{pmatrix} 1 & \lambda \\ \lambda & 1 \end{pmatrix} \Gamma_{hN}^{\text{ela}} , \quad (8.13)$$

so that one recovers $\Gamma_{p \rightarrow p} = \langle p | \hat{\Gamma} | p \rangle = \Gamma_{hN}^{\text{ela}}$ for the elastic case and similarly $\Gamma_{p \rightarrow p^*} = \langle p | \hat{\Gamma} | p^* \rangle = \lambda \cdot \Gamma_{hN}^{\text{ela}}$ for the transition into an excited state.

Using these definitions the elastic ($p \rightarrow p$) hadron-nucleus amplitude (Eq. (8.4)) is

$$\begin{aligned} \Gamma_{hA}^{\text{ela}}(\vec{b}) &= \int \psi_i^*(\vec{r}_1 \dots \vec{r}_A) \langle p | \hat{\Gamma}_{hA}(\vec{b}, \vec{s}_1 \dots \vec{s}_A) | p \rangle \psi_i(\vec{r}_1 \dots \vec{r}_A) \prod_j^A d^3 \vec{r}_j \\ &= \int \psi_i^*(\vec{r}_1 \dots \vec{r}_A) \langle p | \left[1 - \prod_{j=1}^A [1 - \hat{\Gamma}_{hN}(\vec{b} - \vec{s}_j)] \right] | p \rangle \psi_i(\vec{r}_1 \dots \vec{r}_A) \prod_j^A d^3 \vec{r}_j. \end{aligned} \quad (8.14)$$

The amplitude for the process where the beam hadron is in an excited state after the collision ($p \rightarrow p^*$), i.e. diffraction dissociation, is given by replacing $\langle p |$ with $\langle p^* |$.

However, the same arguments as in the case of the inelastic cross section above (Sect. 8.1) apply, so the appropriate definition of the cross section for diffractive dissociation of a hadron on a nucleus is $\sigma_{hA}^{\text{SD}} = \sigma_{hA}^{\text{SD,ela}} + \sigma_{hA}^{\text{SD,q,ela}}$.

Applying orthonormality and completeness as in the calculation of $\sigma^{\text{ela}} + \sigma^{\text{q,ela}}$ in Eq. (8.11) leads to

$$\begin{aligned} \sigma_{hA}^{\text{SD,ela}} + \sigma_{hA}^{\text{SD,q,ela}} &= \int |\langle p^* | \hat{\Gamma}_{hA}^*(\vec{b}, \vec{s}_1 \dots \vec{s}_j) | p \rangle|^2 \prod_{j=1}^A [\rho_j(\vec{r}_j) d^3 \vec{r}_j] d^2 \vec{b} \\ &= \int \left| \langle p^* | p \rangle - \langle p^* | \prod_{j=1}^A [1 - \hat{\Gamma}_{hN}(\vec{b} - \vec{s}_j)] | p \rangle \right|^2 \prod_{j=1}^A [\rho_j(\vec{r}_j) d^3 \vec{r}_j] d^2 \vec{b}. \end{aligned} \quad (8.15)$$

Diagonalizing $\hat{\Gamma}$

The transformation to a basis where $\hat{\Gamma}_{hN}$ is diagonal is of the form $U \hat{\Gamma} U^T$ where U is an orthogonal matrix. Using $U U^T = 1$, $\hat{\Gamma}_{hA}^{(*)}(\vec{b}, \vec{s}_1 \dots \vec{s}_j)$ of Eq. (8.15) and Eq. (8.14) can be brought into diagonal form.

$$\begin{aligned} \hat{\Gamma}_{hA}(\vec{b}, \vec{s}_1 \dots \vec{s}_j) &= 1 - \langle p | U^T U \prod_{j=1}^A [1 - \hat{\Gamma}_{hN}] U^T U | p \rangle \\ \hat{\Gamma}_{hA}^*(\vec{b}, \vec{s}_1 \dots \vec{s}_j) &= (-1) \cdot \langle p^* | U^T U \prod_{j=1}^A [1 - \hat{\Gamma}_{hN}] U^T U | p \rangle. \end{aligned} \quad (8.16)$$

Taking the explicit form of the hadron-nucleon amplitude $\hat{\Gamma}_{hN}$ from Eq. (8.13), U such that $U \hat{\Gamma} U^T = \text{diag}$ is given by

$$U = \frac{1}{\sqrt{2}} \begin{pmatrix} 1 & 1 \\ 1 & -1 \end{pmatrix}. \quad (8.17)$$

The eigenvalues of $\hat{\Gamma}_{hN}$ are $(1 \pm \lambda)$ with the corresponding eigenvectors $|\pm\rangle = U|p, p^*\rangle = 1/\sqrt{2}(|p\rangle \pm |p^*\rangle)$. The physical states $|p\rangle$ and $|p^*\rangle$, in terms of the basis of eigenvectors are

$$\begin{aligned} |p\rangle &= \frac{1}{\sqrt{2}} (|+\rangle + |-\rangle) \\ |p^*\rangle &= \frac{1}{\sqrt{2}} (|+\rangle - |-\rangle). \end{aligned} \quad (8.18)$$

Expressing the diagonal form $U \hat{\Gamma}_{hN} U^T$ in terms of the projections $|\pm\rangle\langle\pm|$ the expressions for $\hat{\Gamma}_{hA}$ and $\hat{\Gamma}_{hA}^*$ in Eqs. (8.16) become

$$\begin{aligned} \Gamma_{hA}^{(*)}(\vec{b}, \vec{s}_1 \dots \vec{s}_A) &= \frac{1}{2} (\langle + | \pm \langle - |) \left[1 - \prod_{j=1}^A [1 - (1 + \lambda) \Gamma_{hN}^j] |+\rangle\langle + | \right. \\ &\quad \left. + \prod_{j=1}^A [1 - (1 - \lambda) \Gamma_{hN}^j] |-\rangle\langle - | \right] (|+\rangle + |-\rangle), \end{aligned} \quad (8.19)$$

where the \pm represents the different channels $p \rightarrow p$ and $p \rightarrow p^*$ and $\Gamma_{hN}^j = \Gamma_{hN}(\vec{b} - \vec{s}_j)$.

The whole expression finally can be simplified to

$$\Gamma_{hA}(\vec{b}, \vec{s}_1 \dots \vec{s}_A) = \frac{1}{2} - \frac{1}{2} \prod_{j=1}^A [1 - (1 + \lambda) \Gamma_{hN}^j] - \frac{1}{2} \prod_{j=1}^A [1 - (1 - \lambda) \Gamma_{hN}^j] \quad (8.20)$$

$$\Gamma_{hA}^*(\vec{b}, \vec{s}_1 \dots \vec{s}_A) = -\frac{1}{2} \prod_{j=1}^A [1 - (1 + \lambda) \Gamma_{hN}^j] + \frac{1}{2} \prod_{j=1}^A [1 - (1 - \lambda) \Gamma_{hN}^j]. \quad (8.21)$$

8.2.2 Calculation of the cross sections

The cross sections that are ultimately needed for the event generator are the production cross section σ_{prod} and the diffractive cross section σ_{SD} . To determine these, according to $\sigma_{\text{prod}} = \sigma_{\text{tot}} - (\sigma_{\text{ela}} + \sigma_{\text{q.ela}})$, σ_{tot} (Eq. (8.7)), $\sigma_{hA}^{\text{ela}} + \sigma_{hA}^{\text{q.ela}}$ (Eq. (8.11)) and $\sigma_{hA}^{\text{SD,ela}} + \sigma_{hA}^{\text{SD,q.ela}}$ (Eq. (8.15)) have to be calculated. This requires the input of the hadron-nucleon amplitude $\Gamma_{hN}(\vec{b})$ and the nuclear densities $\rho_j(\vec{r}_j)$.

For light nuclei ($A < 18$) the nuclear potential can be approximated by a harmonic oscillator so the ρ_j can be taken to be the first (4 states) and second eigenfunction (12 states)

$$\rho_s(\vec{r}) = \frac{1}{\pi^{3/2} a_0^3} e^{-r^2/a_0^2} \quad \text{and} \quad \rho_p(\vec{r}) = \frac{2r^2}{3\pi^{3/2} a_0^5} e^{-r^2/a_0^2}. \quad (8.22)$$

For the hadron-nucleon amplitude, in principle, the full amplitude $a(s, \vec{b})$ described in Sect. 3.1 could be used. In order to be able to do the convolution of the amplitude with the nuclear densities analytically, the standard Gaussian parameterization for the amplitude is chosen

$$\Gamma_{hN}(\vec{b}) = (1 - i\rho_{hN}) \frac{\sigma_{hN}^{\text{tot}}}{4\pi B_{hN}^{\text{ela}}} \exp\left\{-\frac{\vec{b}^2}{2B_{hN}^{\text{ela}}}\right\}, \quad (8.23)$$

where ρ_{hN} denotes the ratio of the real and the imaginary part of the amplitude and B_{hN}^{ela} is the slope of the elastic scattering peak in the exponential approximation (Sect. 4.1).

With this definition the amplitude for elastic hadron-nucleus scattering $\Gamma_{hA}^{\text{ela}}(\vec{b})$ (Eq. (8.6)) can be written down explicitly for nuclei with $4 < A < 18$

$$\Gamma_{hA}^{\text{ela}}(\vec{b}) = 1 - \left(1 - (1 - i\rho_{hN}) G_s(\vec{b})\right)^4 \left(1 - (1 - i\rho_{hN}) G_p(\vec{b})\right)^{A-4}, \quad (8.24)$$

where the convolution of the Gaussian amplitude with the harmonic oscillator functions (Eq. (8.22)) is denoted by $G_s(\vec{b})$, respectively $G_p(\vec{b})$,

$$\begin{aligned} G_s(\vec{b}) &= \frac{\sigma_{hN}^{\text{tot}}}{8\pi\gamma^2} \exp\left\{-\frac{\vec{b}^2}{4\gamma}\right\} \\ G_p(\vec{b}) &= \frac{\sigma_{hN}^{\text{tot}}}{8\pi\gamma^2} \left[1 - \frac{a_0^2}{6\gamma^2} \left(1 - \frac{\vec{b}^2}{4\gamma^2}\right)\right] \exp\left\{-\frac{\vec{b}^2}{4\gamma}\right\}. \end{aligned} \quad (8.25)$$

Since the amplitude and the nuclear densities are essentially Gaussian functions the convolution functions $G_{s,p}(\vec{b})$ are again Gaussian profiles, now with the width parameter

$$\gamma^2 = \frac{1}{4} a_0^2 + \frac{1}{2} B_{hN}^{\text{ela}}. \quad (8.26)$$

σ_{tot} can be calculated by integrating $\Gamma_{hA}^{\text{ela}}(\vec{b})$ in \vec{b} -space and taking the real part (Eq. (8.7)).

Production and diffractive cross sections can be calculated from the sum of elastic and quasi elastic cross sections (Eq. (8.11) and Eq. (8.15)), using Γ and Γ^* . The integrand in $\sigma_{\text{ela}} + \sigma_{\text{q.ela}}$

contains the expression $|\Gamma^{(*)}|^2$ which is of the form $|1 - z_+ - z_-|^2$ for elastic scattering and in case of diffractive scattering it is $|z_+ - z_-|^2$, with z_{\pm} defined as

$$z_{\pm} = \frac{1}{2} \prod_{j=1}^A [1 - (1 \pm \lambda) \Gamma_{hN}^j] . \quad (8.27)$$

Using $|z_+ - z_-|^2 = |z_+|^2 + |z_-|^2 + 2\text{Re}\{z_+ \bar{z}_-\}$ and the definition [101]

$$\int |z_{\pm}|^2 \prod_j [\rho_j d^3 \vec{r}_j] = \frac{1}{4} \tilde{\Omega}(\vec{b})|_{(1 \pm \lambda)} \quad (8.28)$$

the quasi elastic cross section in case of diffraction dissociation can be rewritten as

$$\begin{aligned} \sigma_{hA}^{\text{SD,ela}} + \sigma_{hA}^{\text{SD,q.ela}} &= \int \left[\frac{1}{4} \tilde{\Omega}(\vec{b})|_{(1+\lambda)} + \frac{1}{4} \tilde{\Omega}(\vec{b})|_{(1-\lambda)} \right] d^2 \vec{b} \\ &\quad - \frac{1}{2} \int \text{Re} \left\{ \prod_j [1 - (1 + \lambda) \Gamma^j - (1 - \lambda) \bar{\Gamma}^j] \right. \\ &\quad \left. + (1 + \lambda)(1 - \lambda) \Gamma^j \bar{\Gamma}^j \right\} \prod_j [\rho_j d^3 \vec{r}_j] d^2 \vec{b} , \end{aligned} \quad (8.29)$$

where $\bar{\Gamma}^j$ denotes the complex conjugate of the amplitude $\Gamma_{hN}(\vec{b} - \vec{s}_j)$. The functions $\tilde{\Omega}$ can be reduced to products of $G_{s,p}(\vec{b})$ similar to Eq. (8.24) using $|1 - z|^2 = 1 - 2\text{Re}\{z\} + |z|^2$

$$\tilde{\Omega}(\vec{b}) = \left(1 - 2G_s(\vec{b}) + \Omega_s(\vec{b})\right)^4 \left(1 - 2G_p(\vec{b}) + \Omega_p(\vec{b})\right)^{A-4} , \quad (8.30)$$

with

$$\Omega_{s,p}(\vec{b}) = \int |\Gamma_{hN}(\vec{b} - \vec{s}_j)|^2 \rho_{s,p}(\vec{r}_j) d^3 \vec{r}_j . \quad (8.31)$$

These expressions were chosen such that the similarity with the previously derived σ_{tot} and $\sigma_{hA}^{\text{ela}} + \sigma_{hA}^{\text{q.ela}}$ (omitted here for brevity) are maximal [101]. Effectively, the implementation only has to be extended by the third term in Eq. (8.24).

8.2.3 Numerical results

The results of the implementation can be seen in Fig. 8.1. The calculation uses Goulianos' parameterization with $\zeta = 0.02$ for the diffractive cross section [102] (shown in Fig. 8.1 on the left) and the fit to the elastic cross section from the Review of Particle Physics [16] to define the energy dependence of the effective resonance coupling

$$\lambda^2(s) = \frac{\sigma_{\text{pp}}^{\text{SD}}}{2\sigma_{\text{pp}}^{\text{ela}}} . \quad (8.32)$$

The final result is shown on the right in Fig. 8.1. The analytical result is shown as a solid line, with both, the elastic and the sum of elastic and quasi elastic contributions, separated. The sampled cross section is represented by the broken lines. The new calculation including intermediate states in SIBYLL 2.3 yields a much higher cross section for diffractive events. Compared to the production cross section in proton air collisions (see Fig. 8.3), it is still very small, so the difference for air shower simulations from the cross section alone would be small. The changes in the event generation, presented in the next section, however, result in a larger difference.

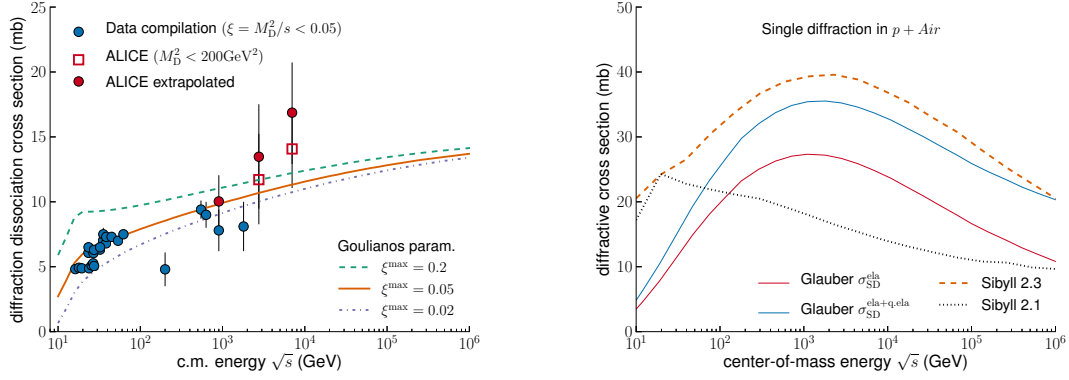


Figure 8.1: Left: Parameterization of the single diffractive cross section by Goulianos [102]. Right: Diffractive cross section in proton air collisions. Results of the numerical calculation are shown as well as the results of the implementation in the MC.

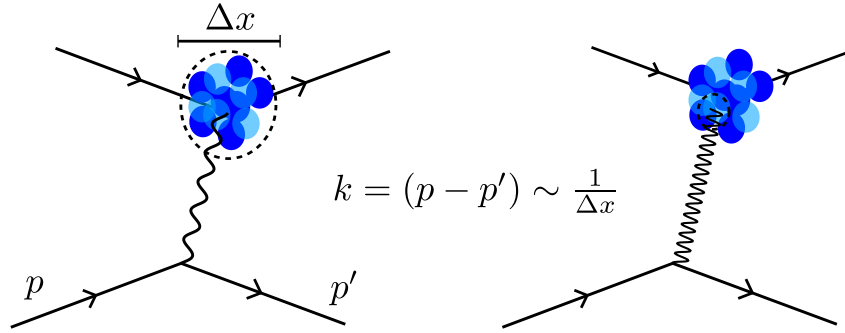


Figure 8.2: Schematic representation of the coherent (left) and incoherent (right) interaction of a hadron with a nucleus. At low momentum transfer the interaction involves the entire nucleus, whereas at high momentum transfers the nucleons participate individually in the interaction.

8.2.4 Event generation

In SIBYLL 2.1, diffractive dissociation of the projectile hadron in a hadron-nucleus interaction occurs only if all the individual nucleon interactions are diffractive. The probability for a diffractive interaction between the hadron and nucleon is determined from the hadron nucleon cross section. If more than one nucleon is participating in the interaction, diffraction is suppressed

$$P_{\text{diff}} = \left(\frac{\sigma_{\text{SD}}}{\sigma_{\text{inel}}} \right)^{N_w} \xrightarrow{N_w \gg 1} 0. \quad (8.33)$$

This implementation corresponds to what is known as *incoherent diffraction*, in that the diffractive interaction really occurs between hadron and single nucleons, not the nucleus as a whole. For low mass diffraction (low momentum transfer, large length scales), the hadron may actually interact coherently with the entire nucleus (see illustration in Fig. 8.2). This *coherent diffraction* corresponds to the calculation presented above. The distinction between low-mass and high-mass diffraction dissociation is arbitrary. Here it is set at $\zeta = 0.02$ (the value used for the definition of $\lambda(s)$)

$$\sigma_{\text{SD}} = \sigma_{\text{SD,l.m}} + \sigma_{\text{SD,h.m}}. \quad (8.34)$$

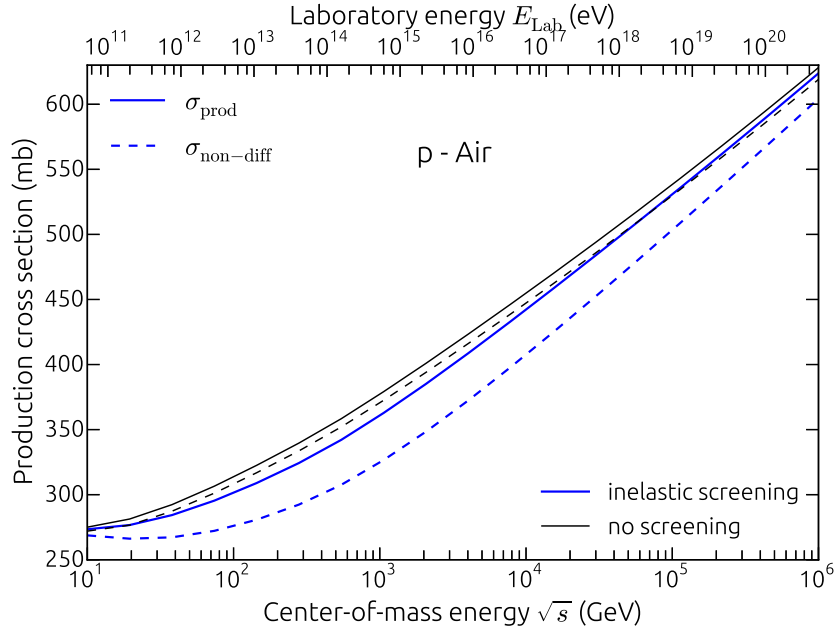


Figure 8.3: Production and non-diffractive cross section in proton air interactions.

With this and assuming the $1/M^2$ distribution of the diff. mass, the low-mass contribution to the total diffractive cross section can be estimated from

$$\begin{aligned}
 f_{\text{l.m.}} &= \frac{\sigma_{\text{SD,l.m.}}}{\sigma_{\text{SD}}} \\
 &= \int_{M_{X,\text{min}}^2}^{\xi_{\text{l.m.}} s} M_X^{-2} dM_X^2 \left(\int_{M_{X,\text{min}}^2}^{\xi_{\text{max}} s} M_X^{-2} dM_X^2 \right)^{-1} \\
 &= \frac{\ln(\xi_{\text{l.m.}} s) - \ln(M_{X,\text{min}}^2)}{\ln(\xi_{\text{max}} s) - \ln(M_{X,\text{min}}^2)}. \tag{8.35}
 \end{aligned}$$

The incoherent contribution is then taken to be the remainder of the diffractive hadron nucleon cross section.

In Fig. 8.4 the selection procedure of low- and high-mass contributions in the model is shown schematically.

In Fig. 8.3 the production cross sections for both schemes are shown. As mentioned before, the difference between the calculation with and without screening in the production cross section is small ($\mathcal{O}(1\%)$). Due to the different treatment of diffraction, the difference between the non-diffractive cross sections in both approaches is much greater ($\mathcal{O}(5 - 10\%)$). While the interaction length that determines shower development, is usually determined from the production cross section, the important process for shower development are the non-diffractive interactions. Diffractive interactions, especially interactions with low excitation masses, that produce only few additional particles, do not contribute to the shower development. The effective interaction length that influences the development, in particular, the position of the shower maximum (X_{max}) in the atmosphere is therefore related to the non-diffractive cross section. The actual effect in simulations are discussed further in Sect. 10.

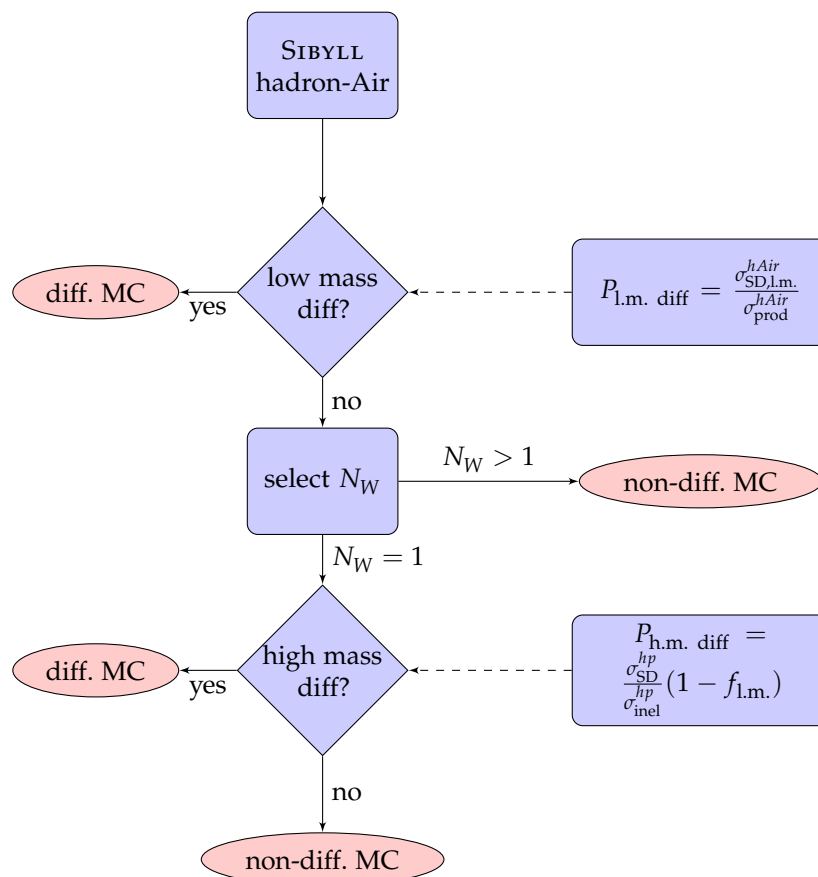


Figure 8.4: Program flow in case of hadron-air collisions in SIBYLL.

Chapter 9

Comparison of the new model with accelerator data

In Sect. 3.4 the performance of SIBYLL 2.1 was discussed and some of the shortcomings were identified. Means of rectifying these issues were subsequently presented as extensions and updates to the model. In this section, the performance of the updated model is demonstrated in comparisons with selected measurements at different energies and in varying beam configurations. Remaining and new problems are discussed as they appear. Some of the figures are produced with the RIVET MC validation and tuning framework [103].

9.1 Fixed target experiments

In general, fixed target experiments cover lower energies than colliders, because the center-of-mass (cm.) energy is proportional to the square root of the beam energy, $\sqrt{s} \simeq \sqrt{2E_{\text{Lab}} m_{\text{nuc}}}$. Therefore, the same technology for acceleration, e.g. the Super Proton Synchrotron (SPS) where $E_{\text{Lab}} = 450 \text{ GeV}$, yields much higher energies for colliding beams ($\sqrt{s} = 900 \text{ GeV}$), since, in that case $\sqrt{s} = E_{\text{beam}} + E_{\text{target}}$. The lower energies in fixed target experiments have the advantage that the phase space for forward particle production is still within the acceptance of the detectors. There are two reasons for this. One is that due to the lower total momentum, a particle with $x_{\text{L}} = 0.9$ will still be produced with a measurable angle with respect to the beam direction. The second reason is that the absence of a beam pipe behind the target, allows the placement of detectors closer to the beam axis. This allows the measurement of the leading particles.

In the left plot in Fig. 9.1 the leading proton spectra in p-p collisions as measured in fixed target experiments at the Fermi National Accelerator Laboratory (FNAL), are shown [104]. The description of these was fine tuned into SIBYLL 2.1, while the more general approach of beam remnants is used in the new model (see discussion of remnant model in Sect. 5). The flatness of the leading proton spectrum is not reproduced as well as in the previous model.

Comparing the spectra at different energies the deviation from the flat spectrum appears to increase with energy (see also the data from HERA at $\sqrt{s} = 200 \text{ GeV}$ in Fig. 9.3-left), which could mean that the remnant mass spectrum does not have the correct energy dependence. In light of the non-trivial sub-structure of the remnant de-excitations (e.g. see Fig. 5.5), the resulting flat spectrum is sufficient for the purposes of the model.

In the left plot in Fig. 9.1 the spectra of positive charged particles C^+ in π^+ , K^+ and p-p collisions with beam momentum $250 \text{ GeV}/c$ [98] are shown. The two peaks in the C^+ -spectrum are from the leading particles ($x_{\text{F}} \rightarrow 1$) and the particles from central production ($x_{\text{F}} \sim 0$). Both models reproduce the spectra for the different beam particles well. In the transition region between non-diffractive and diffractive (diff.) particle production around $x_{\text{F}} = 0.8$, SIBYLL 2.1 produces a discontinuity due to the hard implementation of the diff. mass limit. In the new model, the hard limit is replaced with a smooth transition function (Fermi function).

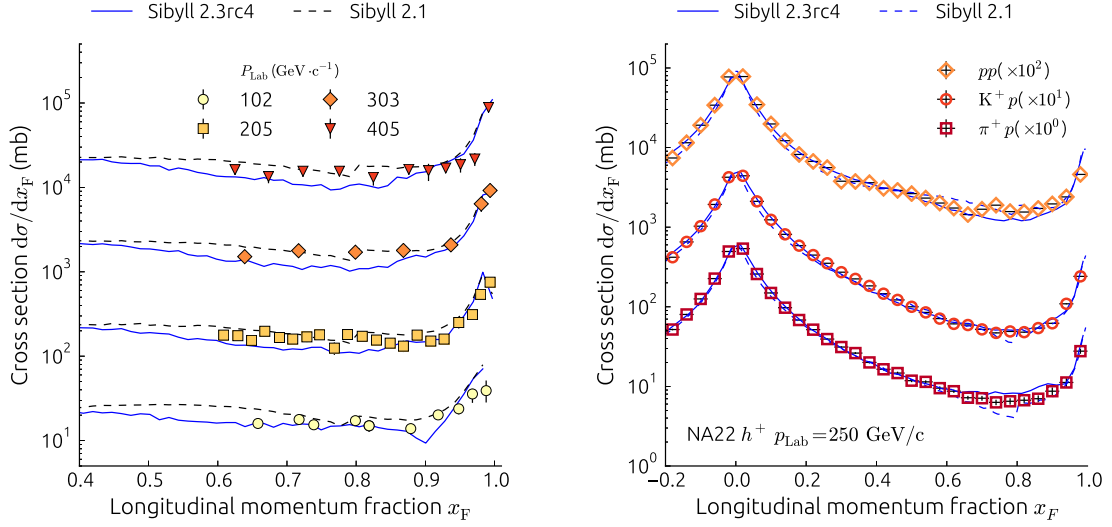


Figure 9.1: Left: Bubble chamber measurements of leading proton spectra at low energy [104]. Both the leading string (SIBYLL 2.1) and the remnant model (SIBYLL 2.3) reproduce these data. Different beam momenta are depicted, namely 405 ($\times 10^4$), 303 ($\times 10^3$), 205 ($\times 10^2$) and 102 GeV/c ($\times 10$). Right: Comparison of different leading particles. From top to bottom: protons ($\times 100$), kaons ($\times 10$) and pions ($\times 1$) for collisions with $p_{\text{Lab}} = 250$ GeV/c [98].

For leading pions (red squares), overlap between remnant dissociation and diff. dissociation in the new model produces a structure in the spectrum that is not present in the data. This is consistent with the overestimation of the production of leading ρ^+ -resonances ($\rho^+ \rightarrow \pi^+ + \pi^0$) encountered earlier (Fig. 7.4 in Sect. 7.2). It might be repaired by allowing the formation and decay of heavy pion resonances $\pi(1300) \rightarrow \rho + \pi$ in the remnant excitation. Similar to the behavior of nucleon resonances described in Sect. 5, heavy pions prefer the decay channel where the ρ is in the charge opposite state, i.e. $\rho^0 + \pi^+ : \rho^+ + \pi^0 = 2 : 1$. In the current model only ρ -resonances are formed in the remnant excitation, and charge exchange ($\pi^+ \rightarrow \rho^0$) can only occur if one of the sea quarks is exchanged with a valence quark in the remnant.

One measurement of the leading particles at higher energy is the proton spectrum measured in deep inelastic scattering at HERA [105] as shown in Fig. 9.3. SIBYLL does not include a model of hadronic photon interactions, but the proton dissociation shown here is universal. The kinematic of $\gamma^* + p \rightarrow p + X$ corresponds to pp collisions in SIBYLL with $\sqrt{s} \sim 200$ GeV. As an illustration of the problems with the transition between non-diff. (remnant) and diff. regions encountered before, the contributions to the spectrum from the different components are also shown. Judging from these, the forward proton peak could be sharpened by increasing the momentum fraction of the sea quark pair which is sampled along with the remnant. This would limit the maximal fraction of the total momentum assigned to the remnant and the overlap between diff. and non-diff. components would decrease, making the peak more narrow. The plateau

In Fig. 9.2, the double differential spectra of charged pions in $\pi^- C$ collisions are shown as functions of the total momentum in the lab. frame. Different intervals in transverse momentum are scaled with powers of ten starting with 10^0 for the interval with the largest p_{\perp} . The data shown are the preliminary results from a measurement in the NA61 fixed target experiment with a $p_{\text{Lab}} = 158$ GeV beam of negatively charged pions [96].

The maximal momentum shown here corresponds to $x_L = 0.28$. In the intervals with transverse momentum below 0.5 GeV, this translates to a Feynman- x (momentum fraction in cm. frame) of the same order. Beyond that, the corrections in the m_T/E expansion of x_L are large so the correspondence (Eq. 2.7) is not trivial anymore. In the p_{\perp} -interval between 1.58 GeV/c and 2 GeV/c, the first order corrections are -0.18 and -0.32 , meaning that x_F is maximally 0.02 and

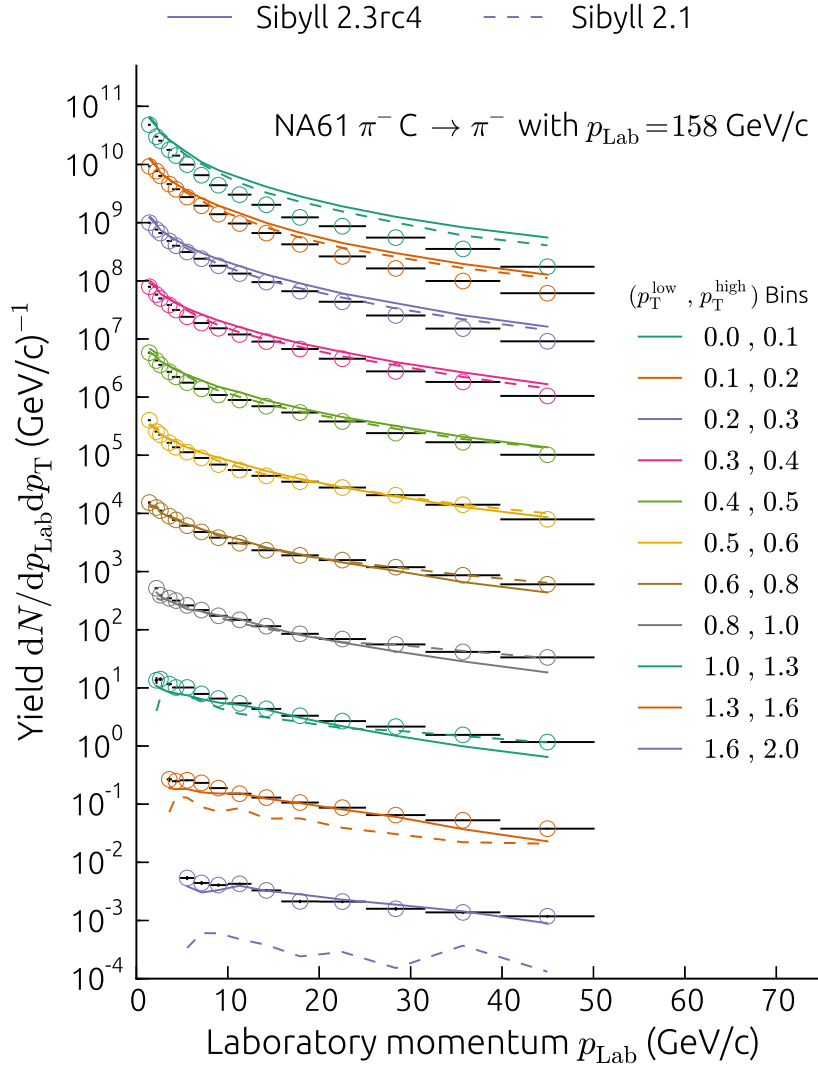


Figure 9.2: Double differential spectrum of π^- produced in π^- C collisions measured in the NA61 experiment [96]. The range in lab. momentum p_{Lab} shown here corresponds to the central and backward fragmentation region in the cm. frame (see discussion in text).

minimally -1 . This exercise shows that at these low lab. momenta, the data contain contributions from the central region ($x_F \sim 0$) and the backward fragmentation region ($x_F \lesssim -0.5$).

The interesting region for air showers is the forward fragmentation region where currently no data from NA61 are available. In the central region, which appears in the low p_{\perp} intervals in Fig. 9.2, the spectrum appears to be slightly too hard in both models, and the overall multiplicity is too large. This could be accompanied by an underestimation of the production in the forward region, which could have a large effect in air shower simulations. In light of the general scarcity of data on π -nuclear interactions, an extension of the x_F range of the measurement would be very helpful.

Completing the discussion of NA49 data, the spectra of charged kaons are shown in Fig. 9.3 [106]. The difference between the spectra of K^+ and K^- is a direct consequence of the quark content of the proton. $K^+ : u\bar{s}$ can be produced from the proton with a single additional $s\bar{s}$ -pair, while for $K^- : s\bar{u}$, at least two pairs are needed. K^- can therefore only be produced inside the hadron chain (not the end), where the assigned momentum fractions are smaller (hadron chains are ordered in rapidity, see Sect. 3.3.1). The only chance for production at the

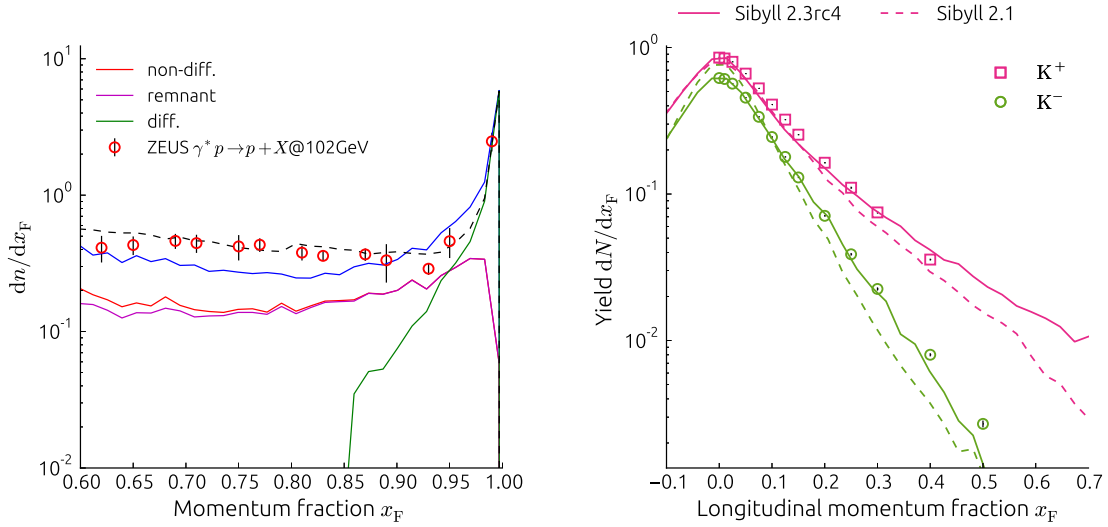


Figure 9.3: Left: Leading proton spectrum in deep inelastic scattering at HERA [105]. The photon proton interaction is approximated with $\sqrt{s} = 200$ GeV pp interactions in SIBYLL. Contributions to the spectrum in the model by diffractive and non-diffractive interactions are shown. For non-diff. events the remnant contribution is shown as well. Right: Kaon spectra in NA49 [106]. Note that for SIBYLL 2.1 the central production of positive and negative kaons is identical, while the data still show more positive kaons. With the remnant model the ratio between the charges is reproduced more accurately.

string end (in pp collisions) is in strings between sea quarks, which naturally carry only small momentum fractions. The same arguments hold for \bar{p} -production, and therefore, the spectra are very similar (see Fig. 5.1).

The other side of the process behind the production of leading K^+ can be seen in the measurement of Λ hyperon production in pion proton and kaon proton interactions as shown in Fig. 9.4 [107]. The reaction is called *associated production* and in this case it corresponds to the insertion of a $s\bar{s}$ pair into the proton, which will produce a Λ and a K^+ . The fragmentation region of the proton in the interactions shown is in the backward hemisphere ($x_F < -0.5$). In case of the pion projectile, Λ production is strongly asymmetric between the hemispheres and between particle and antiparticle. This is because the Λ is only weakly related to the pion, as is the $\bar{\Lambda}$. On the proton side Λ is strongly favored over $\bar{\Lambda}$.

The $\bar{\Lambda}$ -spectrum is slightly asymmetric between forward and backward hemisphere because mesons contain an antiquark, while for protons, the only antiquarks appear as fluctuations. Not surprisingly, the $\bar{\Lambda}$ -spectrum is the steepest. It is similar to the \bar{p} spectrum in NA49 (see Fig. 5.1).

For the kaon projectile, the initial state already contains the \bar{s} needed to form the $\bar{\Lambda}$, so production is enhanced.

Because Λ -hyperons are heavier than protons, the correlation between leading particles (Λ) and central production ($\bar{\Lambda}$) due to energy conservation that is present in the leading string model in SIBYLL 2.1 is therefore even stronger. The description of the data by that model is correspondingly poor. In the new model, the strong link between fragmentation region and central region is broken by the introduction of projectile remnants. SIBYLL 2.3 is thus capable of reproducing all the aspects and correlations of hyperon production in NA22.

9.2 Large Hadron Collider

When moving from low energy interactions to the highest energies currently achievable in the laboratory, the processes that determine particle production change dramatically. In the low energy region, typically only a single pair of partons scatter and the dissociation of the beam remnants constitutes the largest contributor to particle production. Beyond 1 TeV cm. energy, multiple hard parton interactions are common (see Fig. 9.13-right).

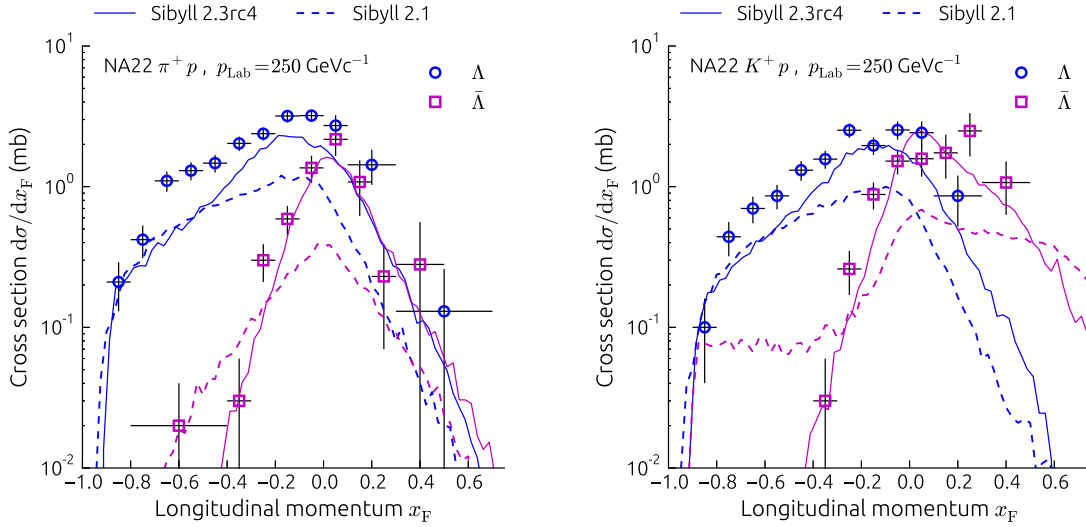


Figure 9.4: Λ -hyperon production in meson proton collisions measured in the NA22 experiment [107]. Projectiles are π^+ (left) and K^+ (right). Note the leading $\bar{\Lambda}$ at large x_F produced from the \bar{s} quark in the K^+ projectile. For π^+ p collisions, only the Λ has a leading contribution. Due to the hard leading fragmentation function, SIBYLL 2.1 has problems reproducing central production. In the remnant model, the energy sharing between central and fragmentation region is more flexible.

The phase space covered by experiments is very different as well. High energies are reached most efficiently in head on collisions. This means that along the beam axis (small angles) no detectors can be placed because the space is occupied by the accelerator (see gap in η -coverage between 5 and 8 in Fig. 2.4). Forward measurements are therefore difficult. A typical detector at a collider is the *Compact Muon Solenoid* (CMS) [108] at the *Large Hadron Collider* (LHC). It is a central detector that roughly covers the region $|\eta| < 2.5$ with several additional components that extend this range.

9.2.1 Central particle production

The measurement of the spectrum of transverse momentum of charged particles and the individual spectra of pions, kaons and protons have been shown before in Sect. 7. To summarize central particle production, the distribution of charged particles in rapidity is shown in Fig. 9.5 on the left. The measurement is done by combining the forward detectors from TOTEM [110] with the central detector from CMS, so that the two regions $|\eta| < 2.5$ and $5 < \eta < 8$ are covered [109].

From the model perspective, the height of the central plateau depends on all aspects of particle production, from the number of parton interactions to the fragmentation function. In SIBYLL, the shape of the pseudorapidity distribution of individual parton interactions (minijets) does not change. This is the case because the fragmentation of all minijets is implemented as a pair of strings. The kinematic of the minijets only changes the extent and position of the strings in rapidity

$$\Delta y \sim \ln \hat{s} \quad , \quad y \rightarrow y + y_{\text{boost}}^{\text{parton} \rightarrow \text{hadron}} \quad . \quad (9.1)$$

The height of the plateau is then determined by the number of strings and the particle yield per string (see Fig 9.6). The model can then be adjusted to describe the plateau height by varying one of the two.

The fall-off towards large rapidities is determined by the shape of the combined distribution of the momentum fractions in minijets (x_1, x_2) in the region where one of the x_i is large (y_{boost} large). If the underlying pseudorapidity distribution of the strings is too steep, reproducing the fall-off becomes difficult. This seems to be the case in the SIBYLL models. As shown in Fig. 9.5, both models can describe the central plateau very well (see also Fig. 3.6) but fail to reproduce the behavior at large η .

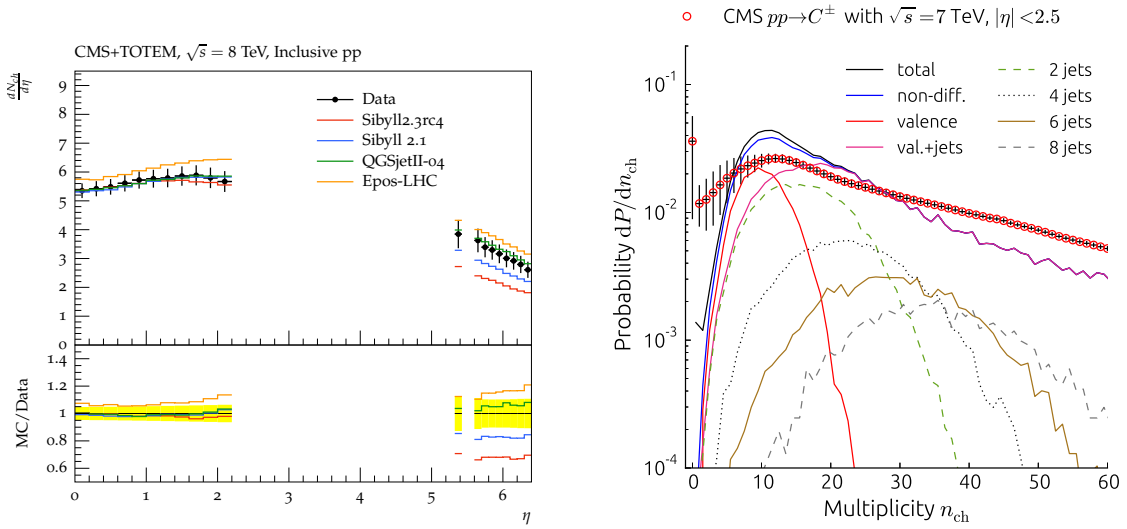


Figure 9.5: Left: Central charged particle production in CMS and TOTEM [109] compared to the predictions by the CR interaction models EPOS-LHC, QGSJET II-04 and SIBYLL. Both SIBYLL models predict a narrower distribution in η than the other models, which is in contradiction with the data. The plot was created using the Rivet analysis framework [103]. Right: Charged particle multiplicity in CMS [56]. The breakdown into different contributions shows that events with large multiplicity are the consequence of multiple parton interactions. The ‘valence’ contribution denotes events with a single parton interaction.

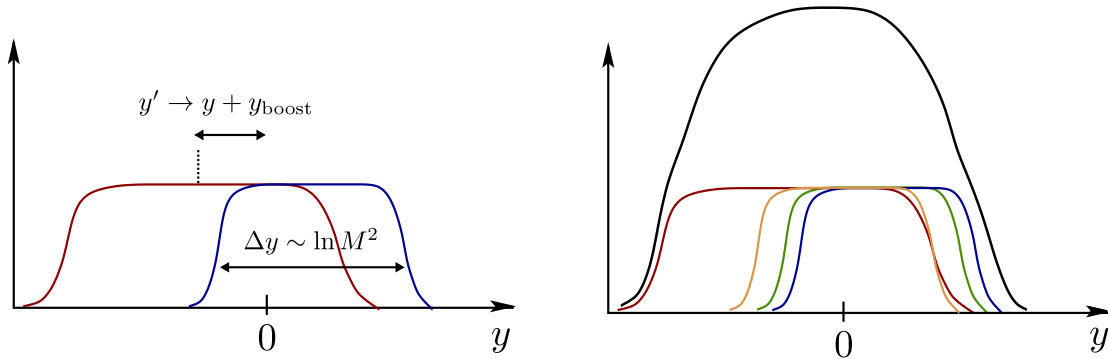


Figure 9.6: Left: String width and position in rapidity is determined by parton kinematic. Right: Overlap of multiple strings produces the central rapidity plateau.

It was investigated whether varying the kinematic of the minijets within certain bounds could increase the width of the η -distribution, but the desired results were not achieved. The problem could possibly be solved by abandoning the simplified two string configuration for the minijets (see Fig. 3.4) in favor of a more complex construct. This configuration is certainly one of the differences to the other CR- and the HEP models, which do not seem to have similar problems. The approach is particularly attractive because it would not challenge the principal interaction picture. It would only change the pseudorapidity distribution of the individual interactions.

The approximation introduced in the two-string minijets is that there is no color connection between the interacting partons and the parent hadrons (Sect. 3.2), which turns the minijet into a string loop. This could be extended by replacing the two strings between gluons with strings between quark-gluon-antiquark, where the quark and antiquark would be fluctuations in the hadron. The gluon in this case would undergo the same scattering as before.

In Fig. 9.5 on the right, the distribution of the charged multiplicity in *minimum bias* events, i.e. events that were recorded without requiring the signature of some specific process (usually large

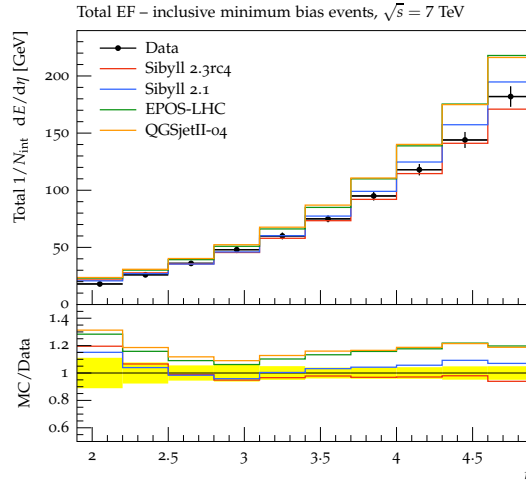


Figure 9.7: Energy flow of charged particles in LHCb [111].

p_{\perp}), is shown. To illustrate the influence on particle production, the contributions of different numbers of parton interactions to the multiplicity distribution are also shown.

The problem with the tail at large multiplicities has already been discussed as one of the shortcomings of SIBYLL 2.1 (Sect. 3.4). As mentioned before, the solution is probably the introduction of an impact parameter dependent saturation model. The figure shows that the tail at large multiplicities is formed by collisions with many interactions. Many parton interactions are most likely to occur in events with a central collision (small impact parameter, large overlap of hadron profiles), which also so means saturation is more likely to occur in these collisions. Currently, saturation is included by reducing the hard interaction cross section as a function of the energy, which will reduce the average number of interactions but will not change the relative rate of events with different numbers of interactions.

Reducing the number of interactions per event leaves more energy for the remaining interactions and therefore strings. Since the string mass determines the width of the distribution of the final state particles in pseudorapidity, an extended saturation model could help increasing the width of the total distribution in η . However, the tail in the multiplicity distribution corresponds to very rare events, while the pseudorapidity distribution represents the average event. It is therefore very unlikely that an extended saturation model alone can repair this.

The problem that occurs with reproducing the lowest multiplicities in Fig. 9.5-right is probably due to the wrong implementation of the selection for the event sample the multiplicity distribution is constructed from, leading to a misrepresentation of diffractive events in the sample. The prescription used in the experiment is to accept all events with a certain energy deposit in both forward hadron calorimeters outside the central detector (HF acceptance: $2.9 < |\eta| < 5.2$), thereby selecting predominantly non-diff. and double diff. events (so-called *non-single diffractive* (NSD) selection) [56]. The multiplicity is then determined from the number of tracks in the central detector in the range $|\eta| < 2.4$. Due to the central rapidity gap, double diffractive events make up the largest contribution at low multiplicities. The underestimation of low multiplicities in the figure suggests that the diffractive events fail to pass the initial threshold in energy deposit.

9.2.2 Forward phase space

Measuring forward particle production is particularly hard for charged particles, which are deflected in the magnetic field of the accelerator. The fact that neutral particles are not deflected, is used in a number of very forward (zero degree) calorimeters at LHC, for example, LHCf [112]. By placing a small detector between the two beam pipes (pp collider), neutral particle production at zero degrees can be measured.

The detector with particle identification capability and the most forward coverage is LHCb [113]. Its measurements typically cover the rapidity region $2.5 < y < 4.5$. In Fig. 9.7, on

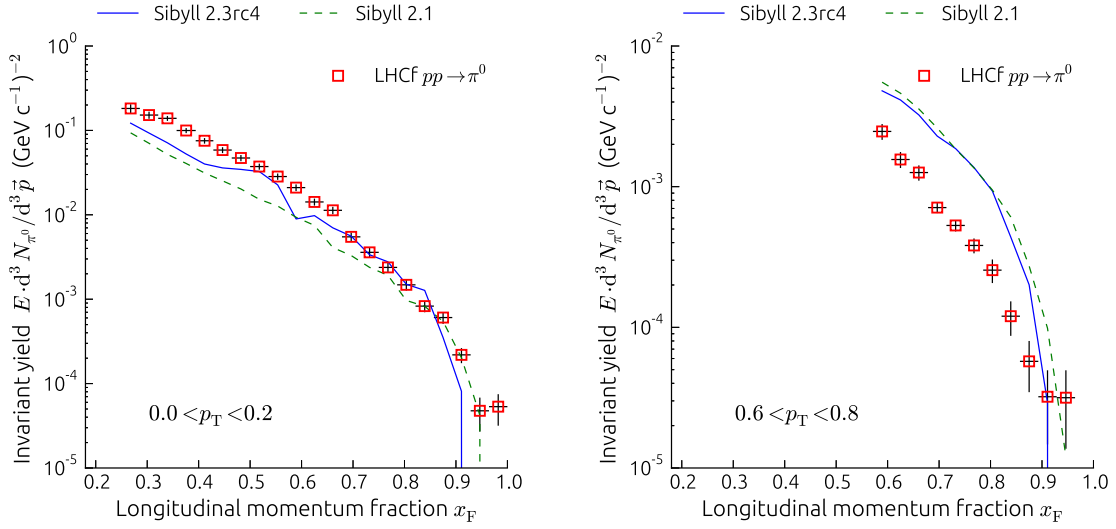


Figure 9.8: Invariant Feynman- x spectrum of neutral pions measured in the LHCf calorimeter [114]. Low- p_{\perp} is shown on the left, higher p_{\perp} on the right. The shape of the spectrum in x_F is reproduced equally well in both version of the model. The normalization is too low for low- p_{\perp} and too high in the high- p_{\perp} region, which would suggest that the distribution in transverse momentum is too hard. In the p_{\perp} -bins between these shown here, production is also overestimated.

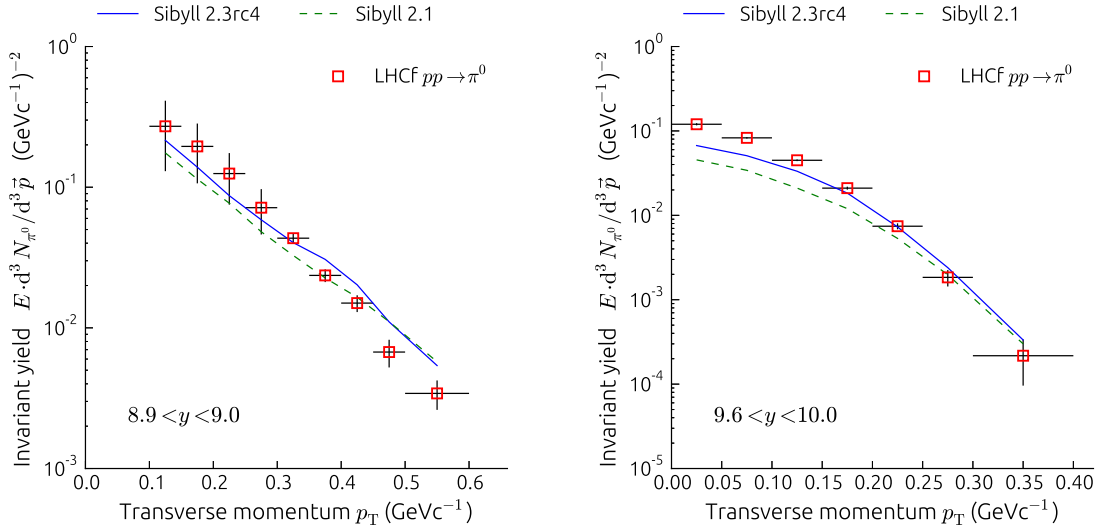


Figure 9.9: Invariant transverse momentum spectrum of neutral pions measured in the LHCf calorimeter [114].

the left, the measurement of the energy carried by charged particles in this region is shown [111]. Comparison with to the total energy flow (Fig. 2.4) suggests that the bulk of the energy is carried by particles outside the detector acceptance. Only the rise of the forward peak is covered by the experiment.

The excellent description of the energy flow by the SIBYLL models makes the problem with describing $dN/d\eta$ less severe, because the energy flow not the multiplicity is what primarily dictates the development of air showers. Since the pseudorapidity is equivalent to the scattering angle, the narrow distribution could have an effect on the lateral distribution of particles at ground.

Moving forward in η , only the neutral particle calorimeter LHCf remains. In Fig. 9.8, the invariant spectrum of neutral pions in LHCf is shown [114]. The performance of the SIBYLL

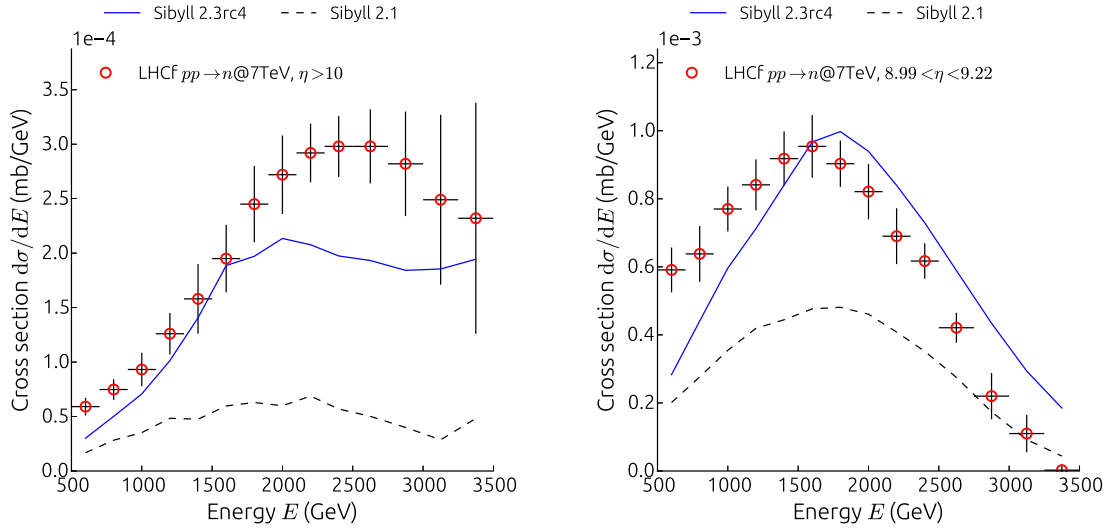


Figure 9.10: Energy spectrum of neutrons in the very forward region as measured at $\sqrt{s} = 7\text{ TeV}$ by LHCf [115]. Shown are the spectra in the two calorimeters corresponding to $\eta > 10$ (left) and $8.99 < \eta < 9.22$ (right) in pseudorapidity. In both cases the remnant model performs much better than SIBYLL 2.1.

models in this range is very similar, which is not trivial given the different treatment of the leading particles. Both models show an overestimation of the number of neutral pions at large x_F in the high- p_\perp range. In combination with the underestimation in the low- p_\perp range, this suggests that the transverse momentum spectrum is too large which is confirmed by Fig. 9.9.

The energy spectrum of neutrons in the very forward region is shown in Fig. 9.10. The measurement includes angles of zero degrees, or ∞ in pseudorapidity, which is in contrast with the measurements of neutral pions shown earlier. The difference is that the neutral pions are not detected directly ($c\tau_0 \approx 25\text{ nm}$) but have to be reconstructed from the two photons. Compared to SIBYLL 2.1, the spectrum is better reproduced by the new model including remnant formation, which is encouraging since the remnant model was not tuned to these data. Comparing the two calorimeters that cover different regions in pseudorapidity (angles), it seems, that the transverse momentum of the neutrons is too high, as already observed in the case of the neutral pions. Large transverse momenta would cause the neutrons to migrate from the small angle bin into the large angle bin.

9.3 Extrapolation

One of the important features that distinguishes CR interaction models from HEP models like PYTHIA or HERWIG is the reliability of the extrapolation to high energy. This does not mean that the models necessarily give the correct prediction for any distribution at high energy. It means that the models are structured such that the individual components are not entirely independent so that the parameters at low energy are connected to the parameters at high energy. This starts at the parton level, where the requirement of unitarity, in principle, connects cross sections for different processes (Sect. 3.1) and ends at the hadron level with universal string fragmentation.

Often the connection can only be established by introducing an arbitrary energy dependence of the parameters.

In practice, a primary difference between CR and HEP models lies in how the models are tuned to new data. Each time a new highest energy is reached in accelerator measurements, CR models are retuned at all energies, while HEP models are retuned to that energy. Retuning includes extending the model by new processes if necessary. As a result, individual data sets are better described by the tuned HEP models, while the CR models work better on average.

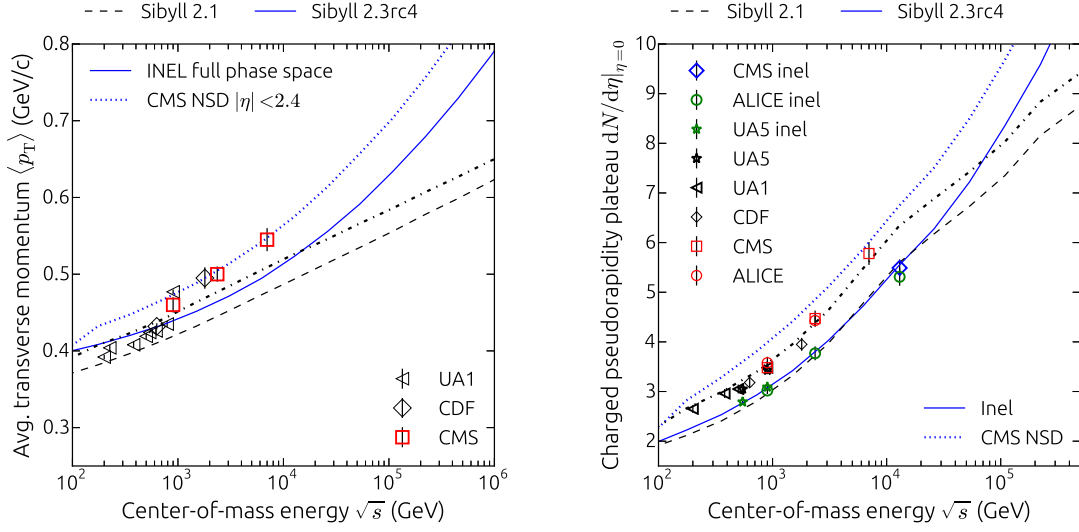


Figure 9.11: Left: Average transverse momentum of charged particles as a function of cm. energy. Two event selections (NSD,INEL) and phase space regions (central,full) are shown. In black are the pre-LHC measurements by CDF [116] and UA1 [117], in red the measurements by CMS [70]. The change in the energy dependence is due to a different parameterization of the average string- p_{\perp} and the correction of the transverse momentum cutoff of the hard interactions. Right: Average charged pseudorapidity density in inelastic and non-single diffractive events. The problem with the width of the pseudorapidity distribution in the NSD sample is evident. The change in the slope at high energy for SIBYLL 2.1 is due to the technical limitation of the number of interactions.

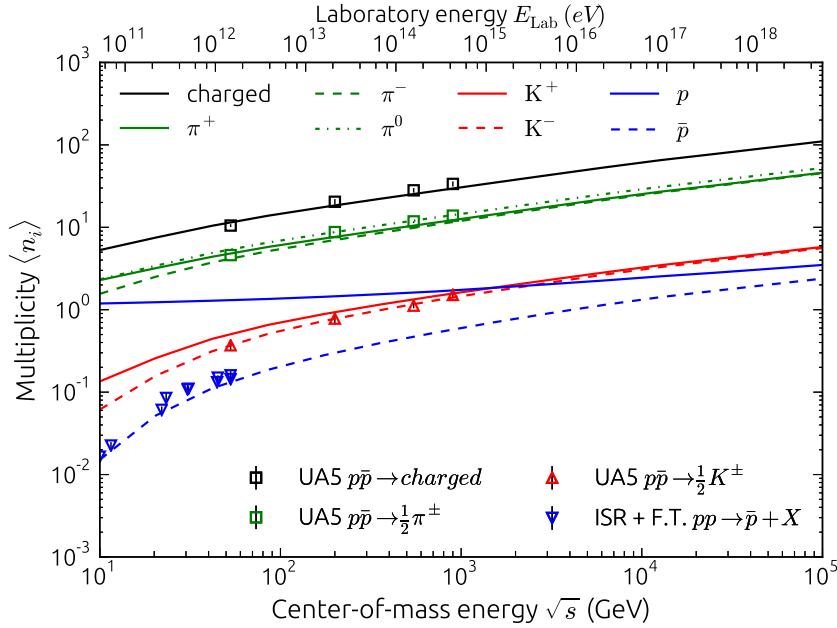


Figure 9.12: Particle multiplicities in pp collisions as a function of cm. energy in SIBYLL 2.3. The all charged, pion and kaon measurements are from UA5 [118]. The antiproton data are a compilation of fixed target experiments [89].

Asymptotically, the CR models, will approach the correct description at all energies (excluding unification and effects from non-hadronic interactions).

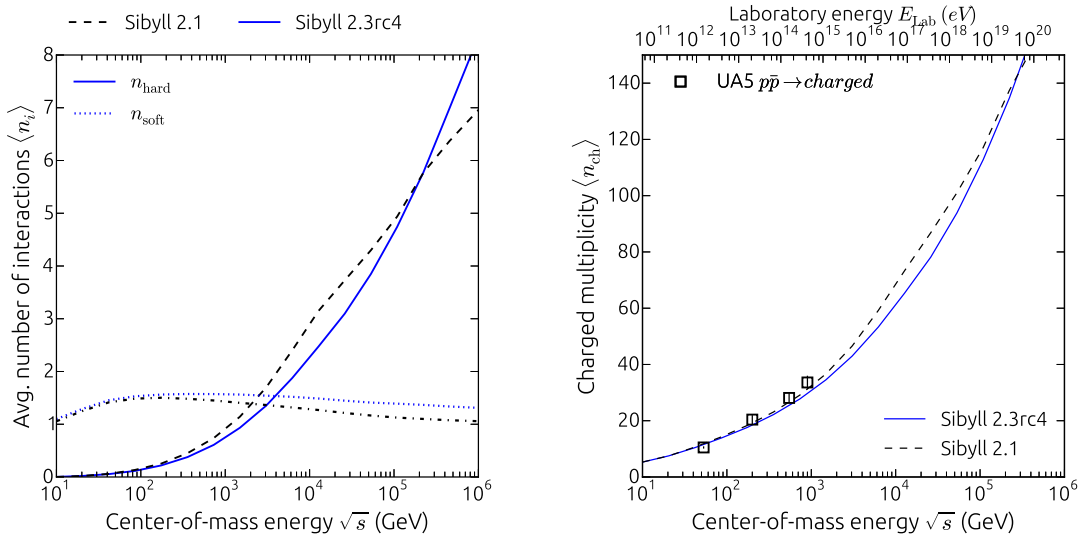


Figure 9.13: Particle production and parton interactions. Particle production at low energy in SIBYLL is dominated by soft interactions, which includes valence strings (2.1) and remnants (2.3). The energy range of the LHC is the first where particle production becomes dominated by multiple hard interactions. Note how the structures in the number of parton interactions due to technical limitations in SIBYLL 2.1 (left) are reflected in the number of final state particles (right). Due to the lower cross section, which was achieved by reducing the width of the proton profile (see Sect. 4.1), SIBYLL 2.3 predicts slightly fewer hard parton interactions.

The current version of SIBYLL (rc4) is improved in many aspects (previous sections), but the comparison with LHC data also revealed some problems. These are reflected in the extrapolation to high energy.

In the left plot in Fig. 9.11, the average transverse momentum as a function of the cm. energy is shown. As part of the transition from the Gaussian- p_{\perp} distribution to an exponential distribution in transverse mass (Sect. 7.3), the energy dependency of the average transverse momentum in string fragmentation was changed from linear in $\ln(s)$ to quadratic. This change was motivated by the new high energy data. Until the TeVatron the data could still be interpreted as rising linearly. Some of the increase in $\langle p_{\perp} \rangle$ also comes from the repaired p_{\perp} -cut in the hard cross section.

The right plot in Fig. 9.11 shows the pseudorapidity plateau as a function of the energy. The problem with the narrow distribution discussed earlier is hidden in SIBYLL 2.1 due to the different implementation of the p_{\perp} -cut. For the new model, this results in the overestimation of the plateau at lower energies. The break in the rise seen for SIBYLL 2.1 at high energy is due to the technical limitation of the number of interactions in the program code ($n_s^{\text{max}} = 20$, $n_h^{\text{max}} = 50$). These breaks reduce the reliability of the extrapolation because they break the connection between low and high energy parameters.

Fig. 9.12 depicts the average multiplicities of the most common hadrons for SIBYLL 2.3. It shows that the multiplicity, considering the general trend, is slightly overestimated for kaons and underestimated for pions at high energy. As a result, the charged multiplicity is probably underestimated at high energy as well. This is compatible with the observation of the narrow pseudorapidity distribution at LHC and will resurface in the discussion of $\langle X_{\text{max}} \rangle$ in the next chapter.

The connection between the number of parton-parton interactions in an event and the number of particles produced, which was already discussed in the context of the multiplicity distribution measured in CMS (Fig. 9.5), is shown in Fig. 9.13. The dominant process for particle production at high energy is hard scattering. The soft interactions dominate at low energy. In SIBYLL 2.1, the number of soft interactions is ≥ 1 , because the valence quarks are assumed to always interact softly. In SIBYLL 2.3, this behavior is kept, although it is not necessary anymore since the valence flavors are treated independently in the remnant.

The break in the number of hard interactions for SIBYLL 2.1 in Fig. 9.13 is again due to the limitation of the number of interactions. In light of the removal of technical problems such as these, the extrapolation in SIBYLL 2.3 is more reliable. As to the accuracy of the prediction, the data from LHC Run II will be available for judgment soon.

Chapter 10

Predictions for cosmic ray interactions

The comparison of the interaction model with accelerator data that was presented in the previous chapter, while revealing several shortcomings, is not a complete gauge of the performance of the model. Since the model is explicitly designed for cosmic ray interactions, the final measure of performance is whether cosmic ray measurements are described consistently.

There are two scenarios in which our understanding of hadronic interactions, represented by the model, can be tested using cosmic ray and air shower measurements. One is the direct measurement of an observable of hadronic interactions. An example of this is the extraction of the proton-proton cross section from air shower measurements mentioned in the discussion of the new cross section in SIBYLL in Sect. 4.1. The measurement of the proton-air cross section is shown in the next section in Fig. 10.1.

The second scenario is to check whether the interpretation of different air shower observables in terms of the properties of the primary particle is consistent or rather inconsistent. One example for this is the 'muon problem' introduced in the first chapter. It will be discussed further in Sect. 10.1. Other examples are the spectrum and charge ratio of atmospheric muons. They will be discussed in Sect. 10.2

The predictions for air showers shown here were calculated using CONEX [26], a computer program that integrates the cascade equations for single air showers from an interpolation table of hadronic interactions.

Some of the discussion in this chapter has been presented in the proceedings to the workshop for elastic and diffractive scattering [119].

10.1 Extensive air showers

10.1.1 Depth of shower maximum

As it was mentioned in Sect. 2.3, the position of maximal development of an air shower in the atmosphere (X_{\max}) depends mostly on the first few interactions. This can be used to determine the interaction length of the primary particle and therefore the proton-air cross section directly from air shower measurements. In Fig. 10.1-left the cross section in proton-air interactions predicted by SIBYLL is compared with the measurement at the Pierre Auger Observatory [63]. The new model is well compatible with the data. The old model, that was tuned to TeVatron data, the cross section at high energy is overestimated.

Turning the previous argument of the dependency of X_{\max} around, the new, lower value of the proton-air cross section predicted by the model, which corresponds to an increased interaction length of the primary particle in the atmosphere, will shift the position of shower maximum to

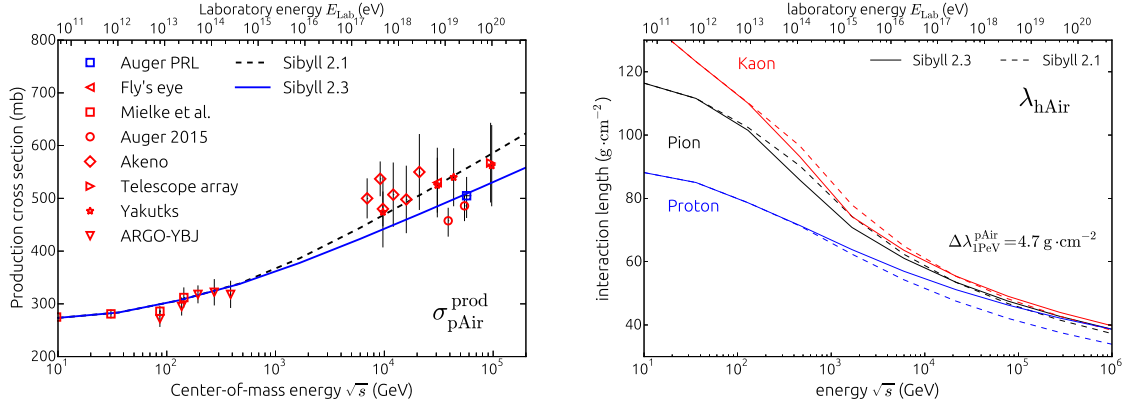


Figure 10.1: Left: Proton-air cross section in SIBYLL compared to measurements based on air shower observations [120, 121, 122, 123, 124, 125, 126, 127]. The prediction by SIBYLL 2.1 is incompatible with the measurement by the Pierre Auger Observatory [63]. Right: Interaction length of protons, pions and kaons in air as predicted by the different versions of SIBYLL.

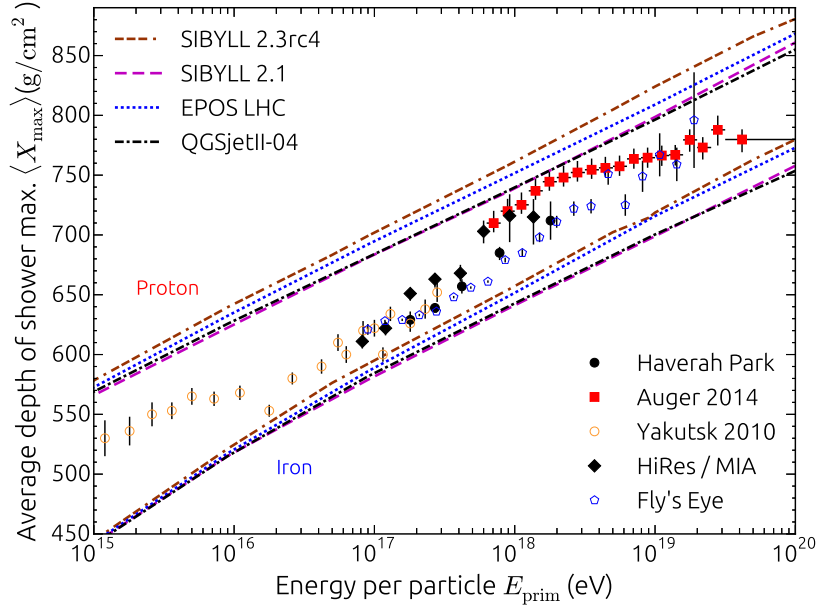


Figure 10.2: Average depth of shower maximum as a function of the primary energy. Comparing model predictions for proton and iron showers and measurement indicates multiple changes in the composition from heavy to light in the energy range from 1 PeV to 10 EeV [128, 129, 130, 131, 132].

larger depth. The actual effect of the cross section on the interaction length is shown in Fig. 10.1 on the right. Since the cross section appears in the denominator of the interaction length

$$\lambda_{\text{int}} = \frac{A m}{\sigma_{\text{air}}}, \quad (10.1)$$

and the relative change is small, the effect on the interaction length is almost negligible. It amounts to 5 g/cm^2 at 10 EeV. In Fig. 10.14 the effect on X_{max} is demonstrated by exchanging the values of the interaction length used in the cascade calculation with the values obtained from the old cross section, while keeping all other aspects of the calculation constant. As expected the difference between the model predictions is of the order of a few g/cm^2 only.

The impact on X_{max} when combining all updates and extensions presented before, is shown in Fig. 10.2. Here, the average depth of shower maximum $\langle X_{\text{max}} \rangle$ is shown as a function of the

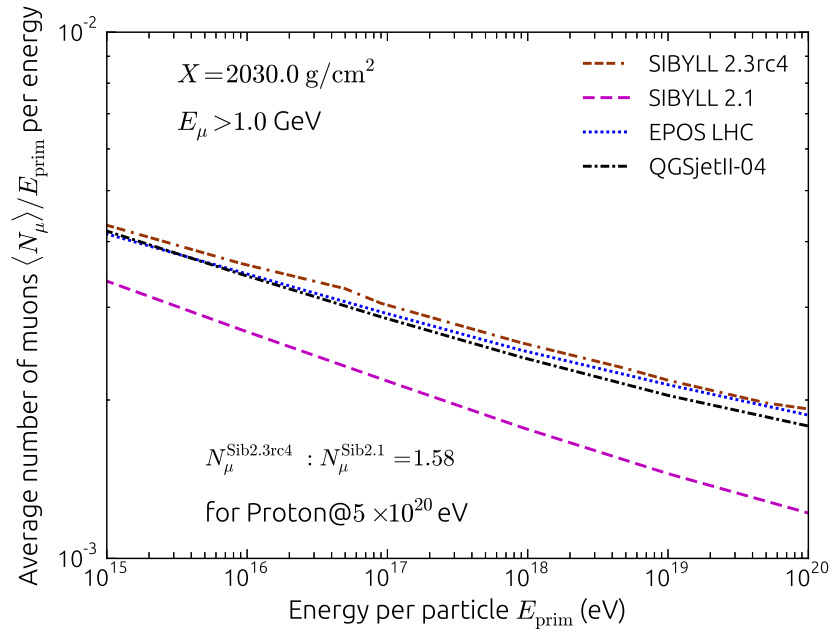


Figure 10.3: Prediction of the number of muons in proton initiated air showers as a function of the primary energy.

energy. As an estimate of the underlying mass composition the prediction for pure composition assuming proton and iron are calculated using a hadronic interaction model and then the measurement is compared to these predictions. While this does not allow the determination of the composition in terms of elemental fractions, it is sufficient to distinguish mixed from pure compositions and determine whether the general tendency is towards increasing or decreasing primary mass.

The measurements of X_{max} in the energy range from 10^{15} eV up to $5 \cdot 10^{19}$ eV [128, 129, 130, 131, 132], indicate that there are several changes from light to heavy composition [133]. According to the elongation rate theorem (Eq. 2.24 in Sect. 2.3), the elongation rate between different primary particles is the same (proton and iron predictions are parallel), which means the composition is constant where ever the data and the model prediction have the same slope. This is important additional information considering the spread between the predictions from different models ($\approx 40 \text{ g/cm}^2$ at 10 EeV). Based on the slope the interpretation of a change in composition may be consistent with the predictions from all models, while the interpretation in terms of masses may be incompatible.

Compared to the previous version of SIBYLL, the predicted shower maximum is much deeper. The new prediction is also much deeper compared to the other models. The elongation rate has increased slightly between the SIBYLL models, which is consistent with the observations made in the discussion of the energy extrapolation in the previous chapter, namely that the multiplicity increases less strong with energy and that Feynman scaling in the fragmentation region is obeyed more closely in the new model.

10.1.2 Number of muons

Many of the extensions to the model discussed in the previous chapters are motivated by the apparent inconsistency of composition measurements based on X_{max} and N_{μ} , that may be explained by a discrepancy between the number of muons in simulations and data (see discussion in Sect. 2.3.3). In principle it is not clear whether the problem is really in the production of muons, but the strong dependency on the interactions of mesons make it a good candidate.

Irrespective of the outcome for muons, baryon and ρ production (Sect. 7) were clearly misrepresented in the model. The prediction for the number of muons in proton initiated air showers

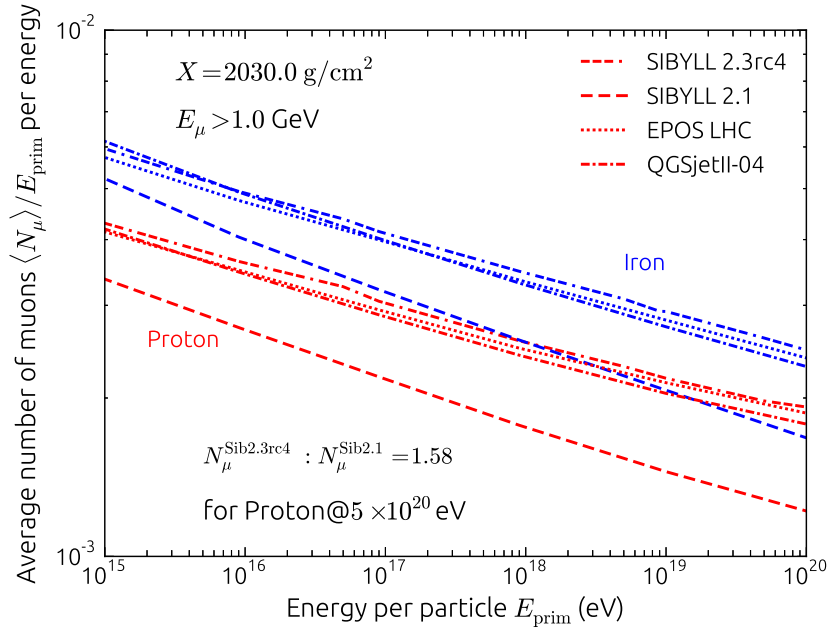


Figure 10.4: Comparison between the predicted number of muons in proton and iron induced air showers. Note that the predicted number of muons in an iron induced shower for SIBYLL 2.1 at the highest energies is lower than for proton induced showers of the same energy for the new models.

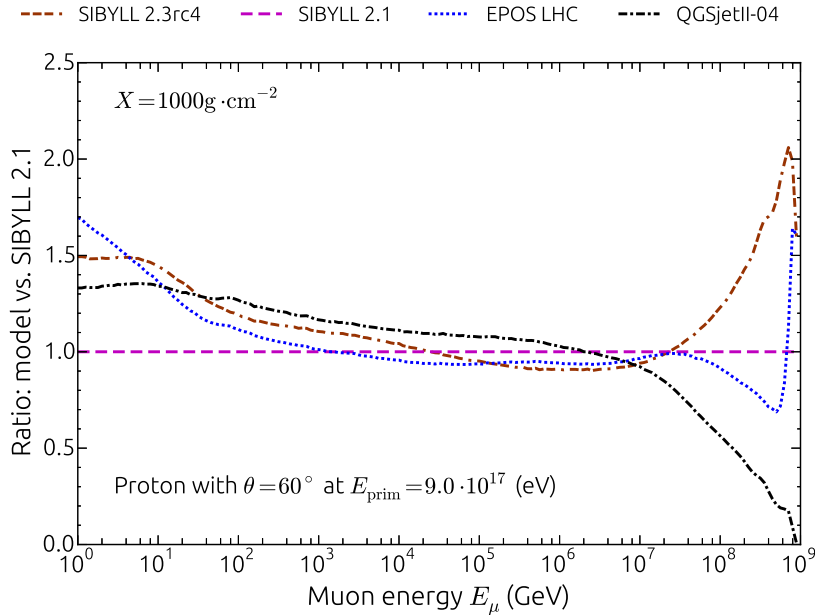


Figure 10.5: Ratio of the energy spectrum of muons in different models relative to SIBYLL 2.1. The primary particles are protons with an energy of 10^{18} eV. Increased baryon and ρ production mostly affect the number of low energy muons. The increase at high energy for SIBYLL 2.3 is due to the decay of charmed hadrons.

as a function of energy for the old and new version of SIBYLL is shown in Fig. 10.3. In order to ensure the full development of the air showers within the depth of one atmosphere up to the highest energy, the simulations are done by injecting the primary particles with an inclination of 60° and then the number of muons is determined at a depth of 2030 g/cm^2 . The energy

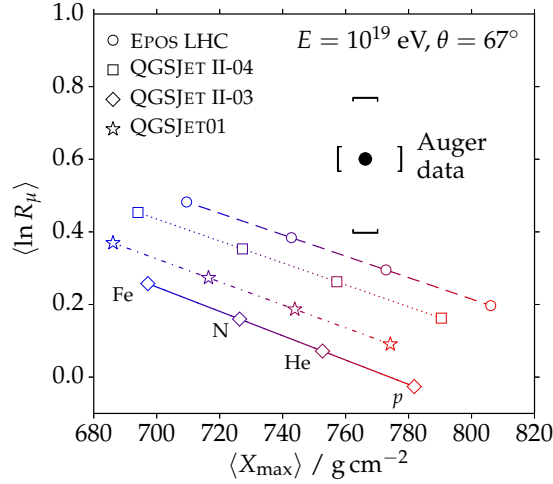


Figure 10.6: Comparison of the composition interpretation of shower maximum and muon measurements at the Pierre Auger Observatory compared [21]. In the new SIBYLL model, consistency between the measurements in terms of a sensible interpretation improves.

threshold for the muons is set to 1 GeV. The predictions from EPOS-LHC and QGSJET II-04 are shown for comparison as well.

The new version of SIBYLL predicts similar but slightly larger numbers of muons than the other LHC tuned models. Compared to SIBYLL 2.1 the number of muons has significantly increased at all energies. At 10^{20} eV the relative increase is $\simeq 60\%$. The slope of the curves corresponds to the exponent α in Eq. 2.25, which reflects the fraction of muon producing hadrons (π^\pm in Heitler-Matthews model) in the model. The increase from SIBYLL 2.1 to SIBYLL 2.3 is probably due to the increased production of vector mesons and is further discussed in Sect. 10.1.3.

The full significance of the increase becomes clear in Fig. 10.4, where the muon number in proton and iron showers is compared. The new model predicts a larger number of muons in proton showers at the highest energies than the previous model produced for iron initiated showers, suggesting a large change in the interpretation of measurements in terms of composition.

As an illustration of the origin of the additional muons, the ratio of the energy spectrum of muons at a depth of 1000 g/cm^2 in the new model and the other LHC tuned models relative to the old SIBYLL model is shown in Fig. 10.5. The showers are proton initiated with a primary energy of around 10^{18} eV. The signature of muons produced in the cascade is that low energies are affected more than high energies. This is clearly seen in the figure. All new models have significantly more muons at low energy compared to SIBYLL 2.1. The large relative increase at energies beyond 10 PeV in SIBYLL 2.3 is the contribution from the prompt muons due to charm decay. SIBYLL 2.3 is the only post-LHC model that includes the production of charmed particles. Since the energy spectrum of the muons is very steep these muons do not contribute to the total number of muons.

Returning to the discussion of the muon problem (Fig. 10.6), the increased $\langle X_{\max} \rangle$ and the increased number of muons both work in the correct direction to ease the tension between the measurements. Compared to the $\langle X_{\max} \rangle$ in the EPOS-LHC model in Fig. 10.2 there is a difference of $\approx 10 \text{ g/cm}^2$ at 10^{19} eV. Given that the number of muons is very similar in SIBYLL 2.3, the corresponding line in Fig. 10.6 would be just in the range of the experimental error. However, the quantity $\langle \ln R_\mu \rangle$, is derived from the signal in a surface detector which may not be sensitive to muons at all energies. Looking at the energy spectrum of the muons, there are some differences between the models, so the prediction for $\langle \ln R_\mu \rangle$ by SIBYLL might not lie as high as the prediction by EPOS-LHC. Nevertheless the change in the number of muons and $\langle X_{\max} \rangle$ is in the right direction.

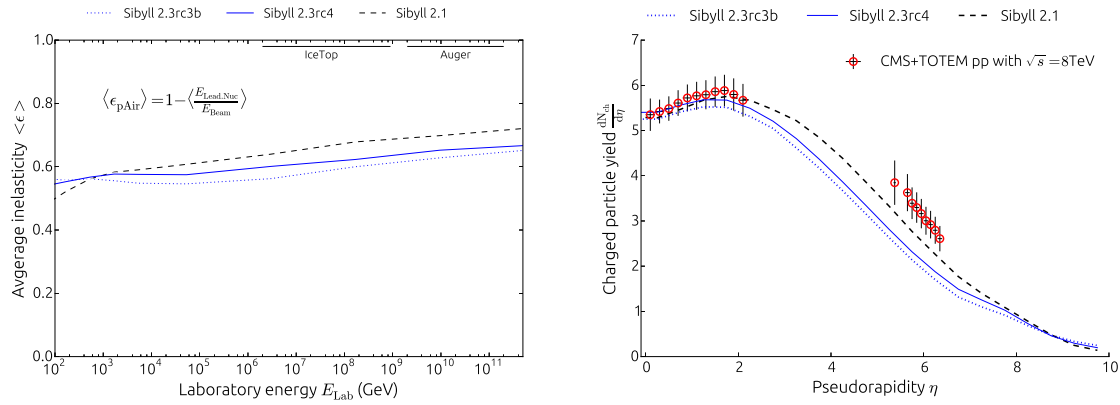


Figure 10.7: Link between central particle production and X_{max} . Left: Inelasticity in proton air interactions as a function of energy. Shown are the predictions for the models SIBYLL 2.1, SIBYLL 2.3 and an intermediate version (rc3b). Right: Pseudorapidity distribution of charged particles for the same three models.

10.1.3 Discussion of uncertainties

Some of the model extensions presented before, like ρ production, were explicitly included to improve the description of muons in air shower simulations. Others were done to improve the description of inclusive atmospheric fluxes (charm production, remnant) and some purely to describe accelerator data better (PDFs). As a result the model has improved in the selected aspects but the description has become worse in other directions and new problems have been revealed (Sect. 9). The next step in the process is to search for links between the established shortcomings of the model and the description of air shower measurements.

X_{max} and central particle production

In the previous chapter it was revealed that the width of the angular distribution (pseudorapidity) of charged particles is not described very well by the model. The discrepancy was argued to be due to the oversimplified representation of (mini)jets. While the angular distribution in itself does not matter very much for air shower development, as it might only affect the lateral spread of the particles, the multiplicity does matter and so does the inelasticity. Due to energy conservation the angular distribution is linked to the inelasticity. If the plateau in pseudorapidity is reproduced, but the distribution is too narrow, then the multiplicity will be too low. Since it is the small angle (large momentum) contribution that is misrepresented, the effect on the inelasticity, compared to too few particles in the very central region, is maximal.

In Fig. 10.7 the comparison of the inelasticity and the pseudorapidity distribution in SIBYLL 2.1, SIBYLL 2.3 and an intermediate version (rc3b) are shown. The pseudorapidity distribution is too narrow compared to the measurement in all three models. The model with the widest distribution is SIBYLL 2.1, correspondingly the inelasticity is largest in SIBYLL 2.1.

Based on the connection between inelasticity and the depth of shower maximum that was discussed in Sect. 2.3.3 (e.g. Fig. 2.10), the average depth of shower maximum is expected to decrease when the width of the pseudorapidity distribution is increased.

N_{μ} and meson interactions

In the discussion of the link between hadronic interactions and the number of muons in Sect. 2.3.3, the two mechanisms for muon production were prompt production and production in the cascade. The latter is important in air showers and it is influenced by the production of baryons and the fraction of hadrons that decay into muons relative to all hadrons. The interactions that occur most often in the cascade are pion interactions (see multiplicities at high energy in Fig. 9.12). Due to the exponential growth of particle number and the dispersion of the energy among particles, these interactions occur at energies well below the primary energy.

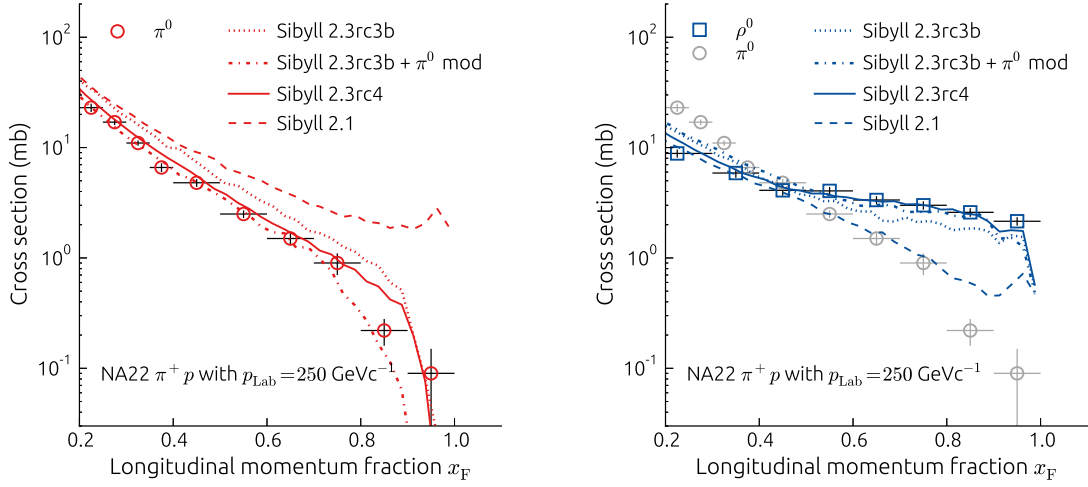


Figure 10.8: Production of π^0 (left) and ρ^0 (right) as a function of Feynman- x in π^+p collisions [94, 95]. The models shown are SIBYLL 2.1, SIBYLL 2.3 and two development versions that are described in the text. The crossover between neutral pion production and neutral ρ production at $x_F = 0.4$ has a large effect on the ratio between charged and neutral pions.

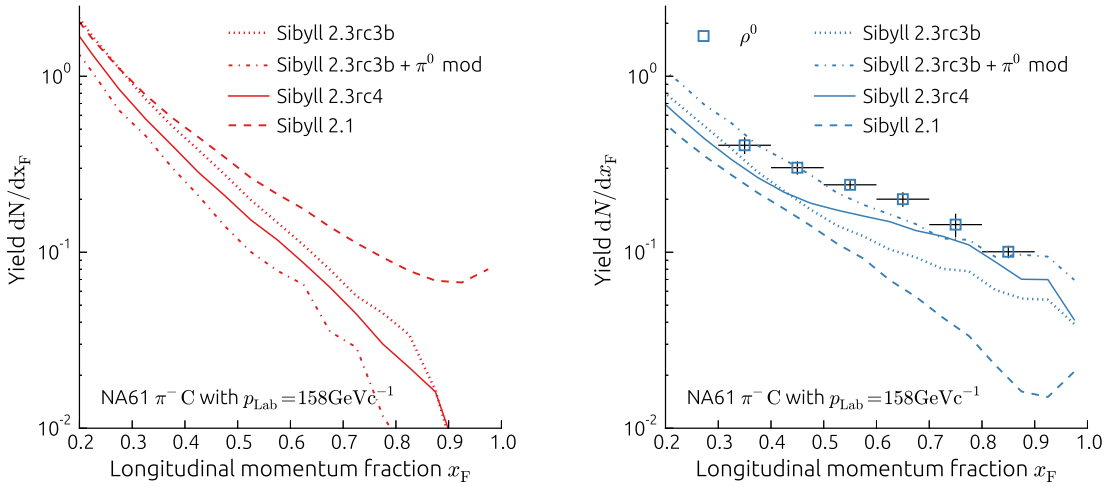


Figure 10.9: Longitudinal momentum spectra of neutral mesons in π^-C interactions in NA61 [96]. The data show a similar enhancement in the production of ρ^0 at large x_F as in the case of pion proton interactions.

The ratio of neutral ρ -mesons compared to neutral pions in pion interactions has a large influence on the production of muons because neutral ρ decay into π^\pm . Changing $\rho^0 : \pi^0$ then essentially changes $\pi^\pm : \pi^0$ (α in Eq. 2.25). The efficiency of changing the ratio between neutral and charged pions was already demonstrated in Fig. 2.8-right.

The extension of pion interactions in SIBYLL that allows the reproduction of the leading ρ observed in data were presented in Sect. 7.2. The results are summarized in Fig. 10.8. Apart from SIBYLL 2.1 and the new model, two intermediate versions, which describe the data with different degrees of accuracy, are shown. These intermediate models can be used to give an estimate of the range of predictions for the number of muons.

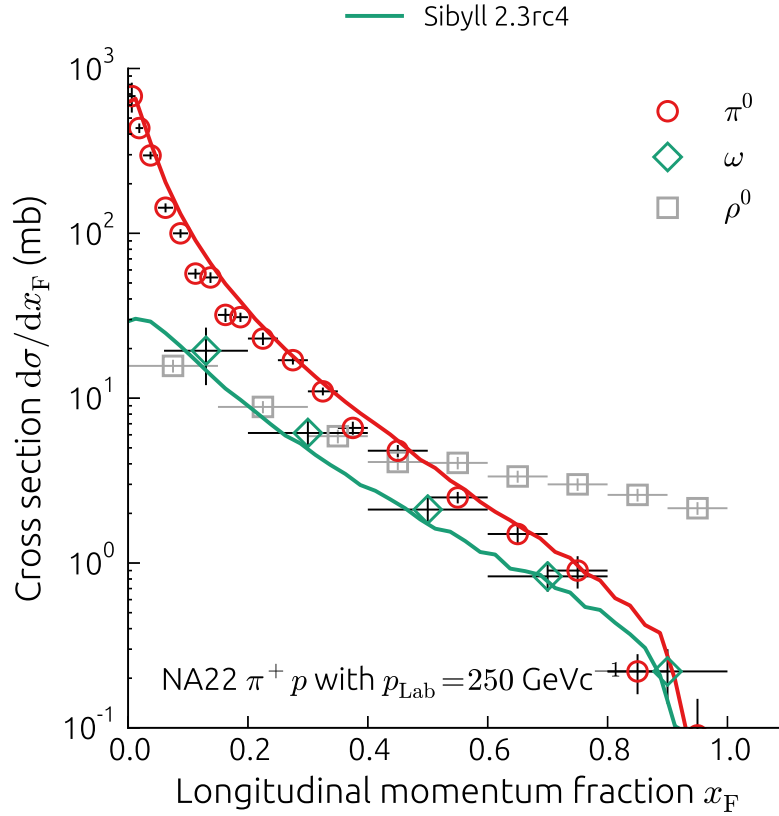


Figure 10.10: Feynman- x spectra of ω and π^0 -mesons [95]. The spectra show a similar suppression in the forward region, in strong contrast to the ρ -mesons.

The model rc3b uses a phenomenological approach similar to the one used in the current model (rc4, Sect. 7.2), but without explicit retuning of the remnant component. As a result the forward yield of neutral ρ in pp collisions (Fig. 10.8-left) is too low and the yield of π^0 is slightly too large (Fig. 10.8-right).

In the model labeled 'rc3b+ π^0 mod' this remaining discrepancy is removed ad-hoc by exchanging neutral π mesons with ρ mesons in the final state. While this procedure is enough to make the model agree with the data for leading ρ , it is not sufficient to describe the neutral pions. To account for these, π^0 in addition are randomly replaced by π^\pm with a probability proportional to the Feynman- x of the pions. The resulting model describes the NA22 data with similar accuracy to the current model (rc4), central ρ are somewhat overestimated but neutral pions agree well with data.

The part of the distribution that affects the ratio of charged to neutral pions the most and which therefore should be reproduced most accurately, is the region where ρ -production exceeds the production of neutral pions, which is the region $x_F > 0.5$.

In Fig. 10.9 a comparison of the same four models with the results from pion carbon interactions in NA61 is shown. Here the ad-hoc tune describes the leading ρ^0 best. For neutral pions unfortunately there are no data available. It should be noted that the NA61 measurement is very recent and still preliminary [96]. Eventually the spectrum for the ω -meson will be measured as well, which could give a hint on the shape of the spectrum of the neutral pions, since, at least in π proton interactions, the two distributions have the same shape (see Fig. 10.10).

Since the ad-hoc model is constructed independent of the identity of the target particle it is not surprising it reproduces the data in pion carbon interactions. In the microscopic models the transition from a proton target to a nucleus increases the number of hadronizing systems (multiple target nucleons interacting), which have to share the available energy. This typically

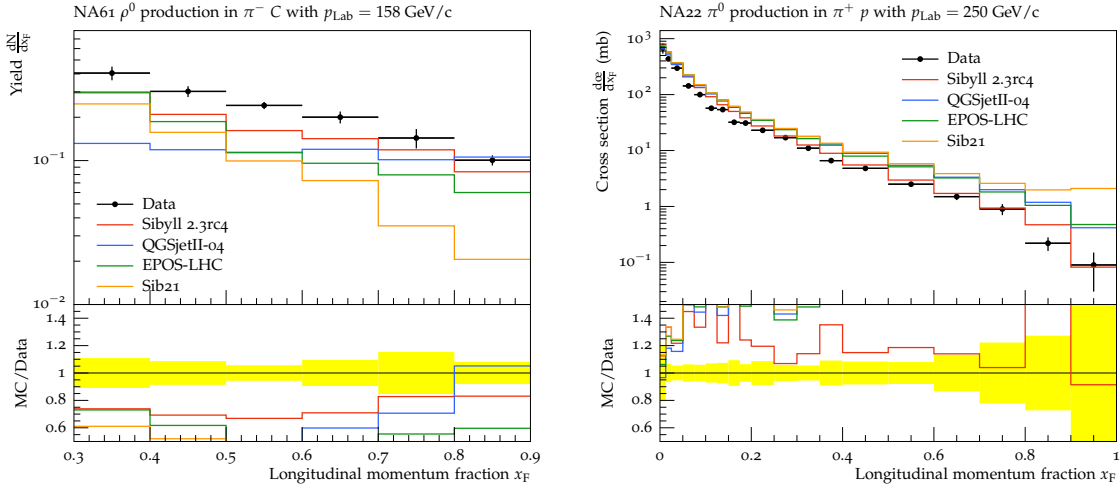


Figure 10.11: Left: ρ -mesons measured in pion carbon interactions. Right: π^0 produced in pion proton interactions. Predictions for the latest CR interaction models and SIBYLL 2.1 are shown. Based on these comparisons the ratio of charged to neutral pions (α) is too small in all models.

reduces the momentum of the leading particle (e.g. leading protons in remnant model, Sect. 5). It is particularly unlikely to produce a heavier resonance like the ρ ($m_\pi = 0.139$ GeV vs. $m_\rho = 0.770$ GeV) when the cm. energy is only $\sqrt{s} \approx 17$ GeV. This makes the confirmation of the leading ρ effect for pion carbon interactions by the NA61 measurement very important.

In Fig. 10.11 on the left, the prediction of ρ^0 production by SIBYLL 2.1, SIBYLL 2.3 and the other CR models EPOS-LHC and QGSJET II-04 are shown. All models, except SIBYLL 2.1 were tuned to the proton data, but not the carbon data. All models reproduce the very forward production but can not account for the intermediate region $x_F < 0.8$. If the crossover between the π^0 and ρ^0 spectra is at the same position in pion carbon interactions as in pion proton, then the ratio of charged to neutral pions is probably too low in all the models.

The ad-hoc tune reproduces the ρ^0 -spectrum in pion carbon interactions best, so it can give an estimate of the number of muons in air showers if the ρ^0 are accounted for. The effect is shown in Fig. 10.12. Compared to the latest models, EPOS-LHC, QGSJET II-04 and SIBYLL 2.3, the ad-hoc model predicts another substantial increase in muon number if the NA61 ρ^0 data is included. With regard to the number of muons in SIBYLL 2.1, the relative increase is $\approx 100\%$.

The slope of the number of muons as a function of energy increases notably, which is consistent with an increase of α .

The ratio of the energy spectra in Fig. 10.13 shows the increase in muon number is largely due to low energy muons which confirms the increased cascade production.

To summarize, the number of muons as predicted by current hadronic interaction models is probably still underestimated. Due to the strong link between the ratio of charged and neutral pions and the number of muons, the predictions will remain uncertain, until the forward production of charged and neutral pions in pion nucleus interactions is measured.

X_{\max} and cross sections

The role of the proton cross section was already discussed in the context of the measurement of the proton air cross section in the introduction to this chapter. The effect of the proton interaction length is demonstrated by exchanging the interaction lengths in the cascade calculations. The difference in X_{\max} is not very large as can be seen on the left in Fig. 10.14.

The same can be done for meson air cross sections. Instead of the old SIBYLL cross section which does not describe the LHC proton measurement very well nor the measurement by the Pierre Auger Observatory at 57 TeV, the COMPETE cross section model [16] is used. Because the cross section for pion interactions in the model is linked to proton interactions, the cross section

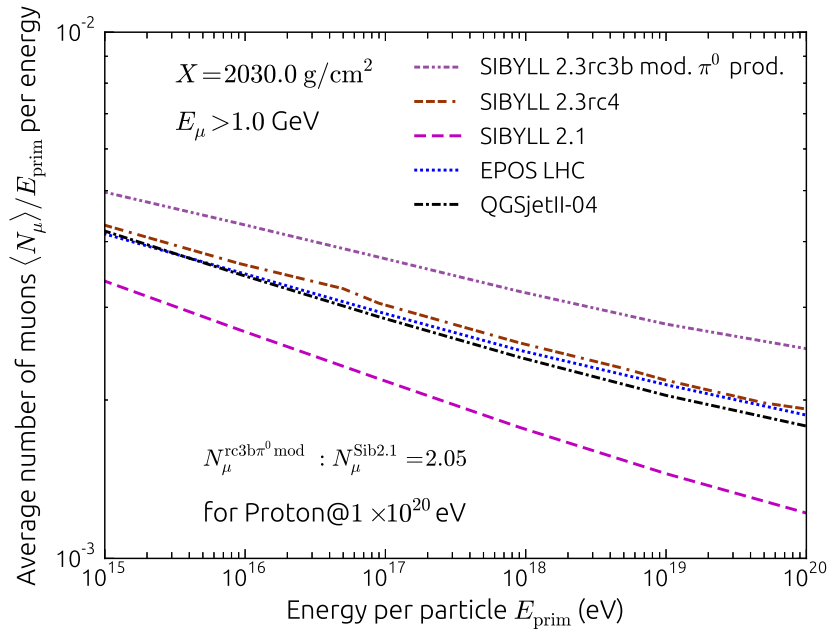


Figure 10.12: Dependency of the number of muons in air showers on the ratio of π^0 to ρ^0 production.

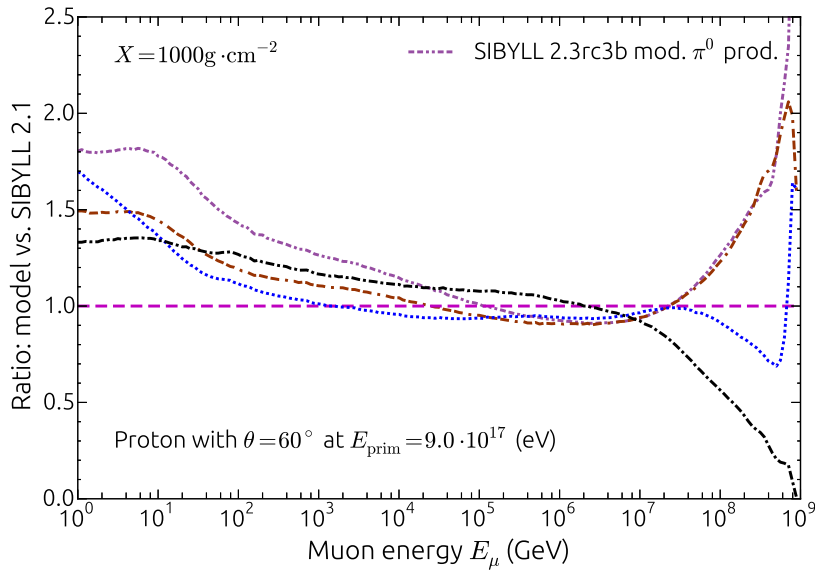


Figure 10.13: Effect of π^0/ρ^0 production on the energy spectrum of muons in proton initiated air showers. The spectra are shown relative to SIBYLL 2.1.

in SIBYLL 2.1 is not a valid alternative although it still describes the available pion data. The effective difference between the cross sections is that the cross section in SIBYLL is smaller at cm. energies below 5 TeV ($E_{\text{Lab}} \simeq 10^{16}$ eV) and larger at higher energy (see Fig. 10.14-right). The convergence of the cross sections for the different hadrons at high energy is due to the increasing contribution from sea quarks and gluons, which is universal. Meson interactions are important in later stages of the air shower so the difference at the lower energies is important. The effect of the meson interaction length is found to mostly appear in the so-called muon production profile (Fig. 10.15-right). It shows how the longer meson interaction length in SIBYLL at the energies where meson interactions take place, moves muon production deeper into the atmosphere. The

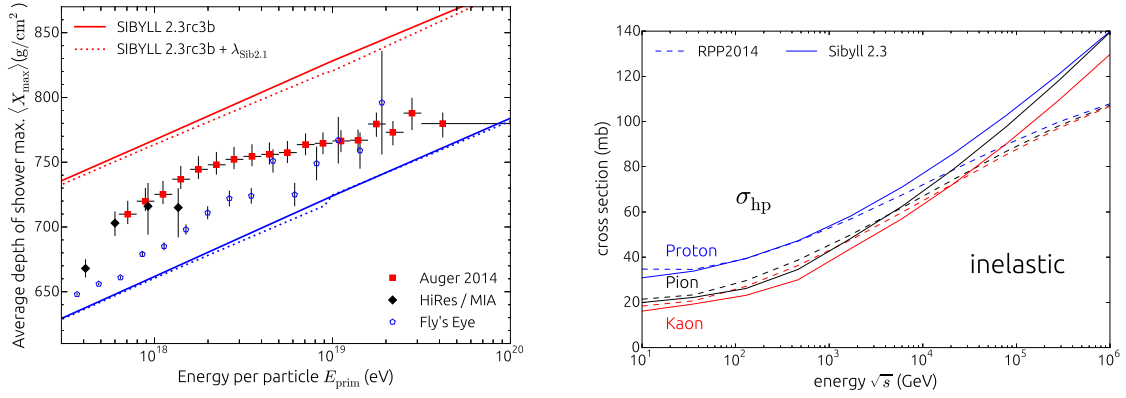


Figure 10.14: Left: Effect of different interaction lengths on X_{\max} at the highest energies. The interaction lengths were only exchanged for proton primaries, the difference in the iron prediction is due to different binning. Right: Comparison of the proton, pion and kaon cross section with air in SIBYLL 2.3 and the COMPETE model [16].

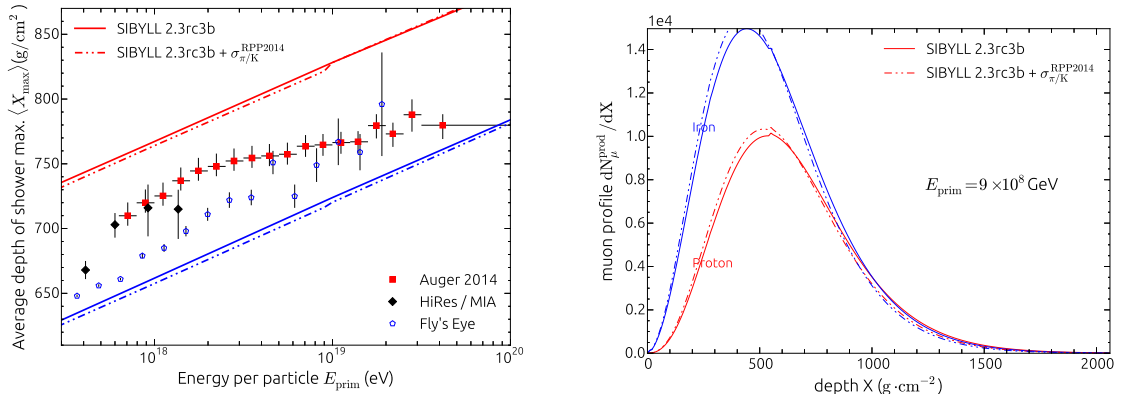


Figure 10.15: Effect of the meson interaction lengths in SIBYLL and the COMPETE model from the Review of Particle Physics 2014 [16].

total number of muons at ground is left unchanged from the modification. The effect on X_{\max} is negligible (Fig. 10.15), which is expected because the early interactions that define the em. component and X_{\max} are proton interactions. It should be added that the models for meson interactions are relatively unconstrained, since there are only few measurements available. The largest constraint comes from within the models through the link between meson and proton interactions.

In Sect. 8 the extended Glauber calculation that now includes inelastic intermediate states was presented. Although the production cross section does not change by much and thereby the interaction length (see Fig. 10.1), there might still be a significant change in X_{\max} due to the increase of the diffractive cross section. This can be seen on the left in Fig. 10.16 where X_{\max} is compared between SIBYLL 2.3, SIBYLL 2.1 and a modified version of the new model where only nuclear diffraction is treated according to the old model. On the right the longitudinal shower profiles are compared between these models. Due to the enhanced cross section for nuclear diffraction, the showers in SIBYLL 2.3 are more penetrating.

10.2 Inclusive atmospheric fluxes

The predictions for the atmospheric fluxes of muons and neutrinos shown here were calculated with a matrix representation of the cascade equations introduced in Sect. 2.4. Details can be found in Ref. [134, 135] or the thesis of A. Fedynitch [136].

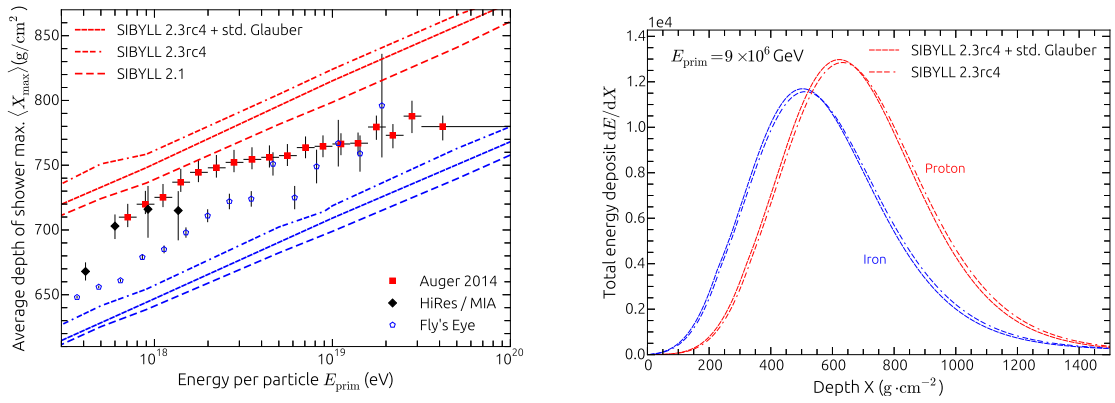


Figure 10.16: Left: Average depth of shower maximum between SIBYLL 2.1, SIBYLL 2.3 and an intermediate model without the extended Glauber calculation. In particular diffraction dissociation in that model is sampled as incoherent only (see Sect. 8). For each interacting nucleon the probability of an diffractive interaction is determined from the hadron nucleon cross section. Right: Shower profiles between SIBYLL 2.3 with and without inelastic intermediate states and coherent diffraction.

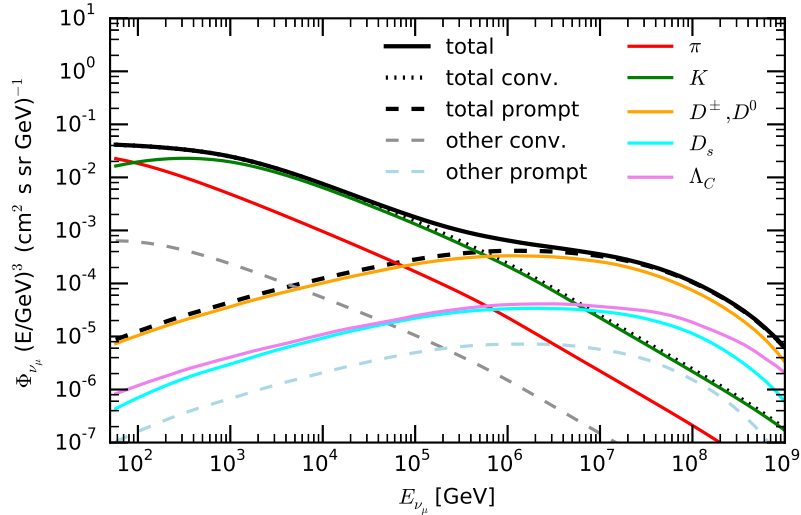


Figure 10.17: Atmospheric flux of muon neutrinos separated by components. The calculation was done with the a development version of SIBYLL 2.3 [135].

The improvement of the description of the muon flux and charge ratio at low energies was part of the motivation to include the explicit treatment of beam remnants. The prompt neutrino component from charm decays is the reason charm production was introduced.

10.2.1 Atmospheric neutrino flux

In Fig. 10.17 the flux of muon neutrinos in the energy range from 100 GeV up to 1 EeV is shown. The flux is separated into the contributions from the different components, that are responsible for some of the features in the spectrum. The effect of the charmed particles is visible in the break of the spectrum between 100 TeV and 1 PeV.

In Fig. 10.18 the component of the flux due to charmed hadrons is shown separately in order to compare the prediction by SIBYLL with other models. The predictions by SIBYLL are all at the lower end. SIBYLL 2.3-PL in the figure represents the prediction of the charm model in SIBYLL, assuming that the interactions producing charm are all point-like (PL) interactions. In that case

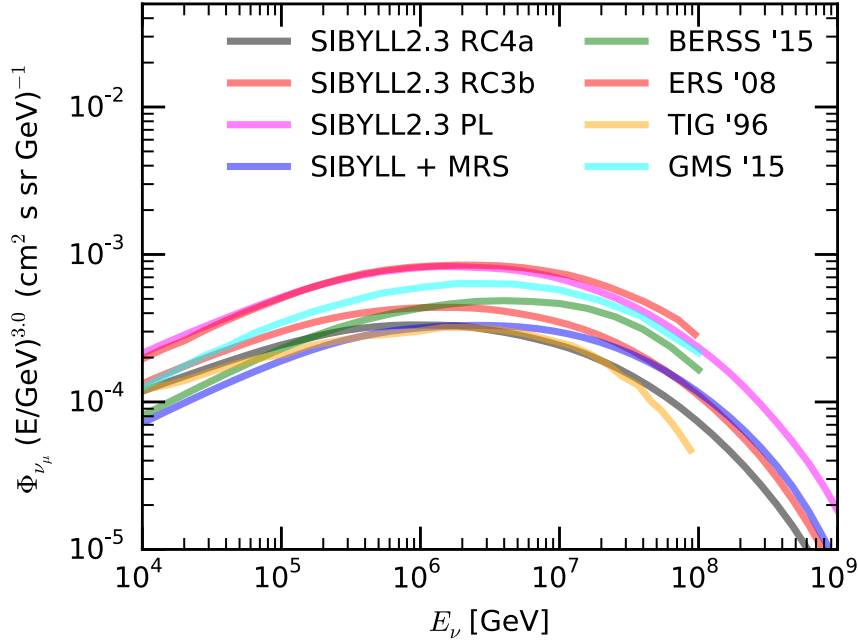


Figure 10.18: Prompt component of the atmospheric flux of muon neutrinos in different models [135].

the production of charm in proton proton collisions can be translated to proton air by rescaling it with the number of interacting nucleons. This corresponds to the procedure used in most other models [134].

10.2.2 Atmospheric muon production and charge ratio

The prediction of the flux of muons in the atmosphere is shown in Fig. 10.19, separated by components as well. The main difference to the neutrino flux is that the prompt component is dominated by the $\mu^+\mu^-$ decay of unflavored resonances not charmed hadrons.

Another difference is, that the dominant contribution at low energies is always the decay of pions, while for neutrinos there is a transition between pion and kaon dominated regions at around 100 GeV. This is due to the effect of the mass difference on the 2-body decay kinematic. The closer the mass of one of the final state particles is to the parent hadrons mass, the larger the average fraction of the energy it carries will be. Since the muon mass is close to the pion mass, the energy fraction of the muon in pion decay is on average $\langle E_\mu \rangle / E_\pi = 0.79$. For kaon decay it is $\langle E_\mu \rangle / E_K = 0.52$. At high energy the re-interaction of pions is more likely than decay so muons or neutrinos with that energy are unlikely to be produced. Therefore there is a break in the pion/kaon contribution to the lepton spectrum. The difference in the decay length of pions and kaons means the break occurs at different energies. For muons the difference is compensated by the difference in the energy fraction, for neutrinos it is enhanced.

The shift of the relative contribution of pions and kaons to the flux of muons is also responsible for the change in the charge ratio the muons, that can be seen in Fig. 10.20 on the left. Since the charge ratio is larger for kaons than for pions (K^- can only be produced from sea flavors), the muon charge ratio increases at the energy where the contribution from kaon decays increases (≈ 1 TeV). Compared to the measurements, the charge ratio is generally a little too high in the new model.

In Fig. 10.20, on the left, the flux of muons at low energy is shown [137]. The measurement is binned in zenith angle. The predictions shown are SIBYLL 2.3 and different models for the primary flux.

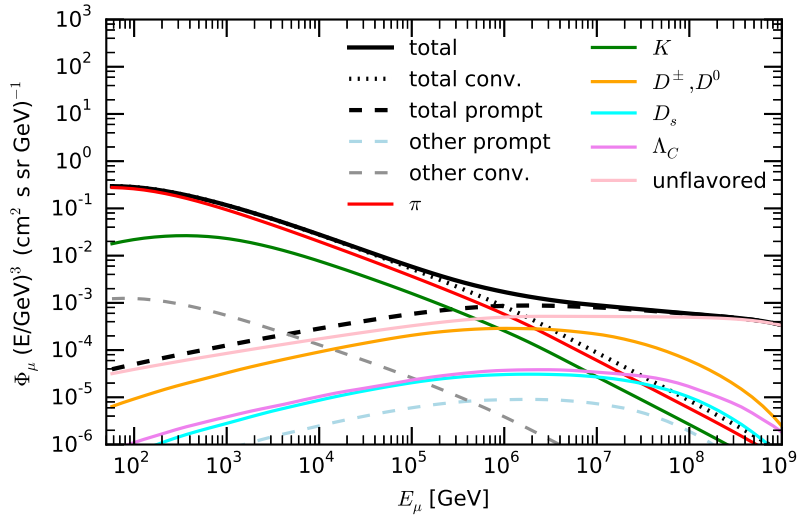


Figure 10.19: Atmospheric flux of muons separated by components. The calculation was done with a development version of SIBYLL 2.3 [135].

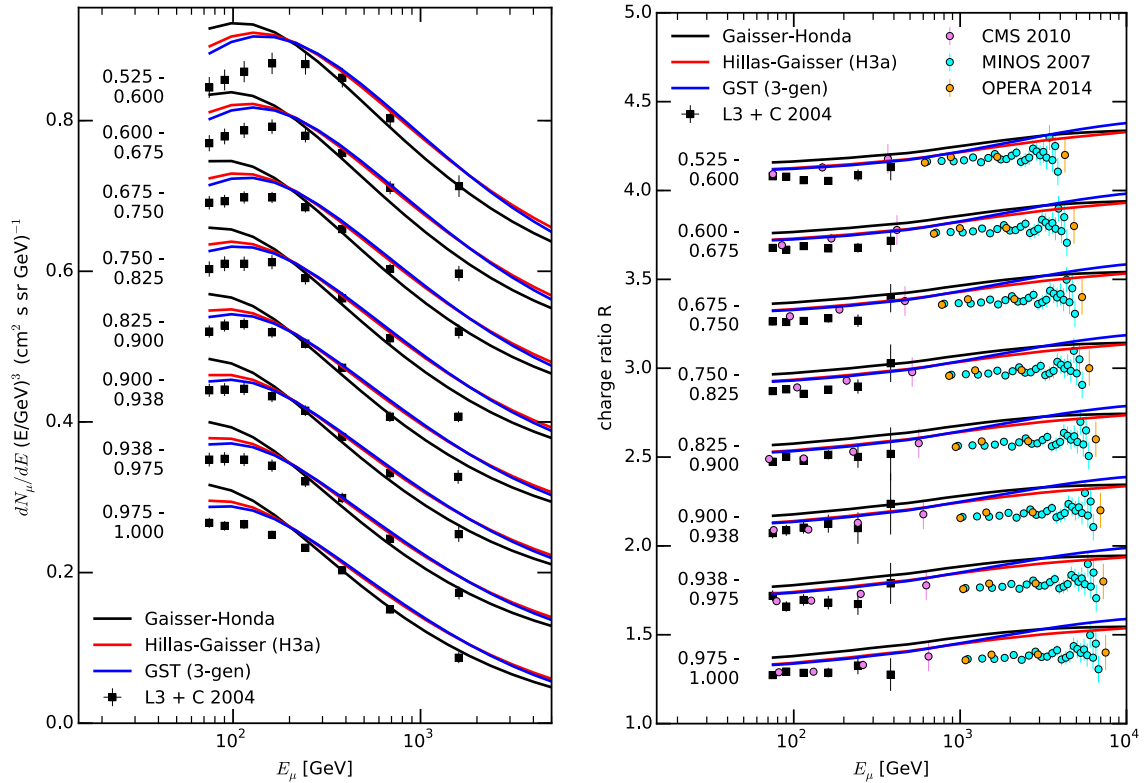


Figure 10.20: Left: Energy spectrum of atmospheric muons at low energy. Predictions are calculated with SIBYLL 2.3 and different primary flux models [138, 139, 140]. Data are separated in zenith angles, measured in L3+C [137]. Right: Charge ratio of atmospheric muons. Measurements are typically done underground [141, 137, 142].

Chapter 11

Conclusion

The subject of this work was the study of hadronic interactions in the light of the new LHC data and additional fixed target measurements and the influence of the new knowledge on multiparticle production on the interpretation of measurements of cosmic rays and atmospheric muons and neutrinos. Hadronic interactions were treated in the framework of the interaction model SIBYLL. The microscopic picture underlying the model was presented briefly. Several shortcomings of the model and new data from LHC and fixed target experiments served as motivation for its extension. Among those were the transverse momentum distributions, the related parton distribution functions and the cross section for minijet production. In the new version of the model, SIBYLL 2.3, the cross section and the transverse momentum spectra measured at accelerators are consistently better reproduced. In addition the new cross section was shown to be compatible with the air shower based measurements at the Pierre Auger Observatory.

The larger part of the model extensions were motivated by the input from air shower simulations and atmospheric flux calculations.

In the case of air showers, it has been noticed on multiple occasions that the interpretation of observables constructed from the electromagnetic shower component is inconsistent with observables determined by the hadronic component. This discrepancy suggests that some aspects of hadronic interactions, that are important in the development of an air shower, are not reproduced well enough in the interaction models. Because the hadronic component is measured through the muons, this discrepancy translates to a mismatch between the number of muons for a given electromagnetic shower signal between simulations and data.

In this work two mechanisms that have been suggested to influence the number of muons before were investigated. One is the production of baryons, the other is the ratio of leading neutral ρ -mesons to neutral pions in meson interactions. Both were found to be misrepresented in the original SIBYLL model. Extensions to the model were developed and shown to be able to rectify shortcomings of the model with respect to measurements at accelerators. The resulting effect on the number of muons in air showers, between the old model and the new one, was shown to be of the order of 60%. In general, the predictions on the muon number by the new version of SIBYLL agree very well with the predictions of other models that already include an improved description of these effects. But there are also significant differences in the depth of shower maximum.

Whether the mismatch between simulations and data for air showers is solved by this increase in muon number, unfortunately, can not be said. This has several reasons. One is, that the number of muons, that was calculated in this work, is the total number of muons. In air shower experiments, however, mainly quantities related to the density of muons in a given lateral distance range are measured and the correction of detector effects are not always included. It was shown that the increase in muon number affects mostly low energy muons. So, depending on the energy threshold of the measurement the observed increase may be smaller. Only a detailed analysis of individual measurements will show if the improvements are sufficient.

The second, more important, reason is that the data from laboratory experiments on the ρ/π ratio are insufficient. The relative enhancement of the production of leading ρ^0 to leading π^0

was unambiguously shown in the NA22 measurement. However, this measurement was done for pion proton collisions, while the interactions in air showers have a nuclear target: air. For pion nucleus interactions only half of the needed information is known. The NA61 collaboration confirms the forward production of ρ^0 in their measurement of π^- carbon interactions, but unfortunately no measurement of neutral pions was possible. Compared to the models tuned to the pion proton measurement, the pion carbon data show even more ρ production in forward direction. Without having a measurement of the neutral pions this can mean two things. First, the ratio ρ to π could be larger for nuclear targets, or secondly, the ratio could be the same and the suppression of forward particle production on nuclear targets is too strong in the models. The first case was shown to increase the number of muons even more, by about 100% relative to SIBYLL 2.1. Until pion nuclear interactions are measured in more detail, the prediction of the number of muons by interaction models remains very uncertain.

The case of inclusive fluxes of muons and neutrinos was mentioned only briefly. The measurement of the first astrophysical neutrinos in the IceCube experiment served as motivation to revisit a previous implementation of the production of charmed hadrons in SIBYLL. The old model was only tuned to low energy data, so it was not surprising that comparisons with recent LHC measurements of charmed hadron production, revealed that the model did not work at high energy. The production of charmed hadrons in air showers, therefore, was underestimated by a large amount. Due to the short lifetime and the decay into muons and neutrinos, decay of charmed hadrons in the atmosphere constitutes a large background to the IceCube measurement. The new model reproduces charm measurements well. The corresponding flux of neutrinos in the atmosphere was shown to be the lowest of all contemporary model predictions. It remains to be seen what the effect on the measurement of the astrophysical flux in IceCube will be.

Obtaining a good description of the inclusive flux of muons and the charge ratio of these muons in the atmosphere was part of the motivation for the inclusion of beam remnants in the treatment of leading particles in the new version of SIBYLL. Since cosmic rays are positively charged the muon charge ratio is larger than one. How much larger depends on the treatment of leading particles in the interactions and the mass composition of the primary cosmic ray flux. In particular, it depends on the charge ratio of pions and kaons in the forward fragmentation region. Both, the measured atmospheric charge ratio of muons or the pion or kaon charge ratios measured in laboratory experiments were not represented well in the old model. With the new treatment of beam remnants introduced with this thesis, the description of laboratory experiments was shown to improve. However, the atmospheric charge ratio was shown to be still too large in the model prediction.

Another reason for the extension of the old SIBYLL model is the aim of achieving a self consistent implementation of the underlying concepts and theoretical ideas. This served as part of the motivation to include so-called inelastic screening effects in the calculation of the hadron-nuclear cross sections.

Next to the successful extension of the model in certain key aspects, motivated by the requirements in particle astrophysics, the limitations of the model became evident on several occasions. For example, the comparison with the measurements of the multiplicity distribution at the LHC shows, that the effective saturation model used in SIBYLL is not sufficiently limiting the number of parton interactions in central collisions.

In addition, the distribution of charged particles in pseudorapidity was shown to be consistently too narrow. Compared to the overestimation of parton scattering this is a more serious problem for applications in air shower physics. While the region in pseudorapidity, where the deviations from the measurement occurs, has no direct influence on the development of air showers, it is nevertheless linked to the forward region through energy conservation and thereby changes the shower development. In particular, the prediction of $\langle X_{\max} \rangle$ was argued to be affected by this.

To summarize, in short, a new version of the hadronic interaction model SIBYLL has been developed and extensively tested. While the fundamentals of the model were left unchanged,

key processes and aspects, deemed important for air shower development, were updated and extended. The new model improved the description of hadronic interactions in most aspects, although some of the shortcomings of the previous model are still present. The predictions by the new model indicate that a more consistent interpretation of different air shower measurements will be possible and that the atmospheric neutrino flux due to charm hadrons may be lower than previously thought.

Acknowledgments

I would like to thank Prof. Dr. Dr. h. c. J. Blümer and Priv. Doz. Dr. Stefan Gieseke for reviewing this work.

Ralph Engel I want to thank for the supervision and guidance in this work and during my whole time as a graduate student.

I would like to thank Tom Gaisser and Todor Stanev for the encouraging discussions and their hospitality during my visit at the University of Delaware.

Anatoli Fedynitch I would like to thank for the helpful coding tips and the pleasant discussions about hadrons and life.

Colin Baus, Alex Herve, Daniela Mockler and David Schmidt I want to thank for the proof reading and discussions of the content of this work.

Darko Veberic, I want to thank for the coding, texing and 'how to trick oneself into writing' tricks. Not to mention the distractions.

Appendix A

Appendix

A.1 Model parameters

The parameters listed here reflect the situation in SIBYLL 2.3.

A.1.1 Cross section

A.1.2 Fragmentation parameters

The parameters of string fragmentation in are changed in certain configurations (e.g. minijets). The default parameters are given in Tab. [A.4](#). Parameters of the Lund fragmentation function are $a = 0.8$ and $b = 0.5$.

A.2 Particle listings

A.2.1 Final state particles

Table A.1: Table of the parameters in the pp cross section model of SIBYLL 2.3. The corresponding equations are shown in Sect. 3.1.

Model process	symbol	value
density profiles:		
hard scattering	ν_h	0.77
	μ_h	-8.8
soft scattering (first term)	ν_{s1}	3.175
	μ_{s1}	0.25
soft scattering (second term)	ν_{s2}	0.5
	μ_{s1}	0.9
hard cross section		
lower boundary of σ_{QCD}	p_T^0	1.0
	Λ	0.065
	c	0.9
higher order correction	K	2.0
soft cross section		
	X	49.89
	Y	$8.03 \cdot 10^{-5}$
	Δ	0.0244
	ϵ	0.4
diffraction dissociation		
	α_A	0.2
	α_B	0.0
	β_A	0.5
	β_B	0.6

Table A.2: Table of the parameters in the πp cross section model of SIBYLL 2.3

Process	parameter name	value
density profiles:		
hard scattering	ν_h	1.0
	μ_h	-8.8
soft scattering (first term)	ν_{s1}	2.29
	μ_{s1}	0.25
soft scattering (second term)	ν_{s2}	0.55
	μ_{s1}	0.9
hard cross section		
lower boundary of σ_{QCD}	p_T^0	1.0
	Λ	0.065
	c	0.9
higher order correction	K	2.0
soft cross section		
	X	22.92
	Y	90.45
	Δ	0.0305
	ϵ	0.077
diffraction dissociation		
	α_A	0.2
	α_B	0.0
	β_A	0.5
	β_B	0.6

Table A.3: Table of the parameters in the Kp cross section model of SIBYLL 2.3.

Process	parameter name	value
density profiles:		
hard scattering	ν_h	1.0
	μ_h	-8.8
soft scattering (first term)	ν_{s1}	1.188
	μ_{s1}	0.25
soft scattering (second term)	ν_{s2}	0.5
	μ_{s1}	0.9
hard cross section		
lower boundary of σ_{QCD}	p_T^0	1.0
	Λ	0.065
	c	0.9
higher order correction	K	2.0
soft cross section		
	X	21.60
	Y	$9.76 \cdot 10^{-5}$
	Δ	0.018
	ϵ	0.4
diffraction dissociation		
	α_A	0.2
	α_B	0.0
	β_A	0.5
	β_B	0.6

Table A.4: Table of the parameters of fragmentation.

rate	value
P_{qq}/P_q	0.08
$P_{u,d}/P_s$	0.38
$P_{ud}/P_{us,ds}$	0.5
P_{spin1}/P_{spin0}	0.3
$P_{s,spin1}/P_{s,spin0}$	0.3
$P_{spin3/2}/P_{spin1/2}$	0.15
$P_{popcorn}$	0.5

Table A.5: Table of final state particles from SIBYLL 2.1. Mesons and non hadronic particles on the left, baryons on the right.

Part.	Id	PDG id
γ	1	22
e^+	2	-11
e^-	3	11
μ^+	4	-13
μ^-	5	13
π^0	6	111
π^+	7	211
π^-	8	-211
K^+	9	321
K^-	10	-321
K_L^0	11	130
K_S^0	12	310
p	13	2212
n	14	2112
ν_e	15	12
$\bar{\nu}_e$	16	-12
ν_μ	17	14
$\bar{\nu}_\mu$	18	-14
K^0	21	311
\bar{K}^0	22	-311
η	23	221
η'	24	331
ρ^+	25	213
ρ^-	26	-213
ρ^0	27	113
K^{*+}	28	10321
K^{*-}	29	-10321
K^{*0}	30	10311
\bar{K}^{*0}	31	-10311
ω	32	223
ϕ	33	333

Part.	Id	PDG id
Σ^+	34	3222
Σ^0	35	3212
Σ^-	36	3112
Ξ^0	37	3322
Ξ^-	38	3312
Λ^0	39	3122
Δ^{++}	40	2224
Δ^+	41	2214
Δ^0	42	2114
Δ^-	43	1114
Σ^{*+}	44	3224
Σ^{*0}	45	3214
Σ^{*-}	46	3114
Ξ^{*0}	47	3324
Ξ^{*-}	48	3314
Ω^-	49	3334

Table A.6: Table of charmed particles in the new SIBYLL 2.3.

Part.	Id	PDG id
D^+	59	411
D^-	60	-411
D^0	71	421
\bar{D}^0	72	-421
D_s^+	74	431
D_s^-	75	-431
D^{*+}	78	10411
D^{*-}	79	-10411
D_s^0	80	10421
\bar{D}_s^0	81	-10421
Σ_c^+	85	4212
Σ_c^0	86	4112
Ξ_c^+	87	4232
Ξ_c^0	88	4132
Λ_c^+	89	4122
Σ_c^{*++}	94	4224
Σ_c^{*+}	95	4214
Σ_c^{*0}	96	4114
Ξ_c^{*+}	97	4324
Ξ_c^{*0}	98	4314
Ω_c^0	99	4332

Table A.7: Table of resonances in SIBYLL 2.3.

Part.	Id	PDG id
$N(1440)^+$	51	0
$N(1440)^0$	52	0
$N(1770)^+$	53	0
$N(1770)^0$	54	0
a_0^0	61	0
a_0^+	62	0
a_0^-	63	0
K_0^{*+}	64	0
K_0^{*-}	65	0
K_0^{*0}	66	0
\bar{K}_0^{*0}	67	0

Bibliography

- [1] R. Engel, D. Heck, and T. Pierog, *Ann.Rev.Nucl.Part.Sci.* 61 (2011) 467–489.
- [2] J. Blümer, R. Engel, and J. R. Hörandel, *Prog. Part. Nucl. Phys.* 63 (2009) 293–338.
- [3] K. Greisen, *Phys. Rev. Lett.* 16 (1966) 748–750.
- [4] G. T. Zatsepin and V. A. Kuzmin, *Pis'ma Zh. Eksp. Teor. Fiz.* 4 (1966) 114.
- [5] M. G. Aartsen *et al.* (IceCube Collab.), *Phys. Rev. Lett.* 113 (2014) 101101
- [6] W. Stirling, private communication.
- [7] R. P. Feynman, *Phys. Rev. Lett.* 23 (1969) 1415.
- [8] T. K. Gaisser, *Cosmic rays and particle physics*, Cambridge Univ. Press, Cambridge, 1990.
- [9] J. Matthews, *Astropart. Phys.* 22 (2005) 387–397.
- [10] I. Engeln and R. Engel, *Bachelor thesis*, 2015.
- [11] K. Alpgard *et al.* (UA5 Collab.), *Phys. Lett.* 112B (1982) 183.
- [12] J. Alvarez-Muniz, R. Engel, T. K. Gaisser, J. A. Ortiz, and T. Stanev, *Phys. Rev. D* 66 (2002) 033011.
- [13] J. Linsley and A. A. Watson, *Phys. Rev. Lett.* 46 (1981) 459–463.
- [14] A. N. Bunner, *PhD thesis*, Cornell University, 1967.
- [15] R. Ulrich, C. Baus, and R. Engel, *EPJ Web of Conferences* 99 (2015) 11001.
- [16] K. Olive *et al.* (Particle Data Group Collab.), *Chin.Phys.* C38 (2014) 090001.
- [17] C. A. Garcia Canal, J. I. Illana, M. Masip, and S. J. Sciutto, *Astropart. Phys.* 46 (2013) 29–33
- [18] P. K. F. Grieder, *Proc. of 13th Int. Cosmic Ray Conf., Denver* 4 (1973) 2467.
- [19] H.-J. Drescher, *Phys. Rev. D* 77 (2007) 056003.
- [20] T. Pierog and K. Werner, *Phys. Rev. Lett.* 101 (2008) 171101.
- [21] A. Aab *et al.* (Pierre Auger Collab.), *Phys. Rev. D* 91 (2015) 032003 [Erratum: *Phys. Rev. D* 91, no. 5, 059901 (2015)].
- [22] T. Pierog, I. Karpenko, J. M. Katzy, E. Yatsenko, and K. Werner, *Phys. Rev. C* 92 (2015) 034906
- [23] S. Ostapchenko, *Phys. Rev. D* 83 (2011) 014018
- [24] R. Ulrich, R. Engel, and M. Unger, *Phys. Rev. D* 83 (2011) 054026.
- [25] W. Bothe and W. Kohlhoerster, *Zeitschr. f. Physik* 56 (1929) 751.

- [26] T. Bergmann *et al.*, *Astropart. Phys.* 26 (2007) 420–432.
- [27] E.-J. Ahn, R. Engel, T. K. Gaisser, P. Lipari, and T. Stanev, *Phys. Rev. D* 80 (2009) 094003.
- [28] A. Capella and A. Krzywicki, *Phys. Rev. D* 18 (1978) 3357.
- [29] A. Capella and J. Tran Thanh Van, *Z. Phys.* C10 (1981) 249–262.
- [30] A. Capella, U. Sukhatme, C. I. Tan, and J. Tran Thanh Van, *Phys. Rept.* 236 (1994) 225–329.
- [31] P. D. B. Collins, *An Introduction to Regge Theorie & High Energy Physics*, Cambridge University Press, Cambridge 1977.
- [32] G. 't Hooft, *Nucl. Phys.* B72 (1974) 461.
- [33] K. Gottfried, *CERN-72-20* (1972) 21.
- [34] M. Glück, E. Reya, and A. Vogt, *Z. Phys.* C67 (1995) 433–448.
- [35] M. Glück, E. Reya, and A. Vogt, *Eur. Phys. J.* C5 (1998) 461–470
- [36] L. V. Gribov, E. M. Levin, and M. G. Ryskin, *Phys. Rept.* 100 (1983) 1–150.
- [37] E. M. Levin and M. G. Ryskin, *Phys. Rept.* 189 (1990) 267–382.
- [38] A. Donnachie and P. V. Landshoff, *Phys. Lett.* B296 (1992) 227–232.
- [39] L. Durand and P. Hong, *Phys. Rev. Lett.* 58 (1987) 303.
- [40] M. L. Good and W. D. Walker, *Phys. Rev.* 120 (1960) 1857–1860.
- [41] R. Engel, Universität Siegen (see <http://www-ik.fzk.de/~engel/phojet.html>) (1997) .
- [42] M. Derrick *et al.* (ZEUS Collab.), *Phys. Lett.* B315 (1993) 481.
- [43] R. J. Glauber, *Phys. Rev.* 100 (1955) 242–248.
- [44] R. J. Glauber and G. Matthiae, *Nucl. Phys.* B21 (1970) 135–157.
- [45] T. Sjostrand, S. Mrenna, and P. Z. Skands, *Comput. Phys. Commun.* 178 (2008) 852–867
- [46] M. Bahr *et al.*, *Eur. Phys. J.* C58 (2008) 639–707
- [47] B. L. Combridge and C. J. Maxwell, *Nucl. Phys.* B239 (1984) 429.
- [48] E. Eichten, I. Hinchliffe, K. Lane, and C. Quigg, *Rev. Mod. Phys.* 56 (1985) 579.
- [49] H.-U. Bengtsson and T. Sjostrand, *Comput. Phys. Commun.* 46 (1987) 43.
- [50] T. Sjostrand, *Int. J. Mod. Phys.* A3 (1988) 751.
- [51] F. Becattini, *Z.Phys.* C69 (1996) 485–492.
- [52] G. J. Alner *et al.* (UA5 Collab.), *Z. Phys.* C33 (1986) 1.
- [53] F. Abe *et al.* (CDF Collab.), *Phys. Rev. D* 41 (1990) 2330.
- [54] V. Khachatryan *et al.* (CMS Collab.), *Phys. Rev. Lett.* 105 (2010) 022002.
- [55] S. Chatrchyan *et al.* (CMS Collab.), *JHEP* 11 (2011) 148 [Erratum: *JHEP*02,055(2012)].
- [56] V. Khachatryan *et al.* (CMS Collab.), *JHEP* 01 (2011) 079.
- [57] S. Chatrchyan *et al.* (CMS Collaboration Collab.), *Eur.Phys.J.* C72 (2012) 2164
- [58] T. Anticic *et al.* (NA49 Collab.), *Eur. Phys. J. C* 65 (2009) 6–93.
- [59] A. Fedynitch, J. Becker Tjus, and P. Desiati, *Phys. Rev. D* 86 (2012) 114024

- [60] J. Engel, T. K. Gaisser, T. Stanev, and P. Lipari, *Phys. Rev. D* 46 (1992) 5013–5025.
- [61] F. Riehn, R. Engel, A. Fedynitch, T. K. Gaisser, and T. Stanev, *EPJ Web Conf.* 99 (2015) 12001
- [62] G. Antchev, P. Aspell, I. Atanassov, V. Avati, J. Baechler, *et al.*, *Europhys.Lett.* 96 (2011) 21002
- [63] P. Abreu *et al.* (Pierre Auger Collaboration Collab.), *Phys.Rev.Lett.* 109 (2012) 062002
- [64] J. Abraham *et al.* (Pierre Auger Collab.), *Nucl. Instrum. Meth.* A523 (2004) 50–95.
- [65] R. Abbasi *et al.* (IceCube Collaboration Collab.), *Nucl.Instrum.Meth.* A700 (2013) 188–220
- [66] G. Antchev *et al.* (TOTEM Collaboration Collab.), *Europhys.Lett.* 95 (2011) 41001
- [67] G. Antchev *et al.* (TOTEM Collab.), *Nucl. Phys.* B899 (2015) 527–546
- [68] D. W. Duke and J. F. Owens, *Phys.Rev.* D30 (1984) 49–54.
- [69] M. Glück, E. Reya, and A. Vogt, *Eur. Phys. J. C* 5 (1998) 461.
- [70] V. Khachatryan *et al.* (CMS Collab.), *JHEP* 02 (2010) 041.
- [71] M. Honda, T. Kajita, K. Kasahara, S. Midorikawa, and T. Sanuki, *Phys. Rev. D* 75 (2007) 043006.
- [72] F. M. Liu, T. Pierog, J. Aichelin, and K. Werner, 2003.
- [73] C. Alt *et al.* (NA49 Collab.), *Eur. Phys. J. C* 45 (2006) 343–381.
- [74] E.-J. Ahn, R. Engel, T. K. Gaisser, P. Lipari, and T. Stanev, [arXiv:1102.5705 \[astro-ph.HE\]](https://arxiv.org/abs/1102.5705).
- [75] C. Lourenco and H. K. Wohri, *Phys.Rept.* 433 (2006) 127–180
- [76] G. A. Alves *et al.* (E769 Collab.), *Phys. Rev. Lett.* 77 (1996) 2388–2391.
- [77] E. M. Aitala *et al.* (E791 Collaboration Collab.), *Phys.Lett.* B371 (1996) 157–162
- [78] S. J. Brodsky, P. Hoyer, C. Peterson, and N. Sakai, *Phys.Lett.* B93 (1980) 451–455.
- [79] B. L. Combridge, *Nucl. Phys.* B151 (1979) 429.
- [80] B. Abelev *et al.* (ALICE Collaboration Collab.), *JHEP* 1201 (2012) 128
- [81] R. Aaij *et al.* (LHCb collaboration Collab.), *Nucl.Phys.* B871 (2013) 1–20
- [82] M. Aguilar-Benitez *et al.* (LEBC-EHS Collaboration Collab.), *Z.Phys.* C40 (1988) 321.
- [83] R. Ammar *et al.* (LEBC-MPS Collaboration Collab.), *Phys.Rev.Lett.* 61 (1988) 2185–2188.
- [84] A. Zoccoli *et al.* (HERA-B Collaboration Collab.), *Eur.Phys.J.* C43 (2005) 179–186.
- [85] B. Abelev *et al.* (ALICE Collaboration Collab.), *JHEP* 1207 (2012) 191
- [86] L. Adamczyk *et al.* (STAR Collaboration Collab.), *Phys.Rev.* D86 (2012) 072013
- [87] A. Adare *et al.* (PHENIX Collaboration Collab.), *Phys.Rev.* C84 (2011) 044905
- [88] R. A. Briere *et al.* (CLEO Collaboration Collab.), *Phys.Rev.* D76 (2007) 012005
- [89] E. Albini, P. Capiluppi, G. Giacomelli, and A. M. Rossi, *Nuovo Cim.* A32 (1976) 101.
- [90] M. Gell-Mann, *Phys.Lett.* 8 (1964) 214–215.
- [91] H. Fritzsche and M. Gell-Mann, *eConf C720906V2* (1972) 135–165

- [92] B. Andersson, G. Gustafson, and T. Sjostrand, *Phys.Scripta* 32 (1985) 574.
- [93] P. Eden and G. Gustafson, *Z. Phys.* C75 (1997) 41–49
- [94] M. Adamus *et al.* (NA22 Collab.), *Z. Phys.* C35 (1987) 7.
- [95] N. M. Agababyan *et al.* (EHS-NA22 Collaboration Collab.), *Z.Phys.* C46 (1990) 387–395.
- [96] A. E. Hervé In *Proceedings, 34th International Cosmic Ray Conference (ICRC 2015)* 2015.
- [97] I. V. Azhinenko *et al.* (EHS-NA22 Collab.), *Z. Phys.* C46 (1990) 525–536.
- [98] M. Adamus *et al.* (EHS-NA22 Collab.), *Z. Phys.* C39 (1988) 311–329.
- [99] A. Bialas, *Phys.Lett.* B466 (1999) 301–304
- [100] A. Adare *et al.* (PHENIX Collaboration Collab.), *Phys.Rev.* C83 (2011) 064903
- [101] R. Engel and R. Ulrich, GAP-2012-056, 2012.
- [102] K. Goulianos, *Phys. Rept.* 101 (1983) 169.
- [103] A. Buckley, J. Butterworth, L. Lonnblad, D. Grellscheid, H. Hoeth, J. Monk, H. Schulz, and F. Siegert, *Comput. Phys. Commun.* 184 (2013) 2803–2819
- [104] J. Whitmore, *Phys. Rept.* 10 (1974) 273–373.
- [105] S. Chekanov *et al.* (ZEUS Collab.), *Nucl. Phys.* B658 (2003) 3–46.
- [106] T. Anticic *et al.* (NA49 Collaboration Collab.), *Eur.Phys.J.* C68 (2010) 1–73
- [107] I. V. Azhinenko *et al.* (EHS-NA22 Collab.), *Z. Phys.* C44 (1989) 573.
- [108] S. Chatrchyan *et al.* (CMS Collab.), *JINST* 3 (2008) S08004.
- [109] S. Chatrchyan *et al.* (CMS, TOTEM Collab.), *Eur. Phys. J.* C74 (2014) 3053
- [110] G. Anelli *et al.* (TOTEM Collab.), *JINST* 3 (2008) –08007.
- [111] R. Aaij *et al.* (LHCb Collab.), *Eur. Phys. J.* C73 (2013) 2421
- [112] O. Adriani *et al.* (LHCf Collab.), *JINST* 3 (2008) S08006.
- [113] A. A. Alves, Jr. *et al.* (LHCb Collab.), *JINST* 3 (2008) S08005.
- [114] O. Adriani *et al.* (LHCf Collab.), arXiv:1507.08764 [hep-ex].
- [115] O. Adriani *et al.* (LHCf Collab.), *Phys. Lett.* B750 (2015) 360–366
- [116] F. Abe *et al.* (CDF Collab.), *Phys. Rev. Lett.* 61 (1988) 1819.
- [117] C. Albajar *et al.* (UA1 Collab.), *Nucl. Phys.* B335 (1990) 261.
- [118] G. J. Alner *et al.* (UA5 Collab.), *Phys. Rept.* 154 (1987) 247–383.
- [119] F. Riehn and R. Engel, to be published in *Acta Physica Polonica*, 2015.
- [120] R. A. Nam, S. I. Nikolsky, V. P. Pavluchenko, A. P. Chubenko, and V. I. Yakovlev, *Proc. of 14th Int. Cosmic Ray Conf., Munich 7 (1975)* 2258.
- [121] F. Siohan *et al.*, *J. Phys.* G4 (1978) 1169–1186.
- [122] R. M. Baltrusaitis *et al.* (Fly’s Eye Collab.), in *Proc. 19th Int. Cosmic Ray Conf. (NASA Conf. Publication 2376)* 5, p. 5, La Jolla, 1985.
- [123] M. Honda *et al.* (AGASA Collab.), *Phys. Rev. Lett.* 70 (1993) 525–528.

- [124] G. Aielli *et al.* (Argo-YBJ Collab.), 2009.
- [125] H. H. Mielke, M. Föller, J. Engler, and J. Knapp, *J. Phys. G* 20 (1994) 637.
- [126] R. U. Abbasi *et al.* (Telescope Array Collab.), *Phys. Rev. D* 92 (2015) 032007
- [127] R. Ulrich *et al.*, *Proc. of 34th Int. Cosmic Ray Conf., The Hague* (2015) .
- [128] M. Ave *et al.*, *Astropart. Phys.* 19 (2003) 61–75.
- [129] S. P. Knurenko and A. Sabourov, 2010.
- [130] T. Abu-Zayyad *et al.* (HiRes-MIA Collab.), *Astrophys. J.* 557 (2001) 686–699.
- [131] R. U. Abbasi *et al.* (HiRes Collab.), *Astrophys. J.* 622 (2005) 910–926.
- [132] A. Aab *et al.* (Pierre Auger Collab.), *Phys. Rev. D* 90 (2014) 122005
- [133] K.-H. Kampert and M. Unger, [arXiv:1201.0018 \[astro-ph.HE\]](https://arxiv.org/abs/1201.0018).
- [134] A. Fedynitch, R. Engel, T. K. Gaisser, F. Riehn, and T. Stanev, *ISVHECRI 2014 - 18th International Symposium on Very High Energy Cosmic Ray Interactions* 99 (2015) 08001.
- [135] A. Fedynitch, R. Engel, T. K. Gaisser, F. Riehn, and T. Stanev, *Proc. of 34th Int. Cosmic Ray Conf., The Hague* (2015) .
- [136] A. Fedynitch, *Cascade equations and hadronic interactions at very high energy*, PhD thesis KIT November 2015.
- [137] P. Achard *et al.*, *Physics Letters B* 598 (2004) 15–32.
- [138] T. K. Gaisser, T. Stanev, and S. Tilav, *Front. Phys.* 8 (2013) 748–758–758.
- [139] T. K. Gaisser and M. Honda, *Ann. Rev. Nucl. Part. Sci.* 52 (2002) 153–199.
- [140] T. K. Gaisser, *Astroparticle Physics* 35 (2012) 801–806.
- [141] N. Agafonova *et al.*, *The European Physical Journal C - Particles and Fields* 67 (2010) 25–37.
- [142] S. Chatrchyan *et al.* (The CMS Collaboration Collab.), *Physics Letters B* 692 (2010) 83–104.